Millikelvin Magnetisation studies of Low Dimensional Systems

Submitted by Tristan James Kershaw to the University of Exeter as a thesis for the degree of *Doctor of Philosophy in Physics* August 2008.

I certify that all material in this thesis which is not my own work has been identified and that no material has previously been submitted and approved for the award of a degree by this or any other University.

(signature) .....

Abstract

This thesis presents a study of two-dimensional electron systems in GaAs-(Al,Ga)As heterojunctions and quasi-two-dimensional electron and hole systems in graphite within the quantum Hall effect regime of low temperature and high magnetic field. This thesis covers three main sets of experimental work as well as details of the experimental methods (chapter 2) used and the background theory behind the observed results (chapter 1).

The first experimental results presented in this thesis in chapter 3 focus on contactless measurement of the equilibrium magnetisation of sample A2268, a ten layer multiple quantum well sample. Fitting the shape of dHvA oscillations at various temperatures to different models for the density of states, various properties of the system can be estimated, such as the shape of the disorder-broadened density of states and the presence of a background density of states between the Landau levels.

Chapter 4 focuses on measurements of the decay of induced circulating currents in the quasi-dissipationless quantum Hall regime in two samples, V0049 and T73. The induced current is measured via contactless measurement of the associated magnetic moment. The magnitude of the induced current is found to be affected by the sweep rate of the magnetic field and also the distance of approach. The decay of the induced currents is observed at several temperatures and for different magnetic field sweep rates and distances of approach. Decays are observed for up to several days at time, far longer than previously possible. Information about the rate of decay can be used to build a picture of the decay mechanisms present in the quantum Hall regime. The presence of a power-law decay regime indicates many decay mechanisms contribute to the decay of a circulating current in the quasi-dissipationless quantum Hall regime.

Chapter 5 focuses on both contactless magnetometry and transport experiments carried out on a graphite sample. The experiments aim to confirm or dispute recent claims of Dirac fermions in graphite. Experiments are carried out at temperatures in the range 30 mK to ~4 K and at two different angles to the applied magnetic field. Phase analysis of both Shubnikov de Haas and de Haas van Alphen oscillations is used to distinguish

between normal and Dirac fermions. Observation of quantum Hall effect displays the presence of a half-integer quantum Hall staircase similar to that observed in graphene.

Acknowledgements

There are several people I would like to thank for helping me both in the course of my PhD and during the writing of this thesis. Firstly, my supervisor Alan Usher for his guidance and the many useful discussions about my experiments. I would also like to thank Martin Smith for being the extra pair of hands that is sometimes required when trying to run a dilution fridge. I would also like to thank the mechanical workshop staff for creating some rather fiddly items of kit of the last few years. Also Dave Manning and Adam Woodgate for always having an extra dewar of liquid He when it is needed.

Finally thank you to my parents and Caroline for their support during my PhD and also to the Friday pub crowd who provided a valuable source of distraction.

Table of contents

List of Figures

1 Introduction and Background

1.1 Introduction

The semiconductor industry is moving at a tremendous pace, striving to make semiconductor devices smaller, faster and more energy efficient. Mobile phones are constantly being made smaller, whilst containing more features such as CCD (charge-coupled device) cameras and solid-state memory devices for storing music. A modern computer CPU (central processor unit) crams millions of transistors into a chip each measuring only 45 nm across and capable of switching on and off 300 billion times a second [http://www.intel.com/]. As the size of these devices decreases they approach the point where quantum confinement and localisation become important. At this level electron-electron interactions could produce a serious perturbation to the system, so it is desirable to understand the nature of these electronic interactions. Studies of low dimensional electron systems, in particular two-dimensional electron systems (2DES) can provide valuable information about the quantum mechanical interactions between charged particles in a magnetic field. The quantum Hall effect (QHE), which results from the forced localisation within these structures gives an insight into the quantum mechanical interactions present in the system. Observations of these electronic interactions within a 2DES may provide invaluable information to the semiconductor industry in the future.

This thesis presents novel direct measurements of the magnetisation of 2DESs and the electron interactions present within the system. The magnetisation of a 2DES is a thermodynamic property of the system and relates to the electron density of states (DOS) when the system is in equilibrium. Also measurements of the magnetic moment associated with non-equilibrium currents circulating in the plane of the 2DES have been measured. Observation of these currents via their associated magnetic moment gives an insight not only into the electron-electron interactions but also electron-phonon interactions and impurity scattering events. All of these measurements give valuable information about the quantum mechanics of electrons within nanostuctures. This chapter will discuss the effects of confinement on electrons, the properties of an ideal two-dimensional electron gas (2DEG) and the effect of applying a magnetic field to such a system.

1.2 Low dimensional systems

In this section we will discuss the effects of confinement on the electron energy levels within a semiconductor and obtain expressions for the density of states $D(E)$ and the Fermi energy E_F. We shall start from the free-particle Schrödinger equation in three dimensions which is given by

eqn. 1.2.i
$$-\frac{\hbar^2}{2m}\left(\frac{\partial^2}{\partial x^2}+\frac{\partial^2}{\partial y^2}+\frac{\partial^2}{\partial z^2}\right)\psi_k(\mathbf{r})=\varepsilon_k\psi_k(\mathbf{r}).$$

If the charge carriers are confined to a cube of length L, the wavefunction takes the form of a standing wave.

eqn. 1.2.ii
$$\psi_n(\mathbf{r})=A\sin\left(\frac{n_x\pi x}{L}\right)\sin\left(\frac{n_y\pi y}{L}\right)\sin\left(\frac{n_z\pi z}{L}\right),$$

where n_x, n_y and n_z are positive even integers and the origin is located at one corner of the cube, A is a constant. If the wavefunction is periodic in L then $\psi(x + L, y, z) = \psi(x, y, z)$ and similarly for the y and z directions. Wavefunctions for free particles that satisfy the periodic boundary condition (i.e. for an infinite size crystal) Schrödinger equation are of the form of a travelling plane wave.

eqn. 1.2.iii
$$\psi_k(\mathbf{r})=A\exp(i\mathbf{k}\bullet\mathbf{r}),$$

with the components of the wavevector **k** satisfying the following for values of k_x, k_y and k_z.

eqn. 1.2.iv
$$k_{x,y,z}=0;\ \pm\frac{2\pi}{L_{x,y,z}};\ \pm\frac{4\pi}{L_{x,y,z}};\ \ldots$$

Upon substitution of eqn. 1.2.iii into eqn. 1.2.i the following can be obtained.

eqn. 1.2.v
$$E_k=\frac{\hbar^2}{2m}\mathbf{k}^2=\frac{\hbar^2}{2m}\left(k_x^2+k_y^2+k_z^2\right),$$

where E_k is the energy of the wavefunction with wavevector **k**. The velocity of a particle in the orbital would be $\mathbf{v} = \hbar\mathbf{k}/m$ from $\mathbf{p} = \hbar\mathbf{k}$. In the ground state of a system of N free electrons all states up to the Fermi energy E_F are filled and all higher energy states are empty. To calculate the energy of the highest occupied state we note that each combination of n_x, n_y and n_z correspond to points on a 3D grid with points separated by π/L in each direction. For a sphere centred on the origin, points on the surface are at a distance $(k_x^2+k_y^2+k_z^2)^{½}$ from the origin and consequently have the same energy. This allows us to determine the energy of the highest occupied state by increasing the radius of the sphere $(k_x^2+k_y^2+k_z^2)^{½}$ so that the surface encloses sufficient states to accommodate all of the N electrons in the system. Since each point corresponds to a cube of unit volume, the number of grid points is equal to the volume enclosed by the surface. Due to the conditions imposed in eqn. 1.2.iv each volume element $(2\pi/L)^3$ has a distinct triplet of quantum numbers (k_x, k_y, k_z) and hence only one allowed wavevector **k**. Therefore, we can deduce that for a sphere of $4\pi k_F^3/3$ the total number of orbitals can be given by

eqn. 1.2.vi
$$N = 2\left(\frac{4}{3}\frac{\pi k_F^3}{(2\pi/L)^3}\right) = \frac{V}{3\pi^2}k_F^3,$$

where V is the volume L^3 (assuming $L_x = L_y = L_z$) and the prefactor of 2 comes from the two allowed states of the spin quantum number m_s for each value of **k**. Hence, rearranging and using eqn. 1.2.v we can find the energy of the highest occupied state (the Fermi energy E_F) is

eqn. 1.2.vii
$$E_F = \frac{\hbar^2}{2m}\left(\frac{3\pi^2 N}{V}\right)^{\frac{2}{3}}.$$

Using the equation $\mathbf{p} = \hbar\mathbf{k}$ we can obtain the electron velocity v_F at the Fermi energy E_F in terms of the carrier concentration N/V.

eqn. 1.2.viii
$$v_F = \left(\frac{\hbar k_F}{m}\right) = \frac{\hbar}{m}\left(\frac{3\pi^2 N}{V}\right)^{\frac{1}{3}}.$$

Rearrangement of eqn. 1.2.vii allows us to obtain an expression for the three–dimensional density of states $D(E)$.

eqn. 1.2.ix
$$D(E) \equiv \frac{dN}{dE} = \frac{V}{2\pi^2}\left(\frac{2m}{\hbar^2}\right)^{\frac{3}{2}} E^{\frac{1}{2}}.$$

For electrons confined to an infinite one-dimensional square well potential, the energy spectrum in the direction of confinement (z-direction) becomes a series of discrete allowed states in **k**-space and we can write the following Hamiltonian.

eqn. 1.2.x
$$\hat{H}\psi_n = -\frac{\hbar^2}{2m}\frac{d^2\psi_n}{dz^2} = E_n\psi_n.$$

For a well of width L the wavefunction is sinusoidal with wavelengths that satisfy $\lambda_n = 2L/n$ where n is an integer. Hence we can write the wavefunction ψ_n as

eqn. 1.2.xi
$$\psi_n = A\sin\left(\frac{n\pi}{L}z\right),$$

where A is a constant. Differentiating twice with respect to z we obtain

eqn. 1.2.xii
$$\frac{d^2\psi}{dz^2} = -A\left(\frac{n\pi}{L}\right)^2 \sin\left(\frac{n\pi}{L}z\right).$$

From comparison of eqn. 1.2.x and eqn. 1.2.xii it becomes apparent that the energy of a state E_n is given by

eqn. 1.2.xiii
$$E_n = \frac{\hbar^2}{2m}\left(\frac{n\pi}{L}\right)^2.$$

Using this equation and substituting in the values for the free electron mass and equating to k_BT we find that the energy level separation $n = 1 \rightarrow 2$ for a 10nm (100Å) infinite square quantum well, E_z is equivalent to a temperature of approximately 130K. This implies that at temperatures below 130K all the conduction electrons will be in the ground state. The continuous bulk spectrum has been transformed into a set of discrete

sub-bands. Each sub-band has a parabolic dispersion in k_x - k_y plane. That is, each state has the same value of k_z but continuous values of k_x and k_y. The k_z value of each parabola corresponds to allowed levels within the confinement potential.

To obtain an equivalent expression for the density of states (eqn. 1.2.ix) for a 2D system, the starting point is the same except one dimension can be ignored. So the wavefunction takes the form

eqn. 1.2.xiv $$\psi_n = \sin(k_x x)\sin(k_y y) = \sin\left(\frac{n_x \pi x}{L_x}\right)\sin\left(\frac{n_y \pi y}{L_y}\right).$$

Consider a 2D array of points separated by π/L in **k**-space, with a circle representing a line of constant energy centred on the origin with area πk_F^2 enclosing N points. The total number of orbitals including spin can be given by

eqn. 1.2.xv $$N = 2\left(\frac{\pi k_F^2}{\left(2\pi/L\right)^2}\right) = \frac{k_F^2 L^2}{2\pi}\ .$$

Hence the Fermi energy E_F can be written as

eqn. 1.2.xvi $$E_F = \frac{N}{L^2}\frac{\pi\hbar^2}{m},$$

where N/L^2 is the carrier concentration. Rearrangement and differentiation yields the 2D density of states, which is independent of energy.

eqn. 1.2.xvii $$D(E) \equiv \frac{dN}{dE} = \frac{L^2 m}{\pi\hbar^2}.$$

As we can see confinement of electrons in one dimension has a dramatic effect on the form of the density of states (DOS). In bulk material the DOS has an $E^{1/2}$ dependence (eqn. 1.2.ix), if electrons are strictly confined to move in two dimensions the DOS is constant (eqn. 1.2.xvii). Therefore for confinement in one direction within a finite potential the DOS becomes a step-like function (Fig. 1.2.i). At electron energies corresponding to allowed energy levels within the confinement potential the next sub-

band in the energy spectrum becomes available and there is a step like discontinuity in the DOS.

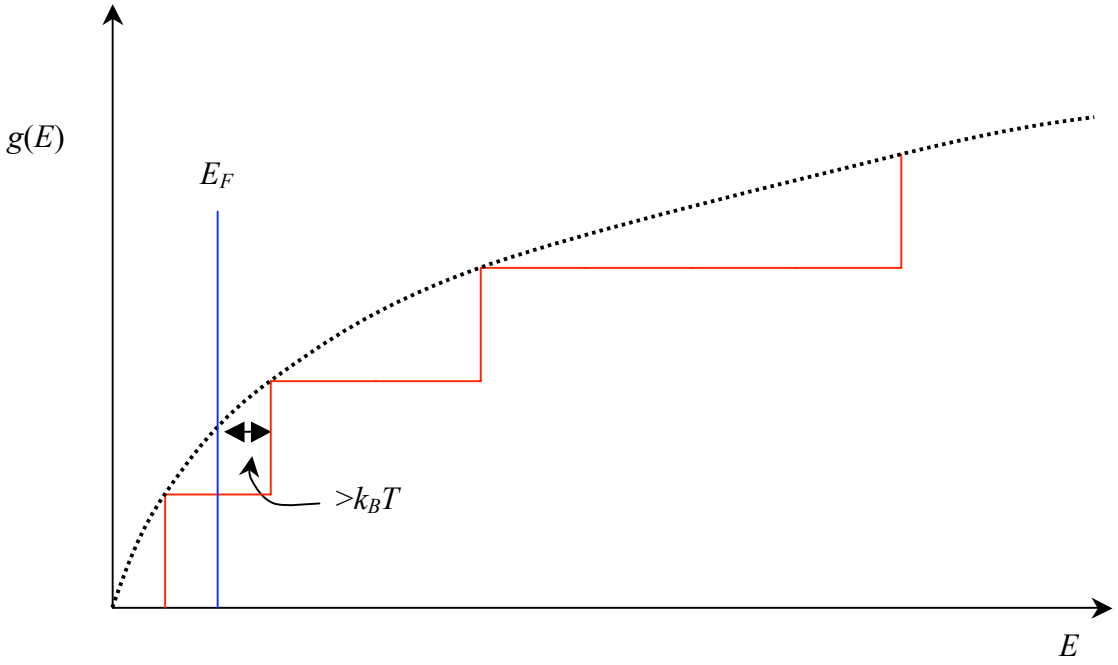

Fig. 1.2.i The DOS in energy space for 2DES (solid line) and 3D (dashed line). The 2D case approaches that of 3D one as L tends to infinity as more discrete energy levels are populated. The position of the Fermi energy (E_F) is indicated on the graph along with the condition needed for only the first sub-band to be occupied at a temperature T.

By controlling the parameters of a practical system it is possible to choose the position of the Fermi level within the material. For a strictly 2D system with no movement possible in the z-direction the required position lies within the first sub-band and is marked on Fig. 1.2.i. The experiments detailed in this thesis were carried out at temperatures below 4 K, at these temperatures k_BT is small compared to E_F, excitation to the 2nd sub-band is not possible and electrons are confined to within the first sub-band. Electron motion in the z-direction is limited to the extent of the confined wave function and electron motion is allowed in two dimensions only and a two-dimensional electron system (2DES) is produced.

1.3 Heterojunctions

Molecular beam epitaxy (MBE) allows the growth of semiconductor structures that have interfaces sharp on the atomic scale. The structure that arises when two chemically different semiconductors are joined together is called a heterojunction. It is assumed that the crystal potential and hence the electrical properties of the two semiconductors involved remain unchanged from those of a bulk semiconductor all the way up to the heterojunction interface. At the interface the electrical properties change abruptly from the bulk values to those of the other semiconductor. Another important benefit of using MBE to grow the sample is the ability to place the dopants away from the interface, a technique referred to as modulation doping. Scattering due to ionised donors can be reduced by spatially separating the dopants from the interface by an un-doped spacer layer. A similar technique called δ-doping can also be used in which the dopants are all placed in a single layer during the growth process, instead of being distributed across several layers as in modulation doping. As Fig. 1.3.i shows a 2DES is formed in the inversion layer in the conduction band at the (Al,Ga)As / GaAs interface.

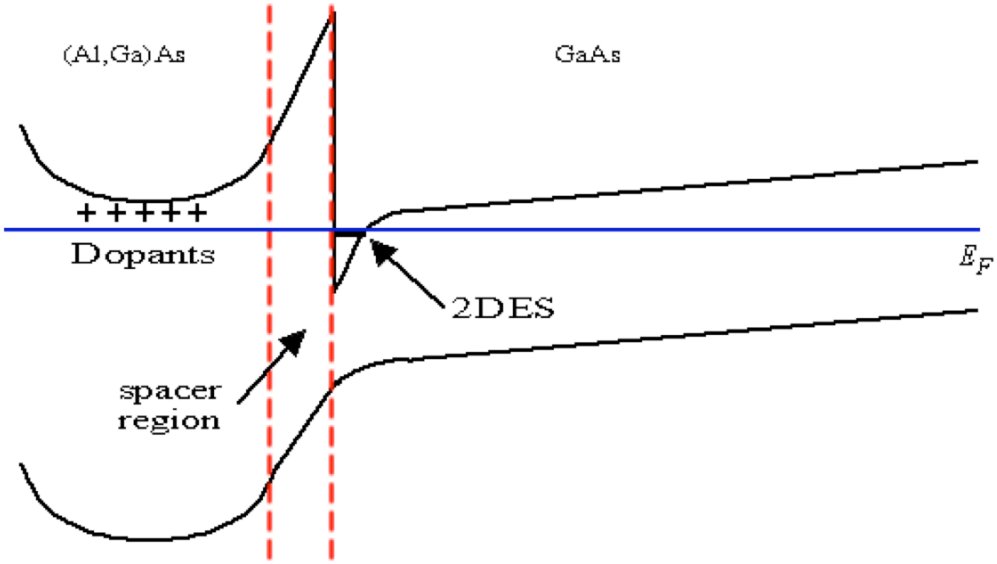

Fig. 1.3.i Schematic of the electronic band structure of a semiconductor heterojunction, depicting the modulation dopants, the spacer region and the resulting band profile. A 2DES is formed where the conduction band drops below the Fermi energy.

Quantum wells are the natural extension of heterojunctions. Two heterojunctions grown back-to-back (close together typically tens of nanometres apart) form a quantum well with the following electronic band profile.

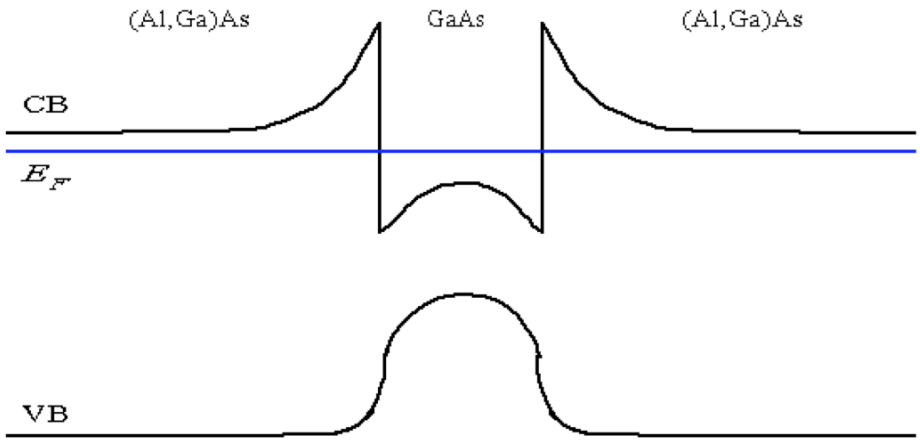

Fig. 1.3.ii Schematic of the electronic band structure of a double heterojunction quantum well.

The materials that lend themselves to MBE are the III-V semiconductors typically for our purposes AlAs and GaAs, although other materials such as II-VI semiconductors can also be used. Ga and Al are both group III metals and GaAs and AlAs have almost the same lattice constant so that strain between the different lattice structures is negligible. The band gap for GaAs and AlAs are 1.42eV and 2.16eV respectively at room temperature. However the heterojunction band gap can be fine tuned by using $Al_xGa_{1-x}As$ and GaAs. However if x exceeds a certain fraction ~0.4 (Ga,Al)As has an indirect band gap that complicates the band structure. Silicon is typically used as the electron donor in III-V semiconductors since Si, being group IV, has an extra electron to donate if it replaces a Ga or Al atom. If the Si replaces an As atom then it acts as an electron acceptor.

1.4 Quantisation of cyclotron orbits in a magnetic field

The application of a magnetic field to a system of weakly interacting electrons such as those in a 2DES further quantises the energy levels of the system and alters the DOS. The momentum of a particle in a magnetic field has two parts, the kinetic momentum $\mathbf{p}_{kin} = m\mathbf{v} = \hbar\mathbf{k}$ and the momentum due to an applied field $\mathbf{p}_{field} = q\mathbf{A}$. $\mathbf{A}$ is the vector potential defined by $\mathbf{B}$ = curl $\mathbf{A}$ and q is the charge on the particle. The total momentum is defined as

eqn. 1.4.i $$\mathbf{p} = \mathbf{p}_{kin} + \mathbf{p}_{field} = \hbar\mathbf{k} + q\mathbf{A}.$$

Onsager (1952) and Lifshitz (1956) showed using a semi-classical approach that electron orbits in a magnetic field are quantised by the Bohr-Sommerfeld relation

eqn. 1.4.ii $$\oint \mathbf{p} \cdot d\mathbf{r} = (n + \gamma)2\pi\hbar,$$

where n is an integer and γ is a phase correction which for non-relativistic electrons has a value $\gamma = ½$

eqn. 1.4.iii $$\oint \mathbf{p} \cdot d\mathbf{r} = \oint \hbar\mathbf{k} \cdot d\mathbf{r} + q\oint \mathbf{A} \cdot d\mathbf{r}.$$

The motion of a particle with charge q in a magnetic field can be written as

eqn. 1.4.iv $$\hbar\frac{d\mathbf{k}}{dt} = q\frac{d\mathbf{r}}{dt} \times \mathbf{B}.$$

Integrating with respect to time gives

eqn. 1.4.v $$\hbar\mathbf{k} = q(\mathbf{r} \times \mathbf{B}).$$

Hence we can write using the geometrical result that $\oint \mathbf{r} \times d\mathbf{r} = 2$(area of orbit)

eqn. 1.4.vi $$\oint \hbar\mathbf{k} \cdot d\mathbf{r} = q\oint \mathbf{r} \times \mathbf{B} \cdot d\mathbf{r} = -q\mathbf{B} \cdot \oint \mathbf{r} \times d\mathbf{r} = -2q\boldsymbol{\Phi},$$

where $\boldsymbol{\Phi}$ is the magnetic flux contained by the orbit in real space. We can write the second half of eqn. 1.4.iii as

eqn. 1.4.vii $$q\oint \mathbf{A} \cdot d\mathbf{r} = q\int \text{curl } \mathbf{A} \cdot d\boldsymbol{\sigma} = q\int \mathbf{B} \cdot d\boldsymbol{\sigma} = q\boldsymbol{\Phi},$$

where $d\boldsymbol{\sigma}$ is the area element in real space. Using eqn. 1.4.vi and eqn. 1.4.vii we can rewrite eqn. 1.4.ii in terms of the magnetic flux $\boldsymbol{\Phi}$ as

eqn. 1.4.viii $$\oint \mathbf{p} \cdot d\mathbf{r} = -q\mathbf{\Phi} = (n+\gamma)2\pi\hbar.$$

Therefore it follows that the orbit of an electron is quantised such that the magnetic flux enclosed by the orbit is

eqn. 1.4.ix $$\mathbf{\Phi}_n = (n+\gamma)\frac{h}{e}.$$

From eqn. 1.4.v we know that a line element Δr in the plane perpendicular to the magnetic field **B** is related to Δk by $\Delta r = (\hbar e/B)\ \Delta k$. Hence the area of an orbit in **k** space S_n is related to the area of the orbit in real space A_n by

eqn. 1.4.x $$A_n = \left(\frac{\hbar}{eB}\right)^2 S_n.$$

Using eqn. 1.4.vii and eqn. 1.4.ix we get

eqn. 1.4.xi $$\mathbf{\Phi}_n = \left(\frac{\hbar}{e}\right)^2 \frac{1}{B} S_n = (n+\gamma)\frac{h}{e}.$$

Hence, the area of an electron orbit in **k** space is

eqn. 1.4.xii $$S_n = (n+\gamma)\frac{2\pi eB}{\hbar}.$$

From this result it is possible to see that the ΔB increment required for two successive orbits n and n+1 to occupy the same area in **k** space is given by

eqn. 1.4.xiii $$S\left(\frac{1}{B_n} - \frac{1}{B_{n+1}}\right) = \frac{2\pi e}{\hbar}.$$

This produces the important result that consecutive electron orbits passing through a constant energy surface in **k** space (such as the Fermi surface) as the magnetic field is increased are periodic in inverse field. As we know from earlier in the chapter an electron wavefunction in two dimensions occupies an area of $(2\pi/\mathrm{L})^2$ in **k** space for a

square sample of side L and from eqn. 1.4.xii we know that the area ΔS between successive orbits n and n+1 is

eqn. 1.4.xiv $$\Delta S = S_{n+1} - S_n = \frac{2\pi e}{\hbar} B.$$

Hence, the number of electron orbitals that can occupy a single magnetic level or Landau level is given by

eqn. 1.4.xv $$D = \frac{2\pi eB}{\hbar}\left(\frac{L}{2\pi}\right)^2 = \frac{eBL^2}{h}.$$

Fig. 1.4.i shows the cross-section of a Fermi surface perpendicular to an applied magnetic field and two consecutive cyclotron orbits.

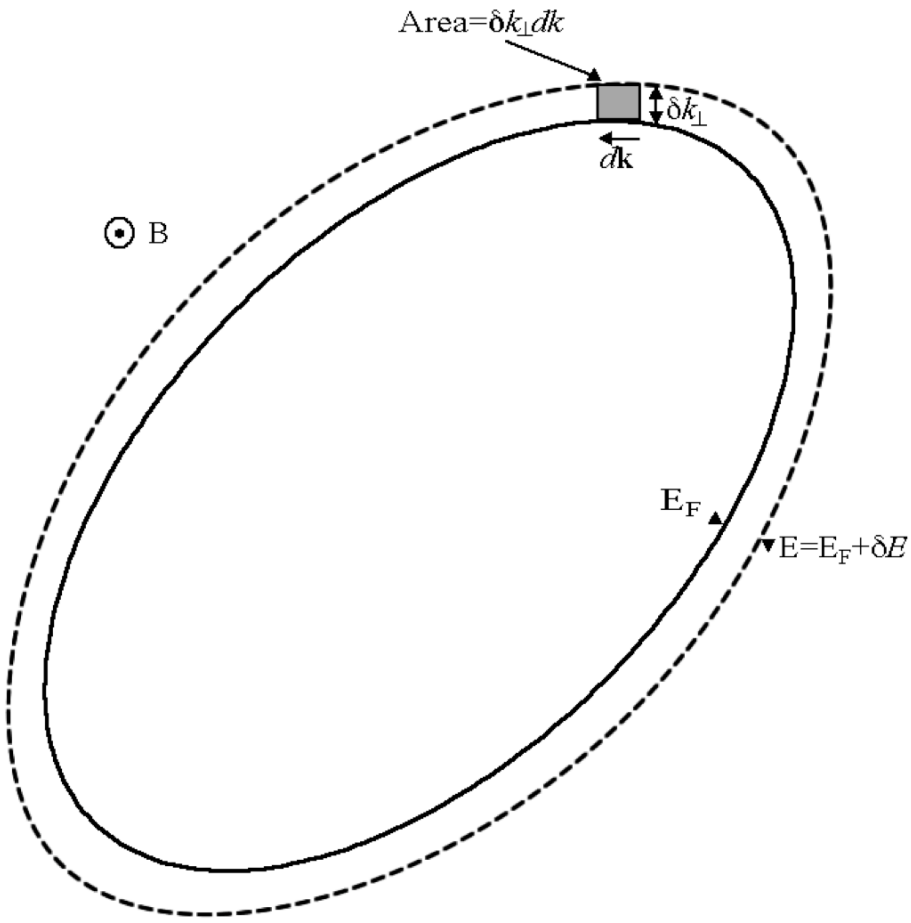

Fig. 1.4.i Illustration of the cross section of the Fermi surface perpendicular to the applied magnetic field showing the area elemental $\delta k_\perp dk$.

The group velocity of an electron at the Fermi energy is $v_F = (\delta E/\delta \mathbf{k})_F/\hbar$ normal to the surface. Since the surface is also perpendicular to the magnetic field, it follows that the electron trajectory in **k**-space is along the Fermi surface contour perpendicular to **B**. Using eqn. 1.4.x one can show that the period of orbit of an electron in **k**-space is

eqn. 1.4.xvi
$$T = \oint \frac{\hbar dk}{e v_\perp B} = \frac{\hbar^2}{eB} \frac{\oint \delta k_\perp dk}{\delta E}.$$

It is apparent that the integral $\oint \delta k_\perp dk$ is equivalent to the ΔS we defined earlier in eqn. 1.4.xiv, as a result we can define a cyclotron frequency as

eqn. 1.4.xvii
$$\omega_c = \frac{2\pi}{T} = \frac{2\pi eB}{\hbar^2} \frac{dE}{dS}.$$

Using $\omega_c = eB/m$ for free electrons in a magnetic field yields a cyclotron mass.

eqn. 1.4.xviii
$$m_c = \frac{\hbar^2}{2\pi} \frac{dS}{dE}.$$

This differs from the definition of the effective mass m^*: m_c is a property of the orbit and is proportional to the first derivative $(dE/dk_\perp)^{-1}$ averaged around the orbit, whereas m^* is proportional to the second derivative $(d^2E/dk^2)^{-1}$ at a point in **k**-space. The effective mass m^* is obtained from an analogous form of Newton's second law $\mathbf{F} = \hbar(d\mathbf{k}/dt)$ such that

eqn. 1.4.xix
$$\frac{1}{m^*} = \frac{1}{\hbar^2}\left(\frac{d^2E}{dk^2}\right).$$

The two masses are only identical for an isotropic parabolic dispersion relation $E = \hbar^2k^2/2m^*$. In the presence of an external field, Schrödinger's equation can be solved exactly, for a field parallel to the z-direction the energy levels are of the form.

eqn. 1.4.xx $$E_n = (n + \tfrac{1}{2})\hbar\omega_c + \frac{\hbar^2 k_z^2}{2m}.$$

Comparison of eqn. 1.4.xx with eqn. 1.2.v shows us that the area of a cyclotron orbit corresponding to the n^{th} Landau level is given by

eqn. 1.4.xxi $$\frac{\hbar^2}{2m}(k_x^2 + k_y^2) = (n + \tfrac{1}{2})\hbar\omega_c.$$

Hence the energy of an electron in the n^{th} Landau level is

eqn. 1.4.xxii $$E_n = (n + \tfrac{1}{2})\hbar\omega_c.$$

Here $\gamma = ½$ as defined by the Bohr-Sommerfeld relation for non-relativistic free electrons. The filling factor ν defines how many Landau levels are full at a given field. Since there is one state per flux quantum per Landau level ν is given by the number of electrons divided by the degeneracy of a Landau level.

eqn. 1.4.xxiii $$\nu = \frac{N\Phi_o}{\Phi}.$$

Or similarly in terms of the electron number density and the degeneracy per unit area the number of occupied Landau levels is given by;

eqn. 1.4.xxiv $$\nu = \frac{n_e h}{eB}.$$

1.5 The de Haas-van Alphen Effect

The magnetisation of a 2DES is a thermodynamical property of the system. Direct measurements of the magnetisation are possible and can yield information about the QHE states within the 2DES. The thermodynamic expression for the magnetisation can be obtained from the Helmholtz free energy F defined as

eqn. 1.5.i $$F = U - TS,$$

where, U is the internal energy, T is the absolute temperature and S is the entropy of the system. The differential form of the 1st law of thermodynamics is

eqn. 1.5.ii $$dU = dQ + dW ,$$

where,

eqn. 1.5.iii $$dQ = TdS .$$

A system magnetised by an infinitesimal increase in the applied magnetic field $d\mathbf{B}$, has work dW done on the system by the magnetic field.

eqn. 1.5.iv $$dW = -\mathbf{M} \bullet d\mathbf{B},$$

where **M** is the magnetisation of the system. Hence the corresponding change in the free energy derived from equations 1.5.iii and 1.5.iv above is

eqn. 1.5.v $$dF = -SdT - \mathbf{M} \bullet d\mathbf{B}.$$

Therefore, the magnetisation of the system can be obtained by differentiating the free energy F with respect to B at constant temperature and electron density.

eqn. 1.5.vi $$M = -\left(\frac{\partial F}{\partial B}\right)_T .$$

Measurement of the magnetisation M in a quasi-static magnetic field B can therefore be used to probe the thermodynamic properties of the system. A convenient way to measure the magnetisation of a system is using torque magnetometry, which is described in the next chapter.

The expected behaviour of M for an ideal system can be obtained by looking at the dependence of the free energy F on the applied field. In an ideal 2DES with no disorder at zero Kelvin the DOS has δ-function Landau levels centred at energies $(n + ½)\hbar\omega_c$. If the Fermi level lies within a partially full Landau level and there are λ completely filled

levels the free energy is the sum of the energy of the electrons in filled Landau levels and the energy of the electrons in the partly occupied level $\lambda + 1$.

eqn. 1.5.vii $$F(B) = \sum_{n=0}^{n=\lambda-1} D\left(n + \frac{1}{2}\right)\hbar\omega_c + \left(\lambda + \frac{1}{2}\right)\hbar\omega_c\left(N - D\lambda\right),$$

where N is the number of electrons and D is the Landau level degeneracy. A plot of free energy $F(B)$ against B (Fig. 1.5.i) shows that the free energy oscillates as B is increased with cusps at integer filling factors.

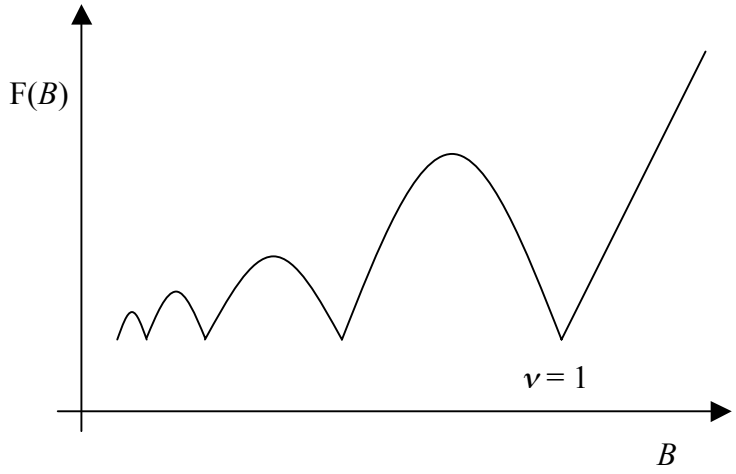

Fig. 1.5.i Plot of $F(B)$ against B. The free energy oscillates as a function of B with cusps at integer filling factors. Note that the energy does not go to zero at zero field.

This oscillatory dependence on B can again be qualitatively explained by considering the occupation of Landau levels at different B values. At high field all electrons are in the first Landau level each with energy $\frac{1}{2}\hbar\omega_c$. As B is reduced ω_c becomes smaller and the total energy decreases. At $\nu = 1$ the first Landau level is completely full and as B is decreased further, electrons are promoted to the second Landau level. Promoted electrons have energy $\frac{3}{2}\hbar\omega_c$ and so the total energy now increases and there is a cusp at $\nu = 1$. This process is repeated and a cusp is seen at all integer filling factors.

A plot of M against B can be obtained by plotting the gradient of the curve in Fig. 1.5.i $-\left(\frac{\partial \mathrm{F}}{\partial \mathrm{B}}\right)_{\mathrm{T}}$ against B.

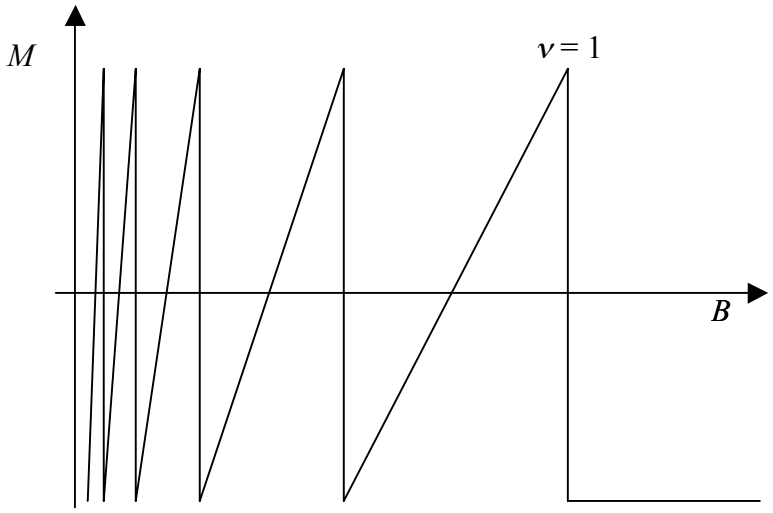

Fig. 1.5.ii Magnetisation of a 2DES as a function of applied magnetic field.

Fig. 1.5.ii shows an oscillatory dependence of M on B with discontinuities at integer values of ν. This is the 2D de Haas-van Alphen (dHvA) effect, first observed in 3D bulk Bismuth by de Haas and van Alphen (1933). As previously mentioned the period of the dHvA oscillations is dependent on the cross sectional area of the Fermi surface perpendicular to the applied magnetic field. For a Fermi surface of general shape with a magnetic field applied in the z-direction, sections at different values of k_z will have different periods. The sample response will be the sum of the contributions from each section or orbit. However, the dominant response will be due to those orbits whose periods are invariant to small changes in k_z. Such orbits are called extremal orbits and occur at points of maximal or minimal cross-sectional area.

The magnetisation of a 2DES was first analysed by Peierls (1933) and revisited in the context of the integer quantum Hall effect (IQHE) by Shoenberg (1984). Shoenberg predicted the oscillating dependence seen in Fig. 1.5.ii and also showed that the Landau level broadening and non-zero temperature will cause deviations from this ideal behaviour. Experimental measurements of the magnetisation can therefore give information about the form of the density of states in the IQHE regime. Eisenstein (1985) was the first to observe the dHvA oscillations in the IQHE regime. The magnetisation curves obtained are shown below.

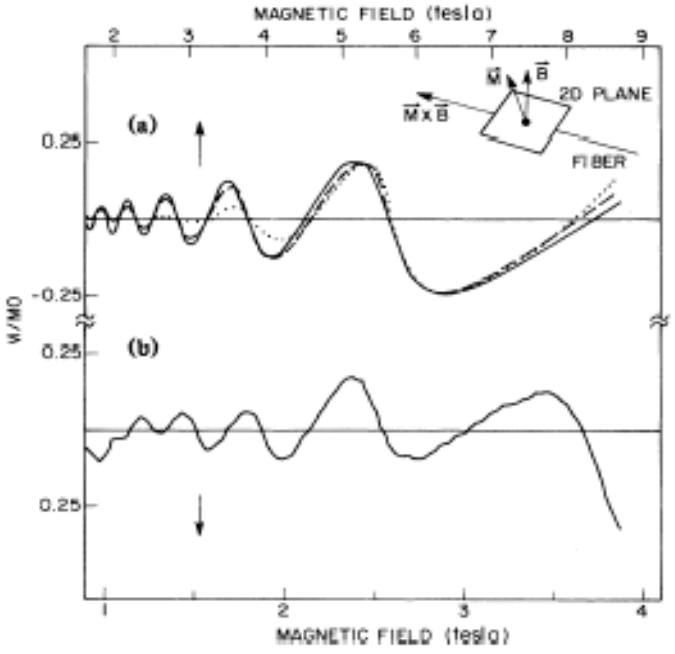

Fig. 1.5.iii Experimental magnetisation curve as a function of applied field obtained by Eisenstein (1985) Sample a) is a 50 × 2DEG with 14 nm GaAs wells and 40 nm AlGaAs Si-doped layers 2D density 5.4×10^{11} cm^{-2}. Sample b) is a single 2DEG with a 100 nm AlGaAs Si-doped layer with 2D density 3.7×10^{11} cm^{-2}. Both samples were at 0.4K.

As predicted by Shoenberg (1984) the curves deviated from the ideal saw tooth oscillations predicted theoretically and they were able to fit the data with a trial form of the disorder-broadened DOS (dotted and dashed lines on Fig. 1.5.iiia). Eisenstein concluded that the Landau level broadening was Gaussian in nature with the overlap between Landau levels giving rise to a significant DOS in between integer filling factors. Eisenstein (1985) also found that the width of the broadened DOS varied with field as $B^{½}$. Further details of the different types of Landau level broadening are discussed in chapter 3.

1.6 Quantum Hall Effect

The integer quantum Hall effect (IQHE) was discovered in 1980 in a 2DES at low temperatures subjected to high magnetic field by von Klitzing, Dorda and Pepper [von Klitzing (1980)]. A quantised Hall resistance was observed with concurrent minima in

the longitudinal resistance. The Hall quantisation was observed to be accurate to better than 5ppm. Later measurements by Cage (1985) have shown that it is accurate to better than 0.01ppm. The fractional quantum Hall effect (FQHE) was discovered in 1984 by Tsui, Störmer and Gossard [Tsui (1984)] when they observed similar features in a high mobility 2DES at fields beyond the IQHE regime (i.e. beyond ν=1). These fractional features correspond to filling factors where there is more than one flux quantum per electron (eqn. 1.4.xxiii).

If Hall measurements are performed on a 2DES at liquid helium temperatures in high magnetic fields a marked deviation from classical behaviour can be observed. Fig. 1.6.i shows the Hall and longitudinal resistivity against applied field for a 2DES at ~8 mK.

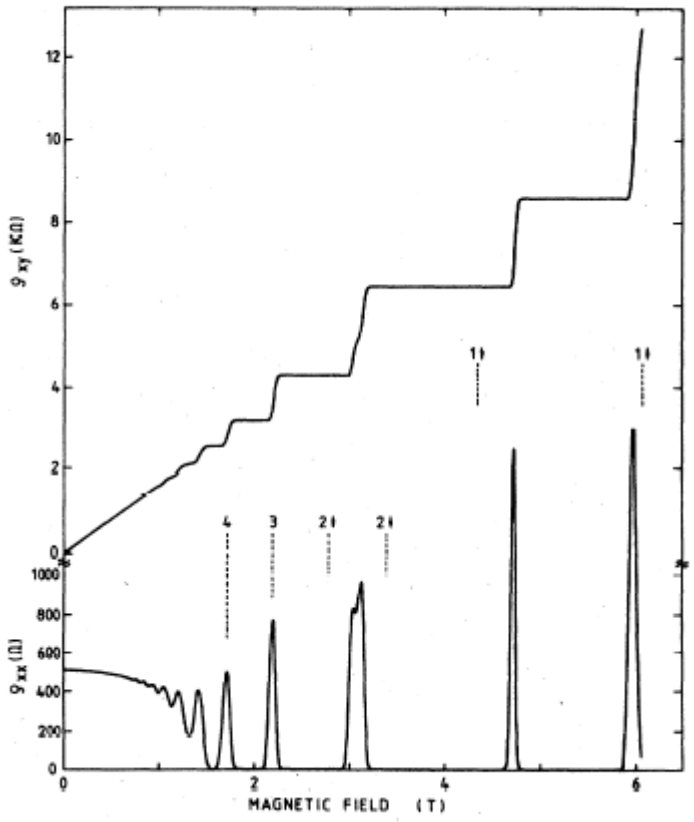

Fig. 1.6.i Experimental curves of Hall resistivity ρ_{xy} and longitudinal resistivity ρ_{xx} as a function of magnetic field obtained from an (Al,Ga)As/GaAs heterostructure, from Von Klitzing (1986)

Broad plateaux are observed in the curve of ρ_{xy} against B with concurrent deep minima in the longitudinal resistivity ρ_{xx}. Von Klitzing (1980) showed that the Hall resistance had a fixed value at certain well-defined magnetic fields. This was observed experimentally in a 2DES formed in the inversion layer of a MOSFET. The value of the

Hall resistance was found to depend only upon the fine-structure constant α ($\approx$1/137) and the speed of light. It was also found to be invariant to changes in the geometry of the sample. The plateaux in ρ_{xy} are quantised to values of $\frac{h}{ie^2}$, where i is an integer.

The quantised Hall states can be modelled as an electron liquid state. A defining property of a liquid is its incompressibility. The adiabatic compressibility for a system with variable volume is given by

eqn. 1.6.i $$\kappa = -\frac{1}{V}\left(\frac{\partial V}{\partial P}\right)_S .$$

This can be converted using the 1st law of thermodynamics (eqn.1.5.ii) to

eqn. 1.6.ii $$\kappa \propto \frac{1}{\frac{\partial^2 E}{\partial V^2}}.$$

Increasing the volume of a 2DES increases the degeneracy and so reduces the filling factor. Therefore V and ν are related by

eqn. 1.6.iii $$V \propto \frac{1}{\nu}.$$

Changes in ν, proportional to changes in V, away from the precise fractional values of ν, perturb the ground state and thereby increase the energy of the system. A plot of E against ν (Fig. 1.5.i) must therefore have a cusp at IQHE and FQHE values, which from eqn 1.6.ii, gives $\kappa = 0$ and so the IQHE and FQHE states are an incompressible liquid.

As we have already discussed the energy levels of a two-dimensional electron system in the presence of a perpendicular magnetic field collapse into discrete Landau levels separated by the energy quantum of their respective cyclotron orbits ($\hbar\omega_c$). When the 2DES is taken to the extreme conditions of high magnetic field and low temperatures, much more striking features emerge, showing the interplay of disorder and the electron-electron interactions of the system [Tsui (1999)]. More specifically, different physics phenomena are observed in three distinctly different physical regimes. Firstly is the disorder dominant regime, when a sample is 'dirty' with low electron mobility (e.g.

$\mu < 10^5$ cm^2/Vs for GaAs [Tsui (1999)]) due to dislocations or impurities within the sample. The striking features in the data constitute the IQHE [Von Klitzing (1980)]. The IQHE is understood in terms of the physics of electrons and their localisation in the presence of random impurities within the sample.

The FQHE is observed in high mobility samples in the regime where the electron-electron interaction dominates. It manifests the many body interaction physics of the 2DES in the intense magnetic field [Tsui (1999)]. Furthermore, even in the cleanest samples, the FQHE series terminates in an insulator phase at the high B limit. This insulator is believed to be an electron crystal pinned by defects to the semiconductor.

The third regime is this high μ and high B limit, where disorder and interaction play equally important roles and need to be treated on an equal basis.

1.6.1 Disorder and Localisation

A GaAs/(Al,Ga)As heterojunction 2DES is generally a very clean system, but in practice all real systems, have some degree of disorder due to imperfections in the structure of the material. This disorder can be represented as a random disorder potential U_D which can be incorporated as an extra term in the equation for the electron energy for an electron in Landau level n.

eqn. 1.6.iv $$E_n = (n + \tfrac{1}{2})\hbar\omega_c + U_D.$$

U_D can be positive or negative and so has the effect of broadening the Landau levels. The DOS for an ideal 2DES is transformed from a set of discrete δ-functions at energies given by the first term in eqn. 1.6.iv to a series of disorder broadened peaks seen in Fig. 1.6.ii.

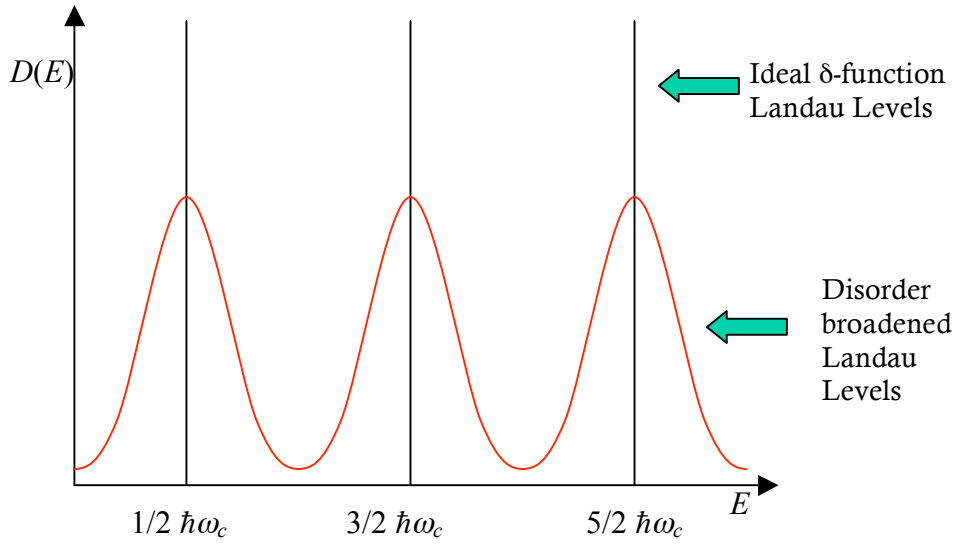

Fig. 1.6.ii Effect of disorder upon the ideal DOS of a 2DES

The exact form of the broadened DOS is still undecided. Gaussian, Lorentzian and elliptical line shapes of the broadened DOS have been suggested, although as yet there is no consensus. Further details about the broadening of the DOS and the theory involved in the different line shapes can be found in chapter 3. The disorder potential also has an effect on the form of the wave functions of the 2D electrons. A 3D representation of the disorder potential (Fig. 1.6.iii) shows peaks and troughs, which represent regions that contain electron energy states with higher or lower energy than average.

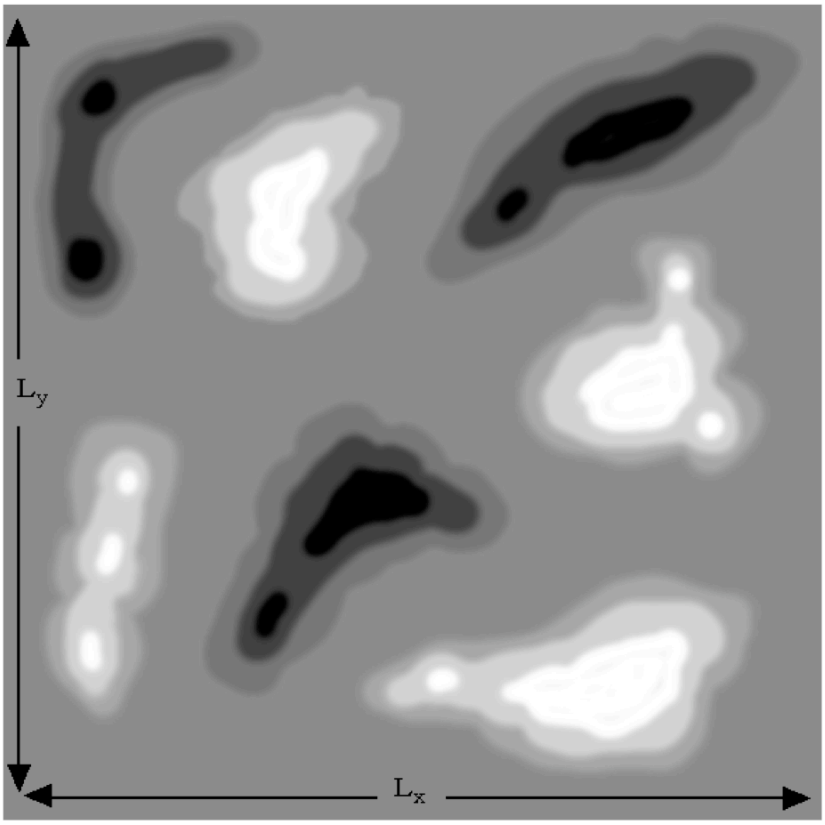

Fig. 1.6.iii Cartoon of a 3D energy plot showing energy peaks (lighter) and troughs (darker) due to disorder in the system.

If these energy states are occupied, electrons will be confined within the regions of high or low energy and the electron wave functions will become localised. This leads to the formation of the localised and extended states.

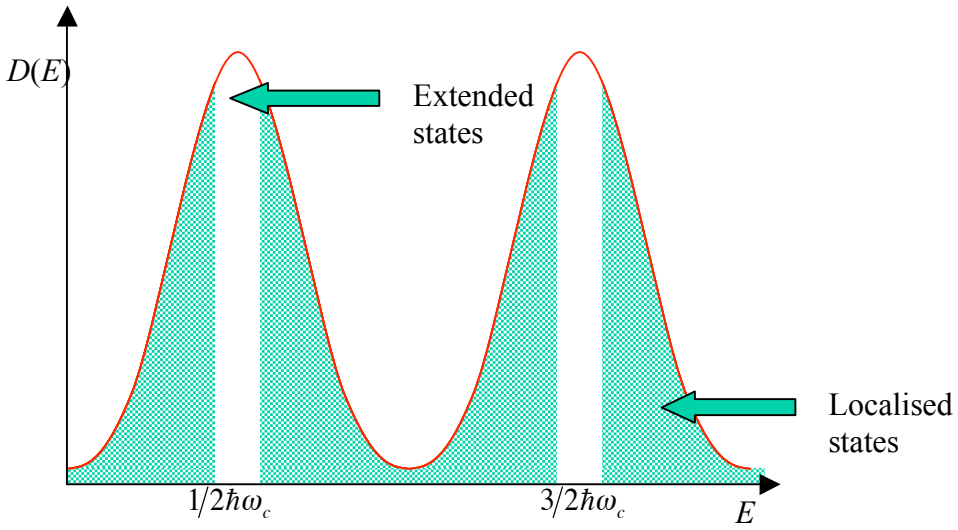

Fig. 1.6.iv DOS for disordered system, showing extended and localised states.

The electron states in the tails of each Landau level are localised with regions of extended states centred around integer filling factor ν. If the tails of the broadened DOS overlap a finite localised density of states can exist between Landau levels. The effects of the random disorder potential are central to the explanation of the IQHE.

Electrical transport within a 2DES in a strong magnetic field occurs when electrons scatter from one state to an adjacent free state in the direction of the applied electric field. As a result, the electrical transport properties of a 2DES are governed by the density of the extended states at the Fermi energy E_F, since electrons confined to the localised states cannot diffuse in this way. By considering the position of E_F on the DOS plot in Fig. 1.6.iv as B is decreased, it is possible to qualitatively explain the features of the IQHE.

At high B field ($\nu < 1$), all the electrons are in the lowest Landau level and close to $\nu = ½$, E_F lies within a region of extended states. When E_F lies within a region of extended states there are empty extended states available at the Fermi level and electrons are able to scatter between extended cyclotron states. Longitudinal current flow is now possible through the Hall bar. Electrons can scatter from one adjacent cyclotron state to another in the direction of the applied longitudinal electric field. This scattering of electrons causes dissipation so that the longitudinal resistivity ρ_{xx} is non-zero. The flow of electrons through the sample perpendicular to B causes a build up of charge along one side of the sample and a transverse electric field E_{xy} is produced. The transverse resistivity ρ_{xy} is therefore proportional to B and, while E_F lies within a region of extended states, ρ_{xy} varies constantly as B is increased or decreased.

As the B field is reduced, ν increases and E_F moves to higher Landau levels. Close to $\nu = 1$ E_F enters a region of localised states in the tail of the first Landau level. Since E_F does not lie in a region of extended states, electrical transport is no longer possible and a 'mobility gap' occurs over this field range. When E_F lies within a 'mobility gap' there is no electron transport and ρ_{xy} cannot change, similarly the longitudinal current density j_{xx} takes a very low value. The longitudinal conductivity σ_{xx} is related to the current density by

eqn. 1.6.v $$\mathbf{j} = \sigma \mathbf{E},$$

so, σxx also takes a very low value. The longitudinal resistivity ρxx is related to σxx by

eqn. 1.6.vi $$\sigma_{xx} = \frac{\rho_{xx}}{\rho_{xx}^2 + \rho_{xy}^2}.$$

If $\rho xy >> \rho xx$, which is true within the mobility gap, then ρxx also takes a very low value. This explains the deep minima in ρxx and σxx observed at $\nu = 1$. As B is reduced further EF enters the region of extended states within the 2nd Landau level ($\nu = 1½$) and electron transport is again possible. A mobility gap and the corresponding features are seen at all integer filling factors. The quantised values of ρxy can be obtained from

eqn. 1.6.vii $$\rho_{xy} = -\frac{B}{n_e e},$$

where n_e is the electron density, using eqn. 1.4.xxiii we can write

eqn. 1.6.viii $$\rho_{xy} = \frac{h}{ie^2}.$$

This gives the quantised values of ρ_{xy} observed at integer filling factors of ν (i = 1,2,3…).

1.6.2 Accuracy of the IQHE

As mentioned earlier the quantisation of the plateaux in ρ_{xy} is accurate to approximately 1 part in 10^8 and it is independent of such parameters such as the electron density or the mobility of the sample. This suggests that the quantisation is due to a fundamental principle. Laughlin (1981) described a thought experiment to show that the accuracy of the quantisation is explained by gauge invariance and the existence of a mobility gap. In the thought experiment a 2DES in a thin strip is bent round to form a closed loop. A magnetic field is applied normal to the surface, which pierces the loop and a Hall voltage V_H, which is measured between the edges of the loop.

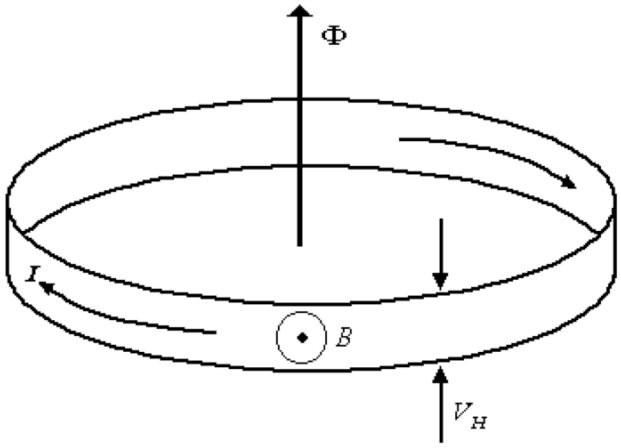

Fig. 1.6.v Schematic of the geometry of Laughlin's thought experiment.

As a flux Φ is passed through the centre of the loop a current *I* flows around the loop, which Laughlin related to the total electronic energy *U*.

eqn. 1.6.ix $$I = \frac{\partial U}{\partial \Phi}.$$

The value of *I* can now be found from the variation δU of the electronic energy that accompanies a small variation in the flux $\delta\Phi$. An increase in the flux through the loop, $\delta\Phi$, is equivalent to the gauge transformation

eqn. 1.6.x $$A \rightarrow A + \delta A = A + \frac{\delta \Phi}{L},$$

where, *L* is the circumference of the loop. This transformation changes the phase of electron wave functions in the 2DES. The wave functions of the localised electrons vanish on a length scale much smaller than *L* and so when E_F lies within a mobility gap the electrons are invariant to this gauge transformation. The wave functions of extended states must be continuous around the loop and this condition will not generally be satisfied if the phase of the wave function is changed. A gauge transformation is only permitted if the change in flux is sufficient to transform the state into an adjacent allowed state, requiring that $\delta\Phi/\Phi_0$ is an integer. When a permitted transformation occurs each electron state is moved on to its neighbouring state. Gauge invariance implies that the final state must be identical after the transformation so the net result is

to transfer charge from one edge of the loop to the other. If a change $\delta\Phi$ of one flux quantum transfers n electrons across the sample the total change in electron energy is given by

eqn. 1.6.xi $$\Delta U = neV_H.$$

Eqn. 1.6.ix can now be rewritten as

eqn. 1.6.xii $$I = \frac{\partial U}{\partial \Phi} = \frac{\Delta U}{\Delta \Phi}$$

and using eqn. 1.6.xi

eqn. 1.6.xiii $$I = \frac{neV}{\Delta \Phi} = \frac{ne^2 V}{h}.$$

Thus, using Ohm's law the Hall resistivity is

eqn. 1.6.xiv $$\rho_{xy} = \frac{h}{ne^2}.$$

Hence, Laughlin showed that the very high accuracy to which ρ_{xy} is quantised is a result of gauge invariance and the existence of a mobility gap.

1.7 Graphite

1.7.1 Band Structure of Graphite and Graphene

Graphite is a 3D layered hexagonal lattice of carbon atoms, made up of stacked single 2D layers called graphene. Even in large bulk samples of graphite the interaction between adjacent layers is small compared with the intra-layer interactions. This is due to the inter-layer separation (3.35Å) being large compared to the nearest neighbour distance between two in-plane carbon atoms (1.42Å) [Physical properties of carbon nanotubes]. Hence the electronic structure of graphite can be approximated to that of many 2D graphene sheets.

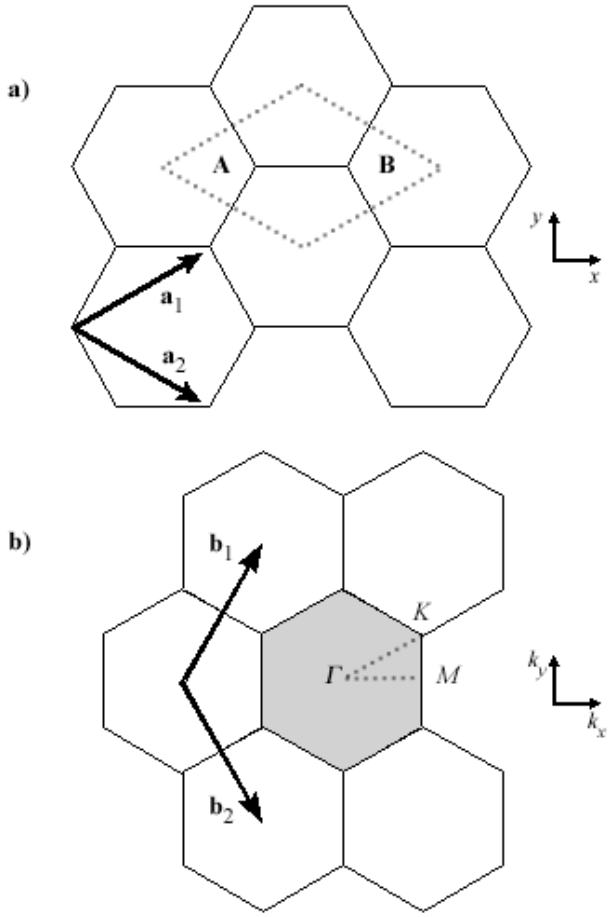

Fig. 1.7.i The unit cell a) and the Brillouin zone b) of graphene are shown as the dotted rhombus and the shaded hexagon respectively. Lines $\mathbf{a}_{1,2}$ are the unit vectors in real space and $\mathbf{b}_{1,2}$ are the reciprocal lattice vectors in *k*-space. *A* and *B* represent the two non-equivalent atoms that make up the unit cell. Energy dispersion relations can be obtained along the dotted triangle connecting the high symmetry points *Γ*, *K* and *M*.

The structure of graphite is known as *abab* or Bernal structure. It consists of planes of carbon atoms (graphene), each forming a hexagonal mesh, the unit cell and Brillouin zone of which are shown above in Fig. 1.7.i. The graphene planes are stacked so that half of the atoms (*A*) are located directly above each other while the other atoms (*B*) are located above the centre of the adjacent hexagon in the plane below (see Fig. 1.7.ii). The atoms *A* and *B* are inequivalent as one cannot move from one atom to the other by a simple translation of the Brillouin zone.

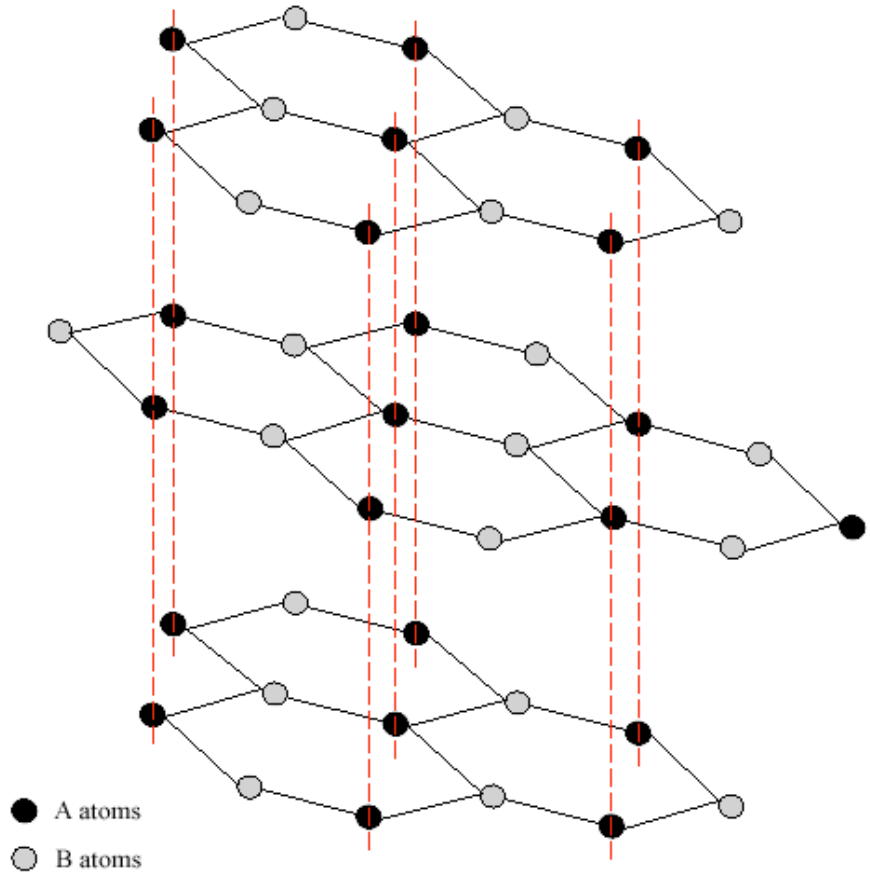

Fig. 1.7.ii Schematic of *abab* or Bernal stacking in graphite. The inter-layer separation is large 3.35Å compared to that of the inter-atom bond length 1.42Å. The distance between equivalent atoms in the plane (shown as $\mathbf{a}_1$ in Fig. 1.7.i) is 2.46Å.

The effective mass Hamiltonian, which describes the energy bands of graphite was first derived by Slonczewski and Weiss [1958] and was further refined by McClure [1957]. However, earlier calculations using the tight-binding approximation showed that the charge carriers in graphite occupy only certain regions of the hexagonal Brillouin zone (Fig. 1.7.iii) and that only the π bands (explained in the next paragraph) near the vertical edges *HKH* are important in the determination of the transport properties of graphite.

There are four atoms per unit cell of graphite, two of each inequivalent carbon atoms *A* and *B*. Each carbon atom in graphite has 6 electrons, 4 in the two inner most *s*-orbitals and two in the outer most 2*p* orbital. The two electrons in the innermost 1*s* orbital are regarded as being core electrons and do not take part in any inter-atomic bonding. The other 4 electrons in the valence bands occupy the 2*s* orbital and the 2*p* orbital. The occupied valance bands are generally referred to as the σ and π band respectively. The σ states are derived from the hybridised 2*s* and in-plane $2p_{x,y}$ orbitals, while the π orbital

are derived from the $2p_z$ orbital perpendicular to the graphene plane. The σ states form three bonds with neighbouring carbon atoms while the other electron in the p_z orbital merges with its nearest neighbours to form an electron 'sea' above the planar surface. It is these p_z electrons that are responsible for the π covalent bonds and hence most of the solid-state properties of graphite. The unoccupied band states derived from the carbon atomic orbitals are designated as the σ^* and π^* orbitals. The lowest energy states are the σ states; these are overlapped by the π states and the highest π states lie just beneath the Fermi energy. The π^* states lie just above E_F and the σ^* states lie above them energetically. The distinction between the π and σ bands is only applicable to planar systems, any form of defects or curvature of the planes leads to mixing of the σ and π states.

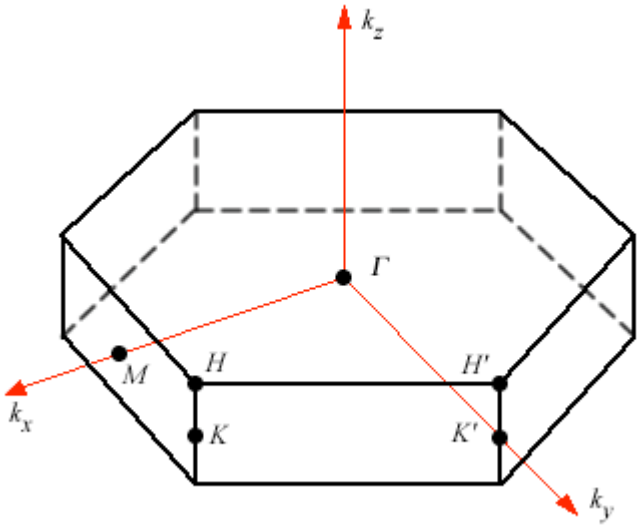

Fig. 1.7.iii Schematic of the 3D Brillouin zone of graphite showing the high symmetry points M, K, Γ and H. Electron and hole pockets are formed by the π bands on the vertical zone edges HKH

Two Bloch functions, constructed from the atomic orbitals of the two inequivalent carbon atoms A and B in Fig. 1.7.ii provide the basis functions for 2D graphite. The upper half of the energy dispersion curve describes the anti-bonding π^* energy band, whereas the lower half describes the bonding π energy band. The four π bands give rise to the 'cigar' shaped electron and hole pockets (Fig. 1.7.iv) along the vertical Brillouin zone edges HKH and $H'K'H'$ (see Fig. 1.7.iii). Both the π and π^* bands are degenerate at the K points through which the Fermi energy E_F passes. A detailed calculation [Slonczewski (1958)] of the density of states shows that the DOS at E_F is zero, hence two-dimensional graphite is a zero gap semiconductor or a semi-metal. The absence of

an energy gap at the *K* point comes from the symmetry requirement that the two atoms A and B are the same. If the atoms A and B were dissimilar then a gap would open at the *K* point between the π and π^* bands.

According to the frequently used Slonczewski–Weiss–McClure (SWMC) model [Williamson (1965)] interlayer coupling between the individual graphene planes in graphite dramatically affects the properties of the electron gas. This interaction leads to the formation of the 'cigar' like Fermi surface pockets (Fig. 1.7.iv) along the *HKH* 3D Brillouin zone edge perpendicular to the $p_{x,y}$ plane.

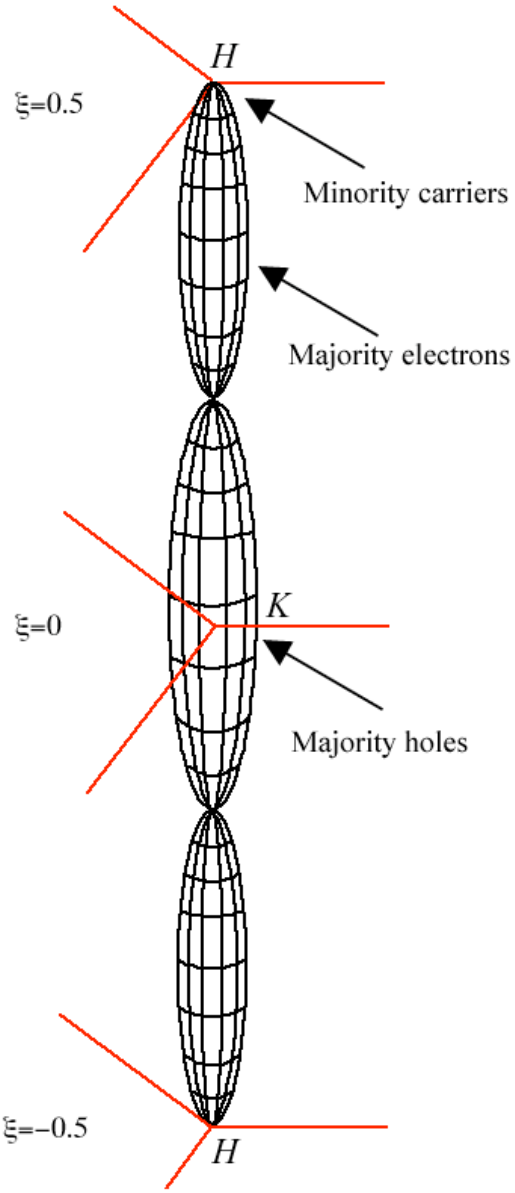

Fig. 1.7.iv Schematic of the Fermi surface of graphite according to the SWMC model. Electron and hole surfaces are shown for the vertical Brillouin zone edge *HKH*.

Majority carrier pockets are located at the extremal Fermi surface points at $\xi = 0$ and $\xi = \pm 0.35$. Minority carriers are located at the *H* point $\xi = \pm 0.5$. The location of the majority carriers pockets within the Fermi surface is disputed, with some groups claiming a reversal of the majority carrier locations [Woolam (1971) and Saito (1998)], however, for consistency the SWMC model results will be used for the time being.

It was shown by Williamson [1965] that at the *H* point the Fermi surface overlaps with the Fermi surface of the mirrored Brillouin zone above. The interlocking of the 'noses' of the 'cigar' shapes defined by the majority electron pockets gives rise to another extremal cross-section of the Fermi surface (Fig. 1.7.v). The central pocket formed from the interlocking of the 'noses' of the two Fermi surfaces gives rise to a well defined extremal area, which is responsible for the minority carrier dHvA oscillations observed in graphite.

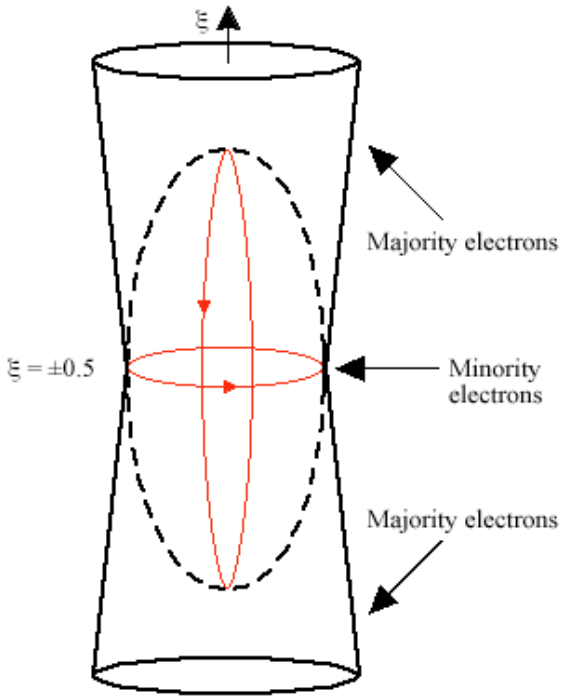

Fig. 1.7.v Schematic of the Fermi surface near to the Brillouin zone corner *H*. A minority carrier pocket is formed at the overlap of the 'cigar' shaped majority electron pockets.

1.7.2 Graphene Physics in Graphite

Recently [Novoselov (2004)] the fabrication of individual graphene flakes (single monolayers) from bulk graphite has led to an increased interest in the physical

properties of graphite. Graphene has several desirable physical properties that make it appealing for use in electronic devices. The relativistic, massless Dirac fermions reported in graphene [Novoselov (2005)] allow very fast conduction of charge with very little dissipation, also the nature of graphene and indeed graphite means the material is bipolar, with both electrons and holes present in the material. By applying a bias voltage to the material an electron or hole current can be selectively allowed to flow [Novoselov (2004)].

However, while the method for producing individual graphene sheets involving the mechanical exfoliation of the graphitic layers from bulk graphite [supplemental material Novoselov (2004)] is surprisingly simple, the results are not consistent enough for commercial or industrial large-scale applications. The graphene flakes are small (a few microns in length) and varying in shape, also the production method produces many more flakes of so called 'few layer graphene' (FLG) two or three graphene layers thick and also small graphite pieces (10+ layers). Currently there is no large-scale method for producing good quality graphene sheets, graphene cannot be grown epitaxially and chemical exfoliation of graphite [Viculis (2005)] yields pieces, which at best are a few layers thick. Also the main method for detecting the presence of graphene is optically, by looking for a slight colour shift in the reflected light from a silicon substrate with a certain thickness of silicon oxide on the surface [Abergel (2007)]. The shift is noticeably greater for each subsequent graphene layer. Unfortunately this means that the graphene flakes are on a substrate of silicon and silicon oxide, which is not always desirable. It is for these reasons that there is a lot of renewed interest in graphite to see if many of the appealing properties of graphene are present in this easy to produce and process material.

It has been proposed that if the inter-layer electron hopping in graphite were zero then the Fermi surface could be reduced to just two points K and K' at opposite corners of the Brillouin zone [Kopelevich (2007)] where the valence and conduction bands touch. This is of course a very similar picture to that of graphene [Novoselov (2005)] and leads to the linear dispersion $E(p) = \pm v|p|$ (where E is the energy and p is the momentum). The p_z electrons move parallel to but not within the graphene layers (through the π bands), this allows the carriers to be described as massless (2+1)D Dirac fermions [Gonzalez (1996)]. This allows a link to relativistic physics models for particles with an effective speed of light on the order of $v \approx 10^6$ ms^{-1}. These models could be used for graphite in

the absence of any interlayer electron hopping. As mentioned earlier in this chapter the presence of any defects or curvature in the graphene planes produces 'mixing' of the σ and π states, if this is the case the system can no longer be described as (2+1)D and interlayer electron hopping can occur. The fundamental question is: if the interlayer hopping in graphite is non-zero how strong is the effect? Currently this remains unanswered because there have been no experiments done on a 'perfect' defect-free sample of graphite. Also if a 'perfect' piece of graphite were possible how much of an effect would the weak van der waals forces between layers have on the electronic properties?

Evidence for the 2D nature of graphite over the 3D like nature predicted by the SWMC model comes from measurements of the interlayer magnetoresistance at low temperatures $\rho_c(B,T)$. Angle dependent measurements of $\rho_c(\theta)$ reveal a maximum in the resistance (the "coherent resistivity peak") when the magnetic field is aligned parallel to the graphene planes for lower quality less ordered graphite samples. However, for well ordered highly–orientated–pyrolytic–graphite (HOPG) samples no maximum in the resistance is observed [Kempa (2003)]. This result suggests that in 'clean' well ordered samples such HOPG samples there is incoherent transport along the *c*-axis perpendicular to the graphene planes, and hence the existence of a 2D-like Fermi surface in graphite. Further evidence for the 2D nature of HOPG graphite samples comes from the presence of the QHE displaying plateaux in the Hall resistance $R_{xy}(B)$. This is in contrast to more disordered 3D-like samples where the QHE is not observed [Kopelevich (2007)].

Kopelevich (2007) postulates that the presence of plateau features in the Hall resistance measurements on highly isotropic graphite samples is indication of a 2D Fermi surface. Such samples also exhibit no 'coherent' resistivity peak in the magnetoresistance measurements when the magnetic field is aligned parallel to the graphitic layers. The ratio between the out of plane resistivity ρ_c and the basal plane resistivity ρ_b in such samples is of the order $\rho_c/\rho_b = 10^4$. This is in contrast to measurements from lower quality Kish graphite samples which do exhibit a 'coherent' resistivity peak where the ratio $\rho_c/\rho_b \sim 100$, such samples do not exhibit any plateau-like features in the Hall resistance. The much larger value of ρ_c in the higher quality samples was attributed to a much higher degree of crystalline orientation along the *c*-axis, confirmed by X-ray rocking curve experiments.

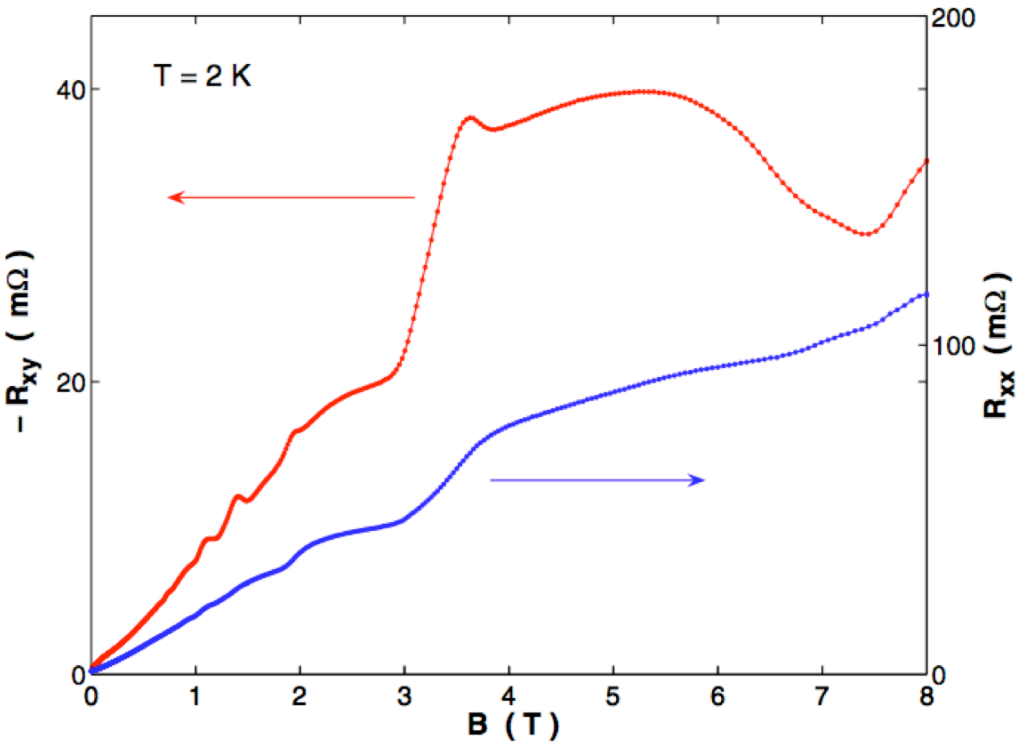

Fig. 1.7.vi Field dependence of basal-plane magnetoresistance $R_{xx}(B)$ and Hall resistance $R_{xy}(B)$ measured for a HOPG sample with magnetic field applied parallel to the *c*-axis. Figure taken from Luk'yanchuk [2006].

The behaviour shown above in Fig. 1.7.vi indicates the presence of a 2D Fermi surface. However, when compared to the equivalent Hall data obtained for standard 2DES there are obvious differences. The longitudinal resistivity ρ_{xx}, which is equivalent to the basal resistivity ρ_b does not fall to zero as expected at integer filling factors. In fact it shows no clear minima corresponding to the plateaus in the Hall resistivity. As can be seen $\rho_{xx} > \rho_{xy}$, this implies that there is still a large amount of structural disorder even in the highest quality HOPG samples. The ρ_{xx} data shown can be considered to be standard SdH oscillations superimposed upon a background field dependent resistivity, which can be attributed to the presence of structural disorder within the sample. Similar behaviour has also been observed in GaAs/AlGaAs 2DESs where $\rho_{xx} > \rho_{xy}$ [Eisenstein (1992)].

Recently a theoretical study of the 3D QHE in graphite using the SWMC model [Bernevig (2007)], predicted the presence of a single plateau in the Hall conductivity $\sigma_{xy}(B)$ for applied magnetic field greater than B_{QL}, where $B_{QL} \sim 8$T is the field at which all carriers are in the lowest Landau level. However as shown in Fig. 1.7.vi plateaus

have been found experimentally in HOPG graphite at fields $B < B_{QL}$. This is further evidence that the SWMC model of 3D graphite is not applicable to high quality 'clean' graphite samples.

Much of the interest in graphene is due to the presence of Dirac fermions with a linear dispersion relation and expected relativistic speeds. If a 'perfect' graphite sample is to be considered as a stack of individual graphene sheets with a 2D Fermi surface, then one would expect Dirac fermions to be present in graphite as well. Quantum oscillation measurements performed on high quality HOPG graphite samples [Luk'yanchuk (2004)] claim to have identified the presence Dirac fermions. The Dirac fermions can be identified from the SdH oscillations, which oscillates as $\sigma_{xx} \sim -\cos[2\pi(B_0/B - \gamma)]$. For normal massive fermions $\gamma = ½$ and for massless Dirac fermions $\gamma = 0$, this leads to a phase difference of π between the different quantum oscillations. This phase difference between the two carrier oscillations is referred to as Berry's phase. The results of Luk'yanchuk are controversial since graphite has been studied extensively in the past [Williamson (1965), McClure (1957), Slonzcewski (1958)] without the phase difference between the two majority carriers being noted. However, the findings of Luk'yanchuk [2004] have been confirmed by angle-resolved photoemission spectroscopy measurements [Zhou (2006)], which show the presence of a linear dispersion relation near the Brillouin zone corner H. Also by observations of the scanning tunneling spectra of graphite samples in a magnetic field [Li (2007)]. This method directly measures the quantisation of the energy levels $E_n = \pm(2e\hbar v_F^2 \mid n \mid B)^{\frac{1}{2}}$. The $B^{1/2}$ dependence being an indication of the presence of Dirac fermions.

Dirac fermions do not obey the standard parabolic formula $E = \mathbf{p}^2/2m$ for massive fermions, instead they have a linear dispersion relation governed by the linear equation $E = \mathbf{p}v$ typically used to describe photons. Hence the equivalent expression for eqn. 1.2.v for Dirac fermions in 3–dimensions is

eqn. 1.7.i $$E_k = \hbar v\mathbf{k} = \hbar v\sqrt{k_x^2 + k_y^2 + k_z^2}\,.$$

Consider a 3D grid of points corresponding to the different combinations of n_x, n_y and n_z separated by π/L in each direction. Using the relation for total number of orbitals

enclosed by a sphere of volume $4\pi k_F^3/3$ centred on the origin given in eqn. 1.2.vi and using eqn. 1.7.i above we can obtain an expression for E_F.

eqn. 1.7.ii $$E_F = \hbar v_F \left(\frac{3\pi^2 N}{V} \right)^{\frac{1}{3}}.$$

Similarly for a 2D system of Dirac fermions using eqn. 1.2.xv and eqn. 1.7.i we can obtain the following

eqn. 1.7.iii $$E_F = \hbar v_F \left(\frac{2\pi N}{L^2} \right)^{\frac{1}{2}}.$$

and hence a 2D density of states $D(E)$.

eqn. 1.7.iv $$D(E) \equiv \frac{dN}{dE} = \frac{L^2}{\pi} \frac{E}{\left(\hbar v_F\right)^2}.$$

Notice that the 2D density of states for Dirac fermions is linear with energy instead of constant as is the case for massive 2D fermions.

The derivation of the quantisation of cyclotron orbits for Dirac fermions follows the same arguments as for normal fermions with a parabolic dispersion relation. The full derivation is rather lengthy and so only brief overview will be shown here. The full derivation can be found in 'Quantum Electrodynamics' [Lifshitz E M, Pitaevskii L P, Berestetskii V B, (Butterworth-Heinmann, Oxford, 1982)]. Using eqn. 1.7.i as a starting point and using Pauli matrices to account for the chirality between the A and B sub-lattices [McCann (2006)] we can write the Hamiltonian as

eqn. 1.7.v $$\hat{H} = v_F \begin{pmatrix} 0 & p_x - ip_y \\ p_x + ip_y & 0 \end{pmatrix} \begin{pmatrix} A \\ B \end{pmatrix} = E \begin{pmatrix} A \\ B \end{pmatrix}.$$

Adapting the momentum to include the effect of magnetic field (**p** becomes **p** + q**A**) and using the Landau gauge **A** = ($-B_y$,0,0) we can re-write the eqn. 1.7.v in terms of two plane-wave functions $\chi_A(y)$ and $\chi_B(y)$.

eqn. 1.7.vi $$\begin{pmatrix} -E & v_F\left(-i\hbar\frac{\partial}{\partial x} - eB_y - \hbar\frac{\partial}{\partial y}\right) \\ v_F\left(-i\hbar\frac{\partial}{\partial x} - eB_y + \hbar\frac{\partial}{\partial y}\right) & -E \end{pmatrix}\begin{pmatrix}\chi_A(y)\\ \chi_B(y)\end{pmatrix}e^{ik_x x} = 0.$$

This in turn yields the harmonic oscillator type expression

eqn. 1.7.vii $$-\frac{d^2\psi}{dx^2} + x^2\left(\frac{m^2\omega^2}{\hbar^2}\right)\psi = \frac{2mE}{\hbar^2}\psi,$$

where ω is the angular frequency of the particle. The solutions of which take the form

eqn. 1.7.viii $$E_s = \pm\sqrt{2eB\hbar v_F^2(s+1)} = \pm\frac{\hbar v_F}{l_B}\sqrt{2(s+1)},$$

where $s = 0, 1, 2 \ldots$ and l_B is the magnetic length $(\hbar/eB)^{½}$. There is also a state at zero energy, which can be solved as a special case allowing eqn. 1.7.viii to be written as

eqn. 1.7.ix $$E_n = \pm\sqrt{2eB\hbar v_F^2 n} = \pm\frac{\hbar v_F}{l_B}\sqrt{2n},$$

where $n = 0, 1, 2 \ldots$ Similarly to the normal fermion case this can be extended to 3D by addition the energy levels in the z-direction.

eqn. 1.7.x $$E_n = \pm\frac{\hbar v_F}{l_B}\sqrt{2n} + \hbar v_F k_z.$$

The following chapter describes some of the details of the apparatus and the experimental methods used to collect the data presented in this thesis.

2 Experimental methods

2.1 Introduction

As discussed in the previous chapter the conditions required for observation of the quantum Hall effect are low temperatures and high magnetic fields. This chapter aims to explain how these conditions can be obtained in the laboratory. The details of the torque magnetometry experiments are also discussed.

The experiments were carried out in the mixing chamber of an Oxford Instruments Kelvinox AST200 dilution refrigerator, located in a low loss Oxford Instruments cryostat equipped with a superconducting magnet capable of maintaining fields of up to 19 Tesla.

2.2 Superconducting Magnets

The discovery of superconductivity has allowed increasingly larger and larger magnetic fields to be used in research. High critical current, high critical field super conductors used to form the windings of electromagnets are able to sustain high magnetic fields without dissipation. This gives superconducting magnets a distinct advantage over traditional Bitter magnets: once energised the magnet no longer needs a constant supply of current to maintain the field since there is no dissipation of the circulating current. The lack of dissipation allows larger currents to be passed using minimal driving voltage, allowing much larger magnetic fields than were achievable or practical with non-superconducting magnets. Although typical current densities are much larger in superconducting magnets there is an upper limit, a critical current density beyond which the material will no longer be superconducting and becomes resistive, this also implies a critical magnetic field which cannot be passed. Persistent currents in superconductors can be maintained indefinitely so long as the critical temperature for the material is not reached. Low temperatures on the order of tens of Kelvin are required to maintain the superconducting state of the wires. Whilst the liquid cryogens required to keep the magnet below the critical temperature are expensive and require regular replenishment, in most cases the cost of cryogens for a superconducting magnet system is much less

than the cost of electricity required to run an equivalent traditional resistive electromagnet.

2.3 Cryostats

Liquid cryogens required for operating superconducting magnets and dilution refrigerators are housed inside a special vacuum vessel called a cryostat. Low loss cryostats such as the one used for the experiments detailed in this thesis are shielded by a liquid nitrogen reservoir. The nitrogen shield minimises the radiation transferred to the helium bath thus reducing helium boil off. Stefan's Law states that the radiated heat transferred between two bodies is proportional to the difference in their absolute temperatures to the fourth power. Hence a surface at 300 K radiates 272 times as much heat as the same surface at 77 K to a surface at 4.2 K. A high vacuum insulates both the liquid helium bath and the liquid nitrogen jacket from external heat loads. Low cryogen boil off is also achieved by constructing the cryostat out of low thermal conductivity materials, however the material used has to be strong enough to support the weight of the magnet and the cryogens it holds. It is for this reason that stainless steel is often used since it has a poor thermal conductivity and yet is very strong. A typical layout of a low loss cryostat is shown in Fig. 2.3.i. depicting the different cryogen and vacuum spaces. Many layers of superinsulation (Mylar sheet coated with aluminum on one or both sides) fill the outer vacuum chamber (OVC) further reducing the radiation transferred from the laboratory to the nitrogen shield, or from the nitrogen shield to the helium bath.

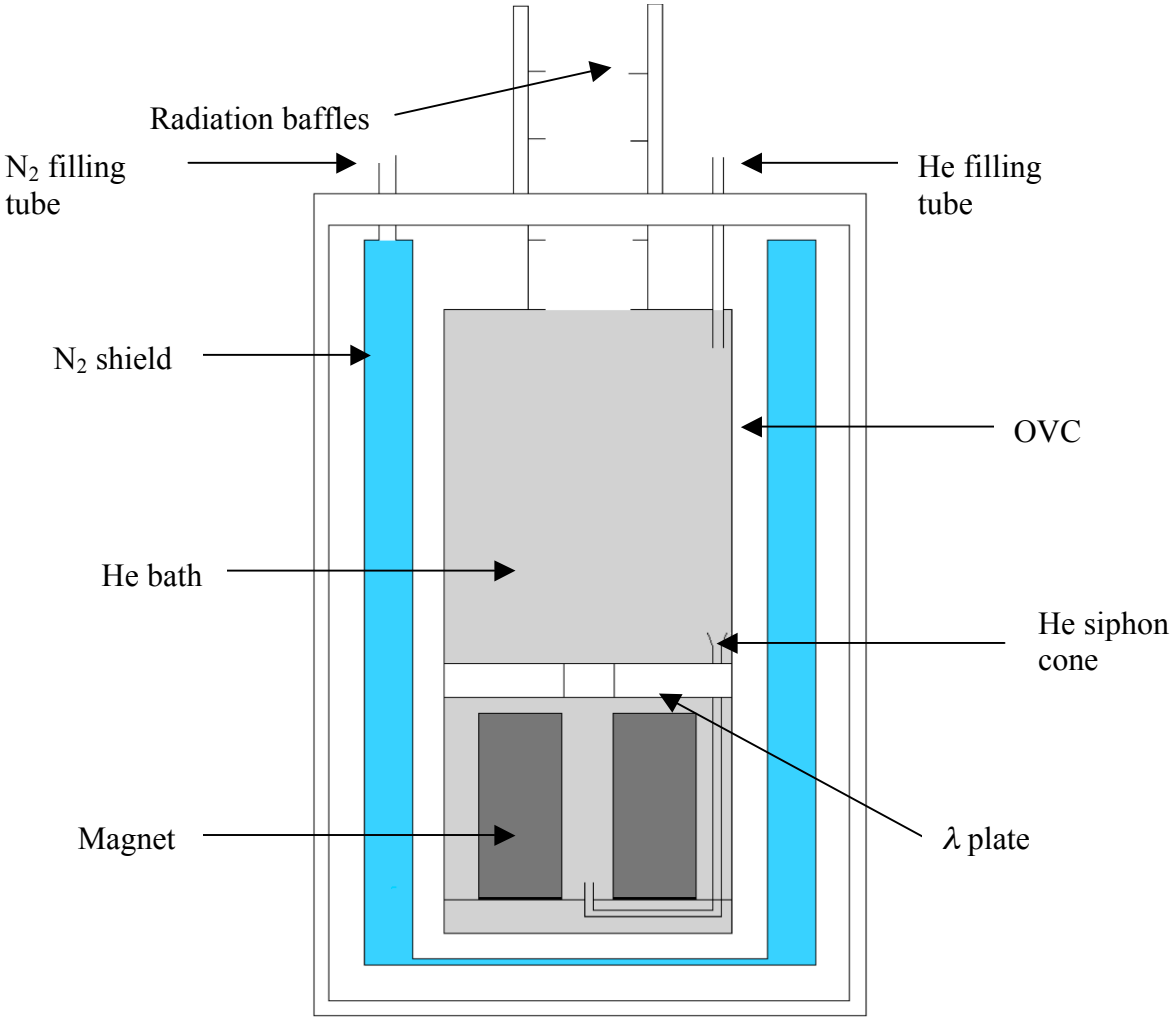

Fig. 2.3.i Schematic of a low loss cryostat showing the orientation of the vacuum and cryogen spaces.

Superconducting magnets are maintained at a temperature of 4.2 K by immersing the coils in the main helium bath. To reach maximum magnetic field the superconducting magnet needs to be cooled to a lower temperature to allow a larger current to be passed down through it without exceeding the critical current density. A temperature of 2.2 K can be achieved by pumping on the surface of the helium in the main bath, this however increases the boil off of the liquid helium. It is for this reason many cryostats are equipped with a λ plate, a baffle that effectively separates the main helium bath into two. The space below the λ plate is cooled by a cooling loop connected to an external pump. The flow of liquid He through the cooling loop is controlled by needle valve. Extra care has to be taken while using the λ plate that the current does not exceed its critical value for a given temperature, causing the magnet to become resistive also known as a 'quench'. If the magnet quenches the stored energy $\left(\frac{1}{2}LI^2\right)$ will be transferred to the liquid helium causing it to boil off rapidly. As a result the temperature

rises and the critical current for the superconducting magnet decreases until the critical temperature is reached. The Oxford Instruments cryostat used for the experiments detailed in this thesis has a main helium bath volume of 120 L and a nitrogen jacket volume of 100 L. The cryostat is equipped with a superconducting magnet with a 4.2 K maximum field of 17 T rising to 19 T at 2.2 K. The magnet has a bore of 52 mm and an inductance of 96.6 H, giving a total stored energy at full field of ~ 6.8×10^5 J.

2.4 Dilution Refrigerators

The ^{3}He / ^{4}He dilution refrigerator has become a standard laboratory instrument for reaching and maintaining ultra low temperatures in the region of tens of millikelvin. When a mixture of the two stable isotopes of helium (^{3}He and ^{4}He) is cooled below a critical temperature it separates into two distinct phases. The less dense ^{3}He-rich phase called the concentrated phase, floats on the denser dilute phase, which is rich in ^{4}He. At temperatures below 0.5 K and ^{3}He concentrations above 6.5% the mixture is separated into these different phases. The dilute phase is so called since the ^{3}He behaves as a gas within the superfluid ^{4}He and has a maximum solubility of 6.5% as the temperature approaches absolute zero.

It is usual to describe the ^{3}He in the concentrated phase as liquid and the ^{3}He in the dilute phase as a gas. The ^{4}He in the dilute phase can be considered to be inert and the ^{3}He moves through the liquid ^{4}He without significant interaction. The enthalpy of the ^{3}He is different in the two phases, allowing cooling to occur by 'evaporating' the ^{3}He from the concentrated phase and pumping it into the dilute phase. This process continues to work even at the lowest obtainable temperature since the equilibrium concentration of ^{3}He in the dilute phase is finite (~ 6%).

The initial cool down of the refrigerator uses the 1K pot to cool the incoming mixture to a temperature low enough to condense the mixture into the unit but not low enough to phase separate the ^{3}He and ^{4}He. The typical amount of ^{3}He for use in dilution refrigerators is approximately 25% the other 75% being made up of ^{4}He. The exact proportions of ^{3}He / ^{4}He depends on the geometry of the system and the desired location of the phase boundary. In order to achieve phase separation the mixture needs to be

cooled to below 0.5 K. This extra cooling can be achieved by reducing the vapour pressure of the liquid mixture in the still using the pumping system. The still is the first part of the refrigerator to cool below the temperature of the pot (~1.5 K). The still cools the incoming ^{3}He before it passes through the heat exchangers and enters the mixing chamber. This process gradually cools the system to a temperature low enough for the ^{3}He / ^{4}He mixture to phase separate and the system to start operating normally.

During normal operation ^{3}He is pumped away from the liquid surface in the still. The still is maintained at a temperature of approximately 0.7 K, at this temperature the vapour pressure of ^{3}He is ~1000 times higher than for ^{4}He. This means ^{3}He evaporates preferentially over ^{4}He and passes through the pumps and back to the dilute phase, heat is applied to the still in order for this process to occur. For continuous operation ^{3}He must be extracted from the dilute phase and returned to the concentrated phase to prevent saturation of ^{3}He in the dilute phase and keep the system in dynamical equilibrium. As the still is pumped upon the concentration of ^{3}He in the concentrated phase drops below 6.5% and there is a flow of ^{3}He between the two phases to maintain the equilibrium concentration caused by the osmotic pressure difference.

In conventional dilution refrigerators room temperature pumping equipment is used to remove ^{3}He from the still and return it to the mixing chamber. This means that the gas has to pass through cold trap filters (activated charcoal cooled in liquid nitrogen) before being cooled by the main He bath and condensed in the 1 K pot.

2.4 Kelvinox AST dilution refrigerators

The Kelvinox AST (Advanced Sorption–pump Technology) series of dilution refrigerators manufactured by Oxford Instruments are based around two sorption pumps located inside the actual fridge unit as shown in Fig. 2.4.i. While the thermodynamics of the cooling process is the same as for a conventional dilution refrigerator, cryogenically sorption pumped units have several advantages. The unit has no moving parts except two cryovalves used to switch between sorption pumps, so it is very quiet mechanically. Also the mixture does not leave the cryostat during operation so helium consumption is decreased since the gas is not warmed to room temperature and then cooled again. Cold

trap filters are only required when condensing the mixture into the fridge and removing it to the storage vessels. Room temperature pumps however, are still required to cool the 1 K pot and to cool the sorption pumps.

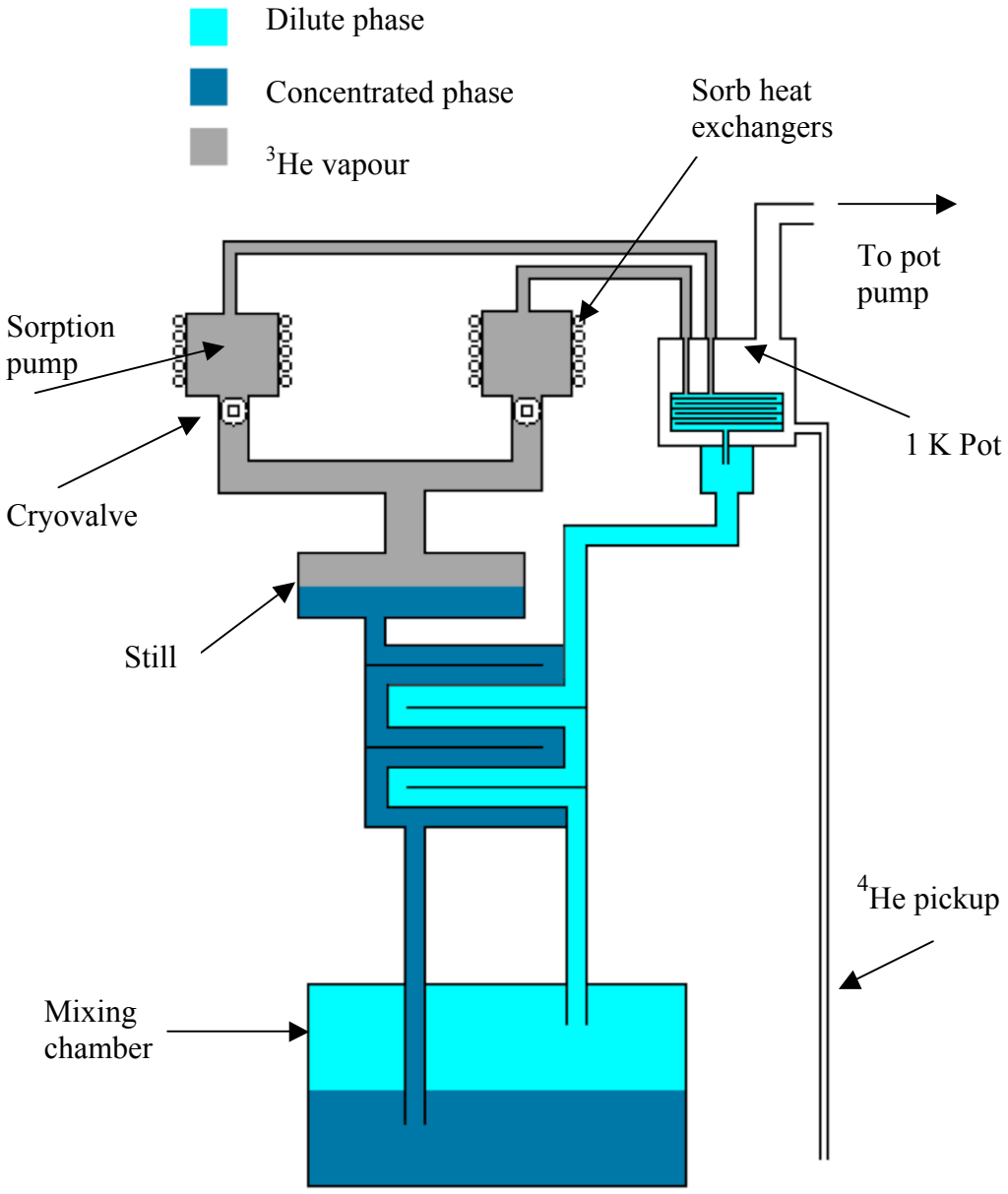

Fig. 2.4.i Simplified schematic of a sorption pumped dilution refigerator.

In a sorption pumped dilution refrigerator two cryogenic sorption pumps cycle to pump ^{3}He around the system. One sorption pump is 'opened' to the still while the other is regenerated and the adsorbed gas returned to the collector and mixing chamber. During sorb regeneration ^{3}He is heated to between 20 K and 40 K and flows from the sorb to the condenser in the 1 K pot and then into the collector. Since at such low temperatures activated charcoal sorption pumps trap contaminants, extra filters and cold traps are not

required during operation. The heating of the regenerating sorb is set to be shorter than the pumping time so that the sorption pump has time to cool before the pumps are changed over. When a sorption pump is being regenerated the cryovalve is closed so that the warm gas does not flow backwards into the still. The 1 K pot condenses the returning ^{3}He and the collector acts as a storage vessel for the liquid ^{3}He. The purpose of the collector is to maintain a steady flow of ^{3}He back into the mixing chamber. The constant temperature of the 1 K pot maintains a constant ^{3}He vapour pressure allowing a constant flow of ^{3}He back into the mixing chamber. The cooling power of a dilution refrigerator is dependent on the balance between the pumping speed of ^{3}He from the still and the rate of return of ^{3}He back into the mixing chamber where phase separation can occur and provide the cooling power needed to maintain such low temperatures. If the flow of ^{3}He back into the mixing chamber is not constant then the cooling power will vary and the temperature of the mixing chamber will fluctuate.

Cryogenic sorption pumps are very powerful and a large throughput of gas can be achieved with relatively small sorption pumps where-as the external room temperature equivalents would be large, mechanically noisy rotary pumps backing a roots booster pump.

The dilution refrigerator is fabricated from non-magnetic stainless steel and is surrounded by a copper clad inner vacuum chamber (IVC). The copper cladding ensures that the entire unit is at a uniform temperature and aids initial cool down, the IVC when evacuated isolates the dilution refrigerator from the relatively warm liquid He in the main bath of the cryostat.

The Oxford Instruments Kelvinox AST200 dilution refrigerator is capable of reaching and maintaining temperatures as low as 15 mK and has a cooling power of 130 μW at 100 mK [Oxford Instruments].

2.5 Torque Magnetometry

At low temperature the electrons in a 2DES are confined to a 2-dimensional plane, hence the magnetisation is confined to be normal to the 2DES. This makes torque magnetometry particularly suited to magnetisation measurements on 2DES. An external

magnetic field applied at an angle θ to the plane of the 2DES results in a torque $\boldsymbol{\tau}$ given by.

eqn. 2.5.i $$\tau = \mathbf{m} \times \mathbf{B} = mB\sin\theta.$$

If the external field and the angle at which it is applied to the 2DES are known then a measurement of the torque represents a measurement of the magnitude of the magnetic moment of the sample and hence the magnetisation of the 2DES.

Several of the experiments detailed in this thesis used 'torsion balance' magnetometry to measure the magnetisation of the sample. This method of magnetometry uses a rotor with the sample placed upon it suspended by a torsion fibre, of torsional constant κ. The torsion fibre provides a restoring force to the rotor and sample. Under equilibrium conditions

eqn. 2.5.ii $$mB\sin\theta = \kappa\Delta\theta,$$

where, $\Delta\theta$ is the angular deflection of the sample due to the applied field. A measurement of $\Delta\theta$ is then equivalent to a measurement of the magnetisation of the sample. It is assumed that $\Delta\theta$ is small enough to keep θ approximately constant.

The magnetometers used at Exeter are of 'differential capacitor' design (Fig. 2.5.ii). The principle of operation of a differential capacitor torque magnetometer is that an angular deflection of the rotor causes an imbalance in the capacitance between the rotor and the plates beneath (stators), which results in a current flowing from the rotor through the torsion fibre to earth.

The rotor is flat on one side upon which a silver or gold film is deposited. The rotor is suspended by a torsion fibre over a split plate, which forms two capacitors with the rotor. The other side of the rotor has two tapered edges pitched at 20° to the horizontal meeting to form a vertex along the axis of the rotor. It is to this vertex that the torsion fibre is attached. A fine gold wire bonded to the metallic film with electrodag makes electrical contact between the rotor and the torsion fibre (typically made of fine phosphor bronze ribbon). The current that flows as a result of an imbalance between the

capacitor plates is proportional to the angular deflection $\Delta\theta$, and hence a measurement of the current is equivalent to a measurement of the torque of the sample (eqn. 2.5.ii).

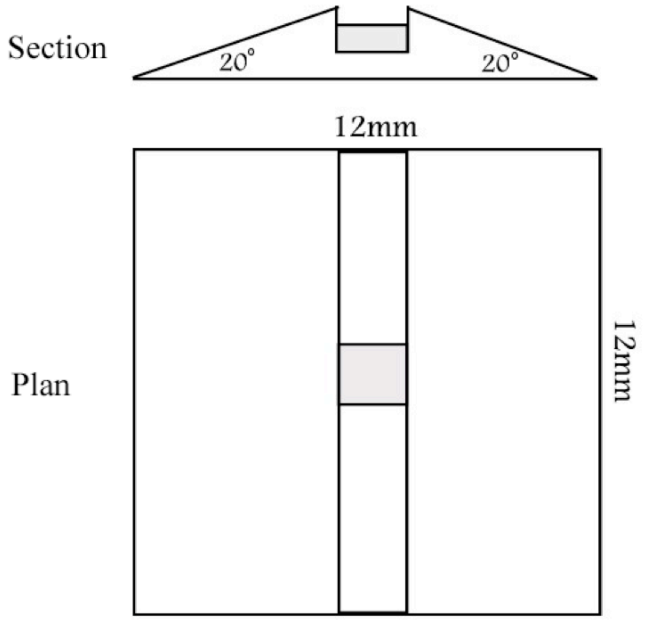

Fig. 2.5.i Schematic of the rotor currently used for magnetometry experiments at Exeter, the torsion fibre is attached to the 'pedestal' coloured grey in the diagram.

Fig. 2.5.i shows the rotor used for magnetometry experiments, the rotor is equipped with two faces for mounting samples. The sample is mounted on one face and a 'dummy' sample is mounted on the other. The dummy sample is of equivalent size and mass, however the dummy does not contain a 2DES. The dummy sample would be made from the same bulk semiconductor as the sample under investigation. The dummy sample not only balances the rotor but also cancels any torque generated by the magnetisation of bulk semiconductor in the sample.

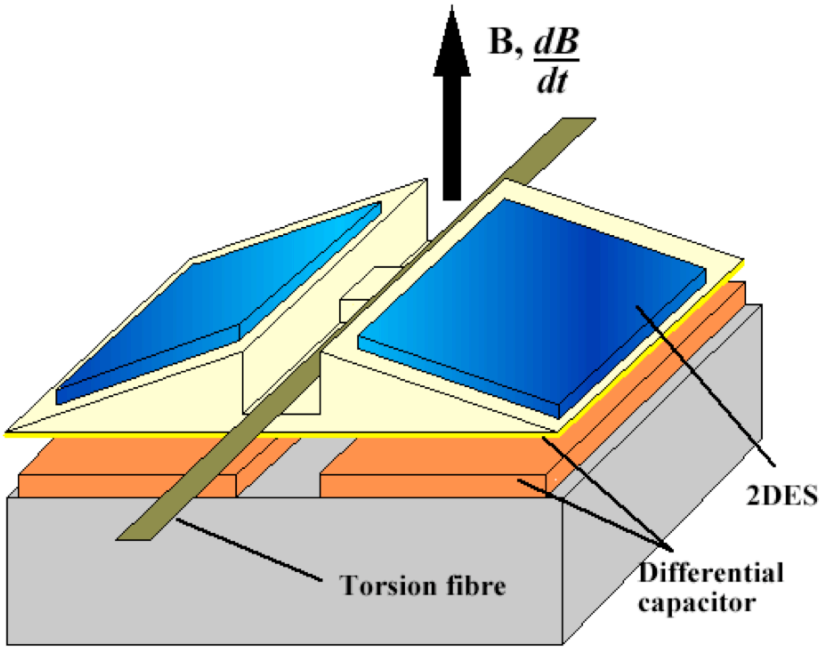

Fig. 2.5.ii Illustration of a differential capacitance torque magnetometer.

The rotor plate is held at 0V by a virtual earth pump and an equal but opposite AC voltage is applied to the stators. A change in capacitance of each side of the magnetometer is detected using an electronic bridge circuit incorporating a virtual-earth transimpedance amplifier. The electronic bridge operates at ~10 KHz and details of its design and specifications have been published by Matthews (2004 (b)). When the system is balanced with a capacitance C_0 on both sides, no current flows from the rotor to the virtual-earth, however if the rotor is imbalanced then the capacitances are no longer equal and a current I will flow from the rotor to earth. The current is proportional to $C_1V_1 + C_2V_2$ where $C_{1,2}$ and $V_{1,2}$ are the capacitances and voltages between each stator and the rotor, however since V_1 and V_2 are equal and opposite the current is proportional to the difference in capacitance between the two sides, $I \propto 2\Delta C$ ($C_1 = C_0 - \Delta C$, and $C_2 = C_0 + \Delta C$).

The rotor and the two stator plates are part of a magnetometer assembly that is mounted in the mixing chamber of a dilution refrigerator below the phase boundary. The magnetometer allows the two stator plates to be moved for easy access to the rotor and to alter the sensitivity of the measurement. The stator plates can either be moved by hand or by using piezo-electric stick-slip motors for fine adjustments. Four piezo-electric actuators are present in the magnetometer allowing the two stator plates to be

tilted with respect to the rotor to compensate for any imbalance in the mass on either side of the rotor.

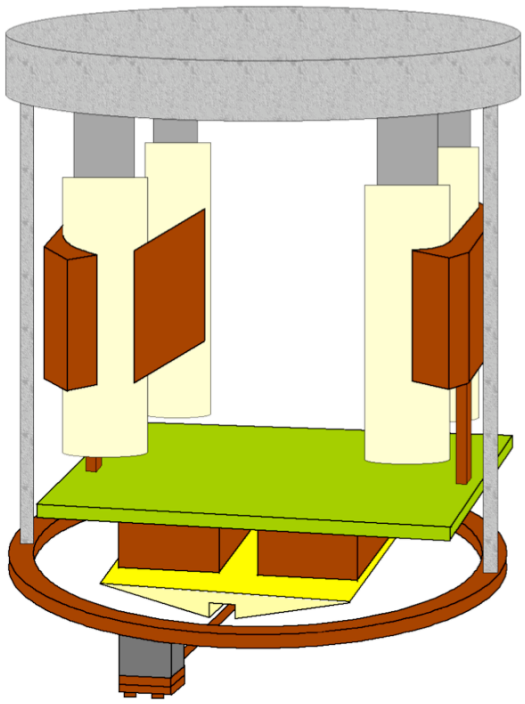

Fig. 2.5.iii Illustration of magnetometer assembly, piezo-electric stick-slip motors control the separation and angle of the stator plates with respect to the rotor.

Fig. 2.5.iii shows an illustration of the magnetometer assembly used for standard magnetometry experiments. As shown in the figure the rotor is suspended 'upside down' by a phosphor bronze torsion fibre below the two stator plates. The stator plates are attached to a 'stycast' resin sheet, the distance and angle of which is controlled by the four piezoelectric actuators. Two phosphor bronze 'pucks' move up or down the ceramic tubes housing the piezoelectric actuators when the actuators are activated. When a voltage is applied to the actuators they will either lengthen or contract (along the long axis of the actuator). The tension between the puck and the piezoelectric actuators is set such that a slow movement of the actuator will move the puck also, but a fast movement will cause the puck to slip. Thus a saw-tooth waveform applied to the actuators allows the pucks to be moved up or down the actuator tubes at will and control the distance and angle of the stators with respect to the rotor.

Phosphor bronze clamps on either side of the magnetometer hold the torsion fibre in place. PVC spacers insulate the clamps and hence the rotor from the rest of the magnetometer, allowing wires to be attached to the clamps to carry the signal to the top of the dilution refrigerator. All the materials used to construct the magnetometer are

non-magnetic, also the materials have to be carefully chosen so that during cool-down thermal contraction does not cause joints between components to loosen or move. Notice that the torsion fibre and the clamps are both made of phosphor bronze so that the torsion fibre does not move as it contracts during the cooling process.

Typically the capacitance between the rotor and a stator is in the range 2 to 5 pF after cooling to 4.2 K (nearly all materials have finished contracting once the temperature reaches 4.2 K). A capacitance of 5 pF between two plates of area 5×10^{-5} m^2 (the area of a stator plate) equates to a distance of less than 90 μm. This yields an overall sensitivity on the order of 2×10^{-7} N m / pF, this gives a resolution in terms of a magnetic moment on the order of 1×10^{-11} J/T or $\sim 1.1 \times 10^{12}$ μ_B at a field of 1 T. Matthews (2004 (b)) gives a more detailed description of the magnetometer assembly and technical specifications experimental apparatus. The absolute sensitivity of the magnetometer is calculated to be 6.5×10^{-12} N m Hz$^{-1/2}$.

The resolution of the magnetometer is limited by the background mechanical and electronic noise in the system. Fig. 2.5.iv shows a plot of magnetometer noise for the system at zero magnetic field for the dilution refrigerator circulating and in single shot mode. The noise level for single shot mode corresponds to a torque $\sim 2 \times 10^{-11}$ N m centred about zero.

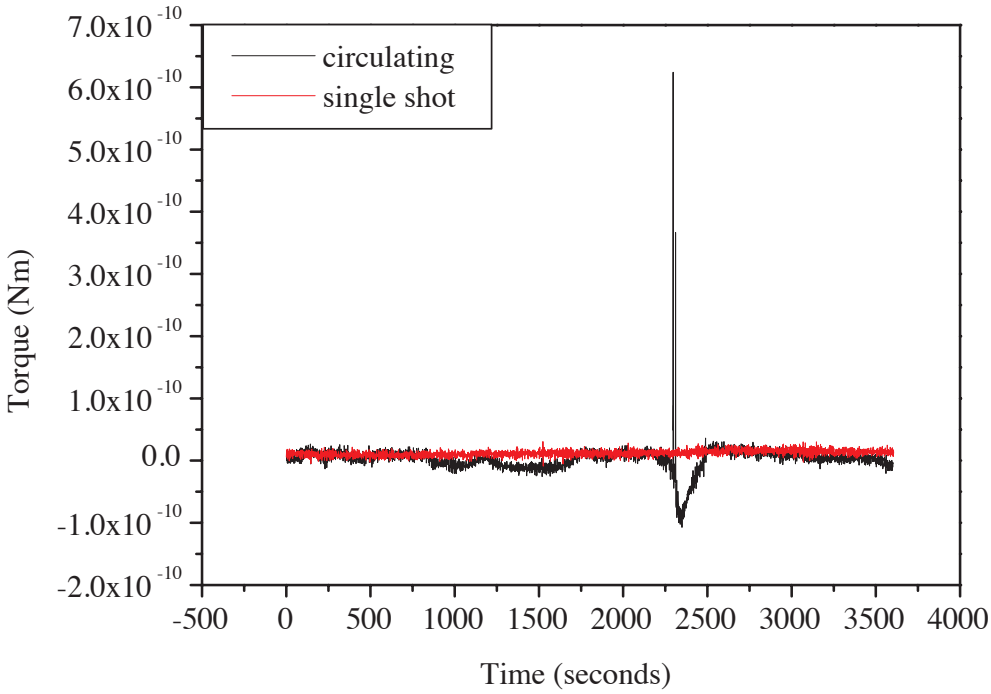

Fig. 2.5.iv Plot of magnetometer noise against time. The black plot is with the refrigerator circulating, the sharp spike is due to the pneumatic piston closing a cryovalve as the sorption pump cycle changes. The red plot is with the refrigerator in single shot mode. The measurements were carried out at zero magnetic field with a 1 second interval per point and a lockin amplifier time constant of 300 ms.

2.6 Cantilever magnetometry

In order to measure the magnetisation of smaller samples a new technique was investigated to replace the more conventional torsion fibre magnetometer used at Exeter. As a result micro-machined cantilevers were fabricated from wafers of GaAs with a 2DES mesa situated at the end of the cantilever. The cantilever mounted at an angle to the external magnetic field would experience a torque generated by the 2DES in the same way as the torsion balance magnetometer explained previously. It was decided to measure the torque capacitively rather than optically or by measuring the piezo-electric current. Gold was evaporated on the underside of the cantilever in order to form one of the capacitor plates, also a calibration coil was evaporated onto the top of the cantilever. The calibration coil can be used to create a known magnetic moment and hence calibrate the device.

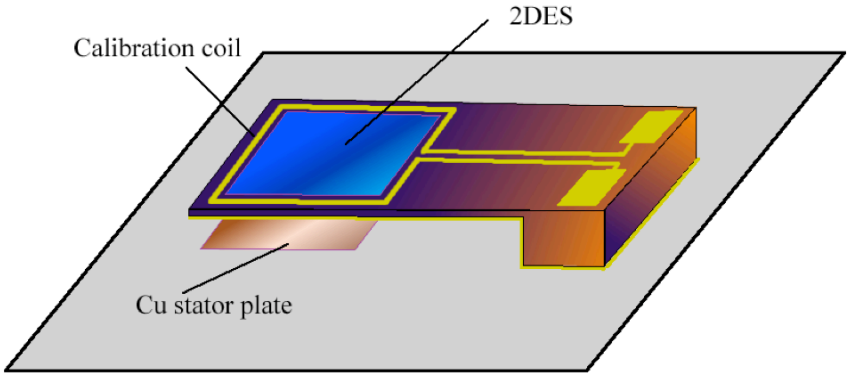

Fig. 2.6.i Illustration of the micro machined cantilever device, the 2DES is located at the end of the cantilever and is enclosed by the calibration coil. Also shown is the copper stator plate forming the capacitor with gold underside of the cantilever. The GaAs surround has been omitted for clarity.

The stator plate was fabricated from a piece of copper clad fibreglass board using standard PCB prototyping techniques. The plate has an area equivalent to that of the 2DES mesa on the cantilever and a thickness of ~20μm. In order to make electrical contact with the stator plate a wire was soldered to the underside of the copper plate after milling through the fibreglass board by hand (milling machines damage the copper sheet). The cantilever was contacted to by locating a wire within a channel in the fibreglass board and back filling with solder. The surface of the solder is made level with the rest of the board so that the cantilever can be 'stuck down' with conductive silver paint. This method has the benefit that none of the wires have a direct line of sight to the 2DES or the stator plate to minimise capacitive coupling. The whole assembly is mounted within the dilute phase of a dilution refrigerator at an angle of 20° to the applied magnetic field. Fig. 2.6.ii shows magnetisation measurements taken with the cantilever. Since there is only one stator plate, data can be recorded using a commercial bridge to measure the capacitance between the two plates or as in the case of the data shown in Fig. 2.6.ii a reference capacitor at room temperature was used so that the differential capacitance bridge [Matthews (2004 (b))] can be used.

Using the method stated above the sensitivity of the magnetometer is fixed and is governed by the distance between the stator plate and the gold underside of the cantilever. The measured sensitivity of the cantilever was 1.1×10^{-8} N m / pF for a 10 μm thick cantilever. This is approximately 18× more sensitive than the torsion balance magnetometer detailed earlier in the chapter. However this increased sensitivity

is balanced against the decreased size of the sample used, a smaller number of electrons means a smaller magnetic moment **m** and weaker dHvA oscillations. The area of the 2DES mesa is $6.25 \times 10^{-6}\text{m}^2$ as opposed to the area of a 2DES ($5 \times 10^{-5}\text{m}^2$) that can be put on the rotor used for the torsion balance magnetometry. This means that despite the cantilever magnetometer being sensitive to far smaller torques the decreased size of the 2DES means that the device is only effectively twice as sensitive as the current torsion balance magnetometer. Using thinner cantilevers to increase the sensitivity or decreasing the width of the cantilever between the 2DES mesa and the pivot point to make more of a paddle shape could overcome this, as would moving the capacitor plates closer together. However, all of these methods make the cantilever less robust and more susceptible to damage.

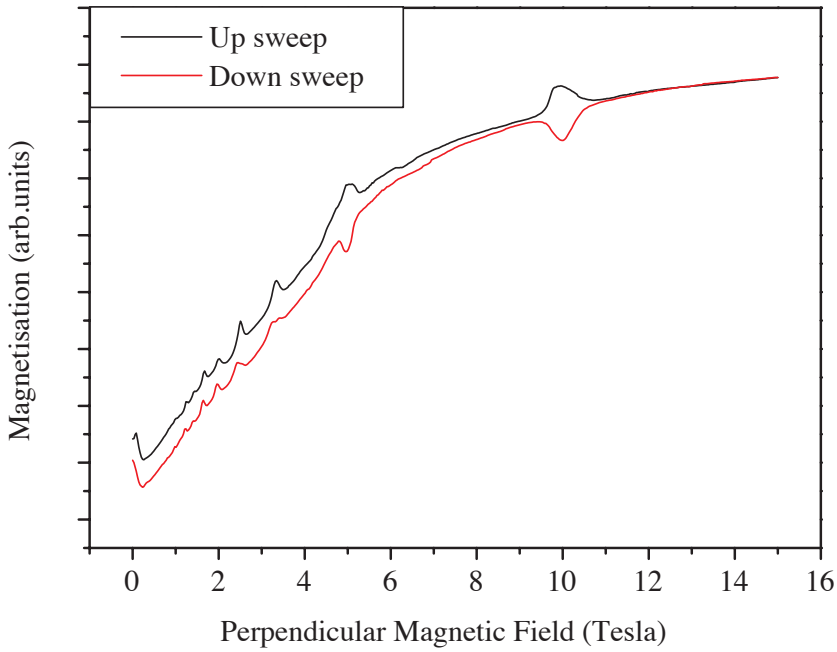

Fig. 2.6.ii Plot of magnetometer output showing up and down magnetic field sweeps at a temperature of ~30mK. The oscillations are dHvA with induced circulating current peaks at higher fields.

2.7 Magnet stability

The superconducting solenoid used for these experiments has two different modes of operation, persistent mode and non-persistent mode. In persistent mode the switch heater is turned off and the supercurrent is free to flow through the solenoid in a closed

loop. This allows the magnet power leads to be ramped down and thus reduce helium boil off. In non-persistent mode the switch heater in on and current flows from the magnet power supply into the cryostat through the solenoid and back to the magnet power supply. In theory when the magnet is in persistent mode the supercurrent should be persistent with no noticeable decay for many years. However, the construction of the superconducting magnet used for the experiments presented in this thesis uses a heater switch of lower quality than those found in machines such as magnetic resonance imaging (MRI) machines. The current experiences some resistance while the magnet is in persistent mode. The stated values for current decay are of the order 1 part in 10^4 per hour for the system used where as MRI type switches can achieve 1 part in 10^7 per hour [Oxford Instruments]

The sensitivity of the experiments and the timescale over which the decay of circulating currents in the QHE regime and the study of the dHvA in graphite (see chapters 4 and 5 respectively) were observed meant that the field stability of the superconducting magnet became an issue. Initial experiments were carried out with the magnet in persistent mode to allow longer experiments by reducing helium boil off from the main bath. However, it was found that the magnetic field decreased over a number hours, this was assumed to be due to resistive losses as the super current passes through the switch heater. Using a Hall probe located on the outside of the cryostat to measure the magnetic field strength, it was noted that the magnetic field decreases with time when the magnet is in persistent mode.

The voltage output by the Hall probe (type SS94A2D) varies linearly with variation in magnetic field [RS Components]. By measuring the change in Hall voltage for a known change in magnetic field, it was found that the Hall voltage varies by 0.11625 VT^{-1}. Hence a measured change in voltage can be converted to a relative change in magnetic field. The decay of the magnetic field with the magnet in persistent mode is shown in Fig. 2.7.i the field is reduced by approximately 2.7×10^{-3} T over a 12-hour period.

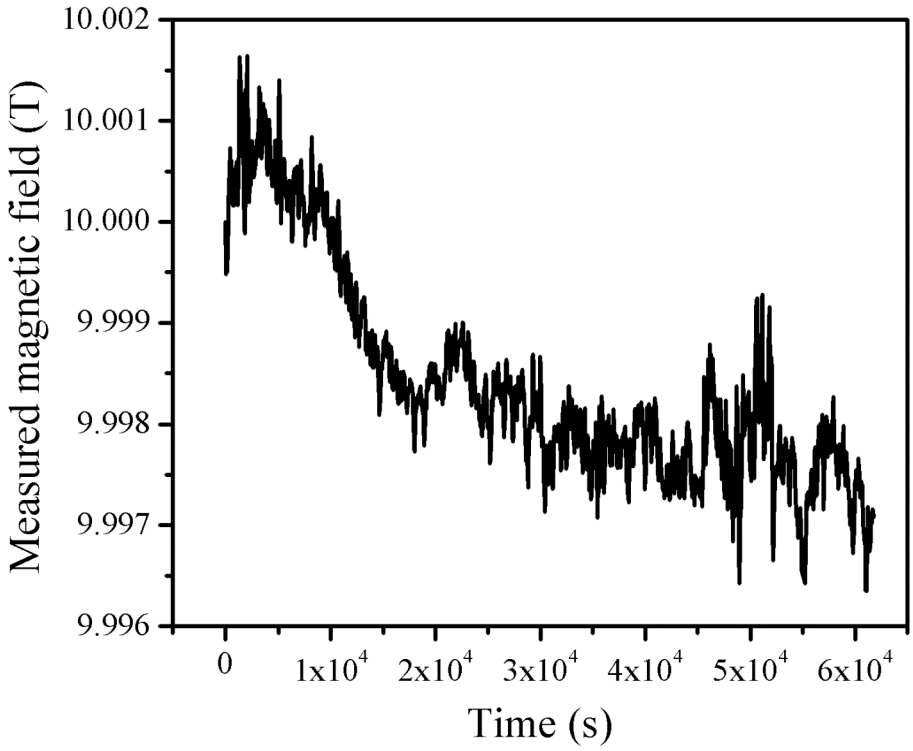

Fig. 2.7.i Plot of relative change in magnetic field versus time for the magnet in persistent mode at 10 T. The rate of decay of the magnetic field is approximately 2.7×10^{-3} T in the first 12 hours, this is within reasonable agreement with the stated value of 1 part in 10^4 per hour [Oxford Instruments].

Variation of the magnetic field can affect the decay of the induced currents in several ways. The magnitude of an induced current in the QHE regime is highly sensitive to the value of the filling factor ν and hence the magnetic field. Thus a change in magnetic field can make a circulating current decay faster or slower than would be expected depending upon the direction of the inducing time varying magnetic field *dB/dt*. If the circulating current was induced by sweeping from below in magnetic field then a decrease in the magnetic field will cause the circulating current decay faster than it would if the magnetic field were static. The decreasing magnetic field has the effect of attempting to induce a current in the opposite direction, thus changing the polarity of the induced magnetic moment and the observed eddy current peak. However, since *dB/dt* caused by the decaying magnetic field is small the result is to make the previously induced current smaller and give the illusion of an increased decay rate.

Conversely if the magnetic field is swept from above then the decrease in magnetic field over time slows the decay of induced currents as shown in Fig. 2.7.ii. This is due to a circulating current being continually induced by the slowly decreasing magnetic field.

Thus, reinforcing the induced circulating current and giving the illusion of a slower current decay rate. If *dB/dt* is large enough the rate of induction can become greater than the rate of the current decay, in which case the decay can be observed to change direction as the magnitude of the induced current increases. This is simply due to an increased torque from the larger induced current.

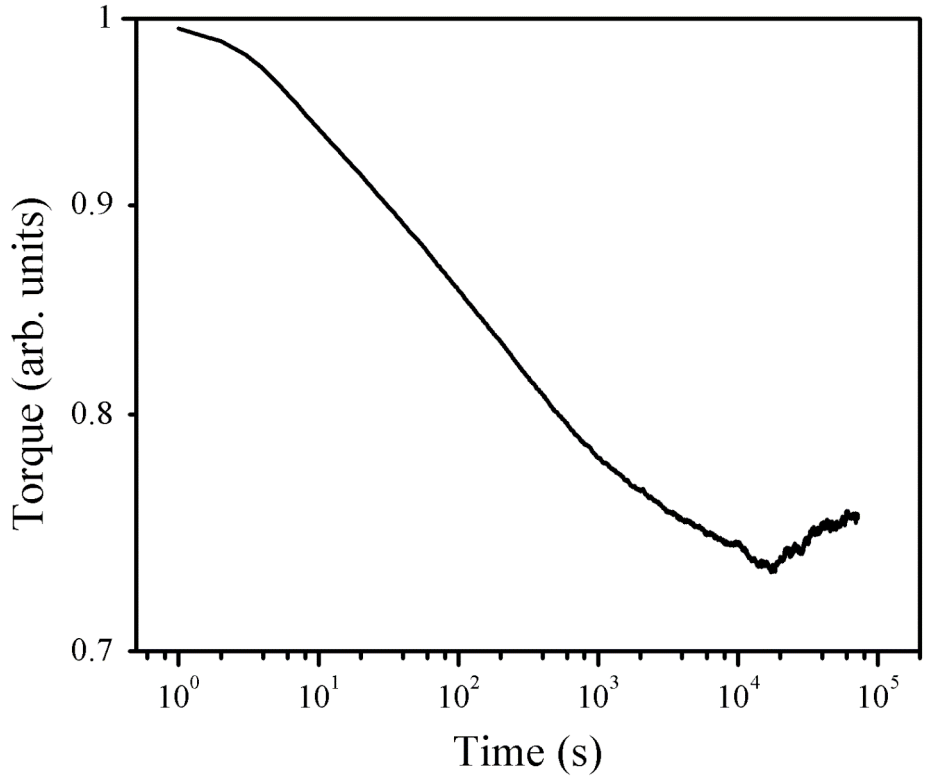

Fig. 2.7.ii Plot of the decay of an induced current within a 2DEG showing an increase in the observed torque as the decrease in magnetic field exceeds the decay of the current. Shown on a logarithmic plot for clarity.

While there are likely to be other factors involved in the observed behaviour such as drift in the electronics involved in measuring the torque, this 'increasing' circulating current is only observed when the magnet is swept from above. This indicates a systematic error associated with the decay of the magnetic field, this is reinforced by the observed behaviour of the current decay increasing when the magnetic field is swept from below (Fig. 2.7.iii).

It was found that the magnetic field was much more stable if the magnet is kept in non-persistent mode with the switch heater on. While this increased the boil off of helium from the main bath and hence increased the mechanical noise, experiments could still be run for a sufficient amount of time to observe the current decays in detail. Using this method the magnet power supply unit is responsible for the magnetic field stability

when operating in non-persistent mode. The magnet power supply is stated to have a current stability of ± 3 mA/°C and also ± 3 mA/12 hours [Oxford Instruments]. The conversion factor between supplied current and generated magnetic field is 0.1605 T/A. This is equivalent to ± 4.8 × 10^{-4} T per °C per 12 hours. Assuming the temperature of the unit remains constant the stability of the magnetic field in non-persistent mode is almost an order of magnitude better than with the magnet in persistent mode. There is however the problem that the magnetic field can both increase and decrease as a function of both time and temperature making it more difficult to distinguish between physical features in the data and drift in the magnetic field.

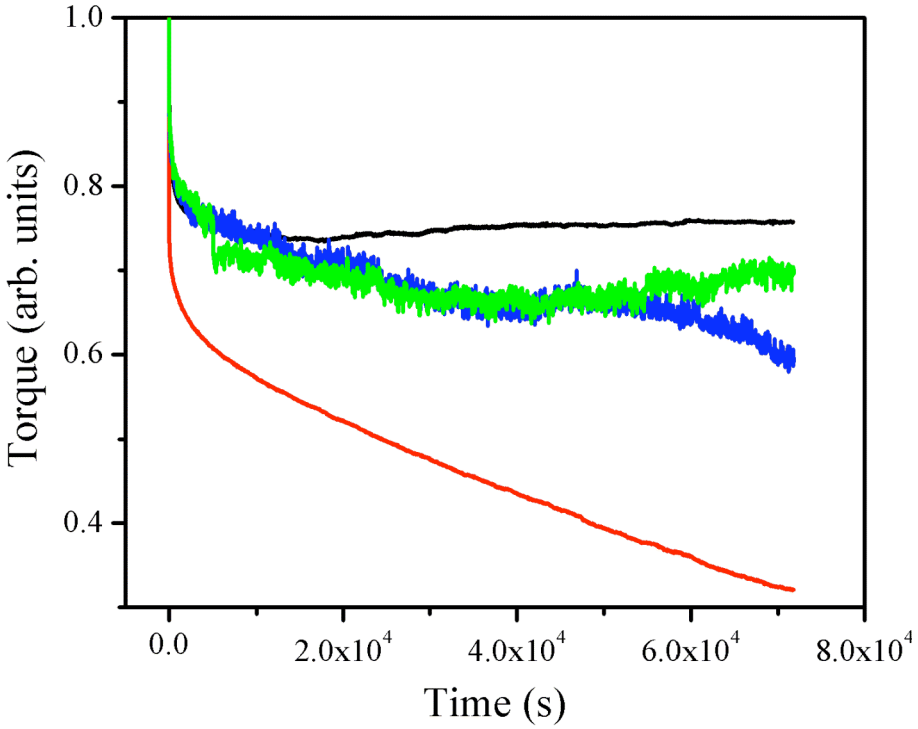

Fig. 2.7.iii Comparison of eddy current decays with the magnet in different modes. The black and red traces are with the magnet in persistent mode the eddy current was approached from above and below respectively. The blue and green traces are with the magnet in non-persistent mode the approach being from above and below respectively.

Fig. 2.7.iii shows the influence of the magnet mode and direction of approach on the rate of eddy current decay. Note the increased noise on the non-persistent mode decays due to the increased helium boil off.

In addition to the decay of a static field the variation in *dB/dt* as the magnetic field swept between two values is also important. During the study of the dHvA effect in graphite (see chapter 5) it was noticed that the magnetisation peaks associated with a

given filling factor ν were not aligned between up and down sweeps of the magnetic field.

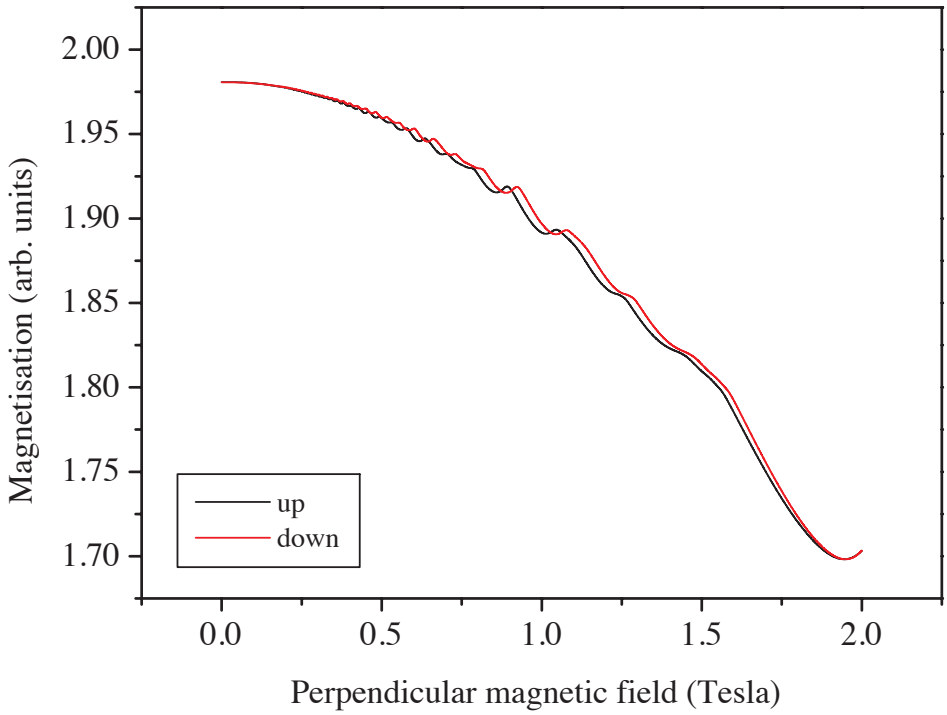

Fig. 2.7.iv Plot of observed dHvA oscillations in graphite for both directions of magnetic field sweep.

Fig. 2.7.iv above shows the measured magnetisation of a graphite sample versus perpendicular magnetic field. The black trace corresponds to an up sweep or a positive *dB/dt* where as the red trace corresponds to a down sweep or a negative *dB/dt*. Note the disparity between the different traces. The offset between the up and down sweeps is not constant indicating that the effect is not simply due to the magnet power supply reporting the magnetic field incorrectly. Features in the data align at the start of the magnet sweep and at the end; this implies that the observed disparity in the central regions of the data is due to a varying magnetic field sweep rate. For this effect to be observed the magnet power supply has to report a value different from the true value of the magnetic field. The power supply reports the magnetic field by measuring the voltage across a 1 KΩ shunt resistor at the output. The measured voltage and hence current is converted to a magnetic field using the conversion factor for the system 0.1605 T/A [Oxford Instruments]. This however assumes that the conversion factor is

constant for both directions of magnetic field sweep. Using a Hall probe attached to the bottom of the cryostat directly below the centre of the magnet the magnetic field was measured directly and plotted against the magnetic field reported by the magnet power supply unit.

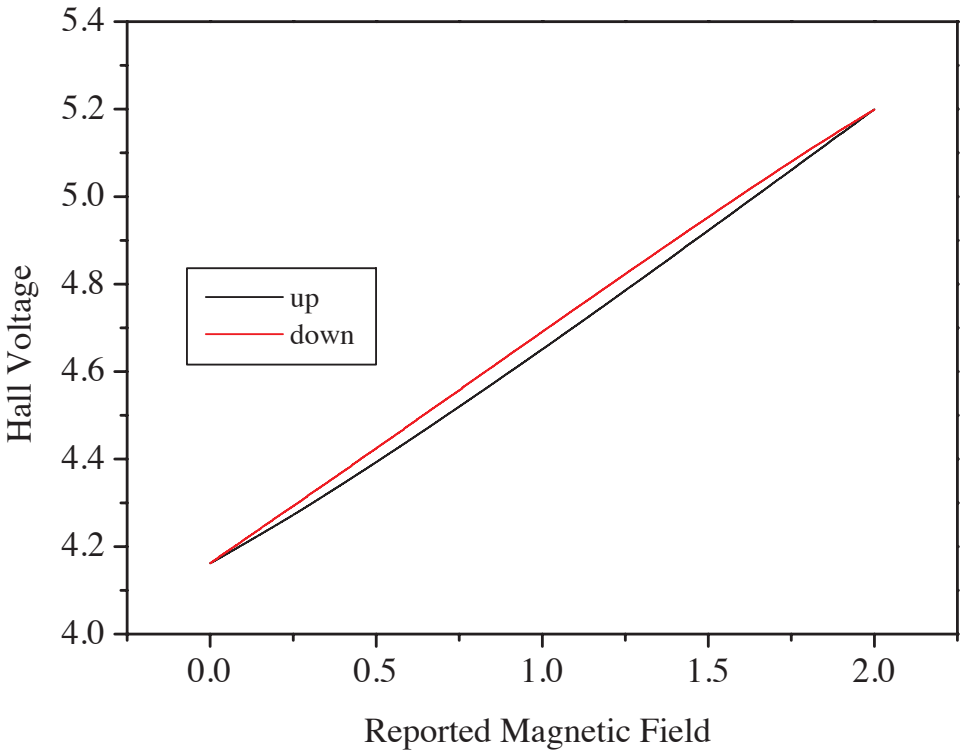

Fig. 2.7.v Plot of Hall voltage versus reported magnetic field for both directions of magnetic field sweep. The field sweeps have the same ramp rate and ambient room temperature. The down sweep followed the up sweep with a pause of 3 minutes in between.

The Hall probe (type SS94A2D) used to measure the magnetic field outputs a Hall voltage that varies linearly with magnetic field to within 0.8% typical (1.5% max) over the range $0 \rightarrow \pm 2500$ Gauss with a sensitivity of 1.00 ± 0.2 mV/Gauss [RS components]. However, as shown in Fig. 2.7.v above Hall voltage is not linear with reported magnetic field, what is also apparent is that there is some hysteresis associated with the superconducting magnet. Upon close inspection the Hall voltage for the down sweep is more linear that the equivalent up sweep with only a slight curvature at the beginning of the sweep, the up sweep on the other hand has more of an exponential curvature. The more linear nature of the down sweep suggests that there is perhaps

some remnant field within the magnet that not only resists the changing magnetic flux but also has more of an effect on a positive *dB/dt* than a negative one. The shape of the curves shown in Fig. 2.7.v was unaffected by the range of the applied magnetic field and similar results were obtained for down sweeps performed several hours after the previous up sweep and also for up sweeps closely following a down sweep, indicating that this is an effect associated with only the superconducting magnet and not with any induced currents within the normal metal of the cryostat or the dilution refrigerator. The effect is only very weakly affected by a hundred-fold increase in *dB*/*dt* and then only the up sweep appears to be affected, the down sweep remains stable with its near linear dependence (not shown). The linear nature of the central region of the down sweep data meant that down sweeps were used to study the dHvA effect in graphite. By extending the observed magnetic field beyond the region of interest so that all the data of interest lay within the linear region, any offset between the 'real' magnetic field and the one reported by the magnet power supply can be corrected by a simple addition of a constant magnetic field to the data. The 1/*B* periodicity of the dHvA can be used as a guide for the magnitude of the correction.

2.8 Summary

In this chapter we have discussed the experimental apparatus and the some of the experiments that can be performed using them. The limitations of the 'torsion balance' magnetometry method have been discussed, as have the uncertainties involved in performing experiments at static and sweeping magnetic fields. This allows for a better understanding of the results presented in later chapters of this thesis.

3 Magnetisation measurements of sample A2268

3.1 Introduction

The aims of the experiments reported in this chapter were to investigate the shape of the Landau level broadening and to determine if the width and background density of states (DOS) varies with temperature by measurement of the de Haas – van Alphen (dHvA) effect. This information should give a better indication as to the origins of disorder in 2D electron systems responsible for the broadening of the Landau levels from the ideal delta functions in a 'perfect' sample.

There are many origins of the disorder responsible for Landau level broadening in 2DES's. Vacancies and impurity atoms at lattice sites alter the electronic structure of the 2D system and can cause scattering of electrons within the sample. Interstitial atoms, dislocations in the lattice structure and phonons can all produce scattering events within the electron system. The use of molecular beam epitaxy (MBE) to grow samples at ultra high vacuum allows samples to be grown with very few defects within the crystal structure. Also the use of modulation doping, to create the heterojunction in which the 2DES is located significantly, reduces the number of impurities that are available to scatter electrons. However, long-range remote impurity scattering can still occur as a result of the impurities used in the modulation doping. Phonons can cause the momentum change needed for electron scattering but they are generally considered negligible at the temperature the experiments were performed at. Sample A2268 used for the measurements reported in this chapter is a multiple quantum well sample and as such there is likely to be some inhomogeneity between the different quantum wells due to surface affects and possible crosstalk between the different quantum wells.

In a perfect sample at absolute zero temperature (as discussed in chapter 1) the dHvA effect manifests itself as 'sawtooth' oscillations periodic in inverse magnetic field, these are a result of the delta function Landau levels. The oscillations as shown in Fig. 3.1.i are of equal magnitude with the high field side being a sharp change in the magnetisation of the sample as a Landau level is emptied. The effect of finite temperature and disorder is to broaden the delta function Landau levels into finite Gaussian functions.

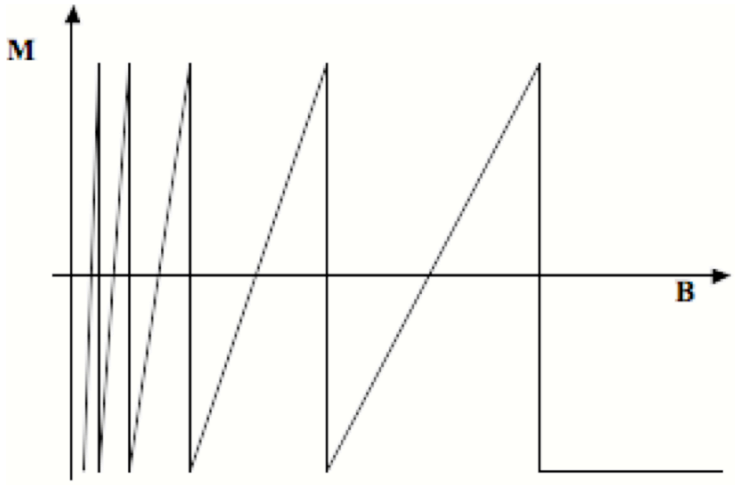

Fig. 3.1.i Illustration of the dHvA effect in a perfect sample at absolute zero.

Careful measurements of the dHvA effect can yield information about the shape and width of the broadened Landau levels and the presence of a background density of states. At small magnetic fields the finite width of the Landau levels causes an overlap between subsequent Landau levels. Thus one cannot clearly define when a Landau level empties as the magnetic field is increased so no dHvA oscillations are observed. The finite temperature can cause the low field oscillations to be 'washed out' as $k_B T \approx \hbar\omega_c$ and electrons are able to transfer between Landau levels.

In order to extract useful information about the density of states from dHvA oscillation a model is needed. The two main models that are used to describe the broadening of the DOS [Potts (1996)] both assume an array of Landau levels periodic in energy and symmetric about $E = 0$ with a width independent of the Landau level index, n. The first model gives a Gaussian broadening of the DOS $g(E, B)$. Since the Landau levels are periodic about $E = 0$ and there is an infinite number of allowed energy levels, the density of states has to be summed over all possible values of n.

eqn. 3.1.i
$$g(E,B) = \frac{2eB}{h}\frac{1}{\Gamma\sqrt{2\pi}}\sum_{n=-\infty}^{\infty}\exp\left(\frac{-(E-E_n)^2}{2\Gamma^2}\right),$$

where E_n is the energy of the n^{th} Landau level given by $E_n = (n + ½)\hbar\omega_c$ and ω_c is the cyclotron frequency $\omega_c = eB/m^*$. The Landau level width Γ is assumed to vary as a function of magnetic field B,

eqn. 3.1.ii $$\Gamma(B) = \Gamma_0 B^p,$$

where Γ_0 is a broadening parameter that varies depending on the line shape used. For the Gaussian model $\Gamma_0 = 5W/6$ and for the Lorentzian model $\Gamma_0 = W/2$, where W is the full width at half maximum of the DOS [Gornik (1985)]. This conforms to theory and experimental observations [Potts (1996)] and p is assumed to be either $p = 0$ or $p = ½$. The $B^{½}$ dependence of the width Γ can be attributed to the presence of short-range potential scattering as proposed by Ando [1974]. The second model assumes a Lorentzian line shape to the broadened DOS given by;

eqn. 3.1.iii $$g(E,B) = \frac{2eB}{h}\frac{1}{\pi}\sum_{n=-\infty}^{\infty}\frac{\Gamma}{(E-E_n)^2+\Gamma^2},$$

The Gaussian DOS line shape comes from theoretical arguments [Wegner (1983)] where the density of states of two-dimensional electrons is calculated in the presence of a strong perpendicular magnetic field and white-noise potential. The Lorentzian DOS line shape comes from the experiments by Ashoori [1992] who found that a Lorentzian line shape fit well to the measured DOS whereas the Gaussian line shape required a background DOS equal to half the zero field DOS to account for the inter Landau level DOS, while the Lorentzian line shape provided a better fit with no background DOS. There have however been numerous reports of experimental data, which support either model.

The presence, if any, of background DOS between Landau levels also warrants investigation, especially since the value of the background DOS between Landau levels can affect the interpretation of the DOS line shape. The background DOS can be characterised as the parameter ξ representing the magnitude of the background DOS as a fraction of the zero field DOS of the sample. The presence of a background DOS is a result of sample inhomogeneities, specifically variations in the carrier density across the sample [Gerhardts (1986)]. Magnetisation measurements are not sensitive to these local variations in the carrier density (n_s), instead the sample average n_s is observed with a constant background n_s and hence a background DOS. This can be incorporated into either the Gaussian model or the Lorentzian model producing a modified expression for the DOS [Potts (1996)].

eqn. 3.1.iv $$g'(E,B) = \xi \frac{m^*}{\pi\hbar^2} + (1-\xi)g(E,B) \qquad (0 \le \xi < 1).$$

It was shown by Shoenberg (1984) that if the DOS is periodic, it is possible to derive analytical expressions for the carrier number density n_s and the grand thermodynamic potential $\Omega(B)$. The grand thermodynamic potential can be calculated using the expression;

eqn. 3.1.v $$\Omega(B) = kT\int_0^\infty g'(E,B)\ln[1-f(E,\mu)]dE\,,$$

where $f(E, \mu)$ is the Fermi function given by

eqn. 3.1.vi $$f(E,\mu) = \frac{1}{1+\exp((E-\mu)/kT)}$$

and μ is the chemical potential. The 2D magnetisation of a sample can be derived using the grand thermodynamic potential and is given by the following equation if the temperature and chemical potential are fixed

eqn. 3.1.vii $$M(B) = -\left(\frac{\partial\Omega}{\partial B}\right)_{T,\mu}.$$

Using the above equations it is possible to derive expressions for the 2D magnetisation $M(B)$ for both the Gaussian and Lorentzian models of the DOS. For the Gaussian broadening model $M(B)$ is given by

eqn. 3.1.viii $$M(B) = -(1-\xi)\frac{2m^*kT}{\pi\hbar^2}\sum_{s=1}^{\infty}(-1)^s \exp\left(-\frac{2[\pi s\Gamma(B)]^2}{(\hbar\omega_c)^2}\right)\left[\left(\frac{\partial I_1}{\partial B}\right)_{T,\mu} + (1-p)\left[\frac{2\pi s\Gamma(B)}{\hbar\omega_c}\right]^2\frac{I_1}{B}\right]$$

and for the Lorentzian broadening by

eqn. 3.1.ix
$$M(B) = -(1-\xi)\frac{2m^* kT}{\pi\hbar^2}\sum_{s=1}^{\infty}(-1)^s \exp\left(-\frac{2\pi s\Gamma(B)}{\hbar\omega_c}\right) \times\left[\left(\frac{\partial I_1}{\partial B}\right)_{T,\mu} + (1-p)\frac{2\pi s\Gamma(B)}{B\hbar\omega_c} I_1\right],$$

where I_1 is given by

eqn. 3.1.x
$$I_1 = \int_0^{\infty} \ln[1-f(E,\mu)]\cos\left(\frac{2\pi sE}{\hbar\omega_c}\right)\mathrm{d}E = \frac{(\hbar\omega_c)^2}{4\pi^2 s^2 kT} + \frac{\hbar\omega_c}{2s}\frac{\cos(2\pi s\mu/\hbar\omega_c)}{\sinh(2\pi^2 skT/\hbar\omega_c)}$$

and

eqn. 3.1.xi
$$\left(\frac{\partial I_1}{\partial B}\right)_{T,\mu} = \frac{1}{B}\left\{-\frac{(\hbar\omega_c)^2}{2\pi^2 s^2 kT} + \pi\mu\frac{\sin(2\pi s\mu/\hbar\omega_c)}{\sinh(2\pi^2 skT/\hbar\omega_c)} + \frac{\cos(2\pi s\mu/\hbar\omega_c)}{\sinh(2\pi^2 skT/\hbar\omega_c)}\left[\frac{\hbar\omega_c}{2s} + \pi^2 kT\coth\left(\frac{2\pi^2 skT}{\hbar\omega_c}\right)\right]\right\}.$$

One can assume that, as the method of measuring the magnetisation of the sample is contactless that the carrier number density n_s is constant as the magnetic field is varied. This implies that it is the chemical potential μ that oscillates with varying magnetic field. Therefore, in order to calculate the 2D magnetisation $M(B)$, the chemical potential $\mu(B)$ must be known for each value of magnetic field B. This can be achieved using a bisection method with the constraint of particle conservation [Potts (1996)]. The carrier number density can be written as

eqn. 3.1.xii
$$n_s = \int_0^{\infty} f(E,\mu)g'(E,B)\mathrm{d}E.$$

The integral can be performed in the same way as for the grand thermodynamic potential $\Omega(B)$ to yield for the Gaussian broadening

eqn. 3.1.xiii
$$n_s = \frac{m^*}{\pi\hbar^2}\left\{I_2 + 2(1-\xi)\sum_{s=1}^{\infty}(-1)^s \exp\left(-\frac{2(s\pi\Gamma)^2}{(\hbar\omega_c)^2}\right) I_3\right\}$$

and for the Lorentzian broadening

eqn. 3.1.xiv $$n_s = \frac{m^*}{\pi\hbar^2}\left\{I_2 + 2(1-\xi)\sum_{s=1}^{\infty}(-1)^s \exp\left(-\frac{2s\pi\Gamma}{\hbar\omega_c}\right)I_3\right\},$$

where I_2 is given by

eqn. 3.1.xv $$I_2 = \int_0^{\infty} f(E,\mu)\mathrm{d}E = \mu + kT\ln(1+e^{-\mu/kT})$$

and I_3 is given by

eqn. 3.1.xvi $$I_3 = \int_0^{\infty} f(E,\mu)\cos\left(\frac{2\pi sE}{\hbar\omega_c}\right)\mathrm{d}E = \pi kT\frac{\sin(2\pi s\mu/\hbar\omega_c)}{\sinh(2\pi^2 skT/\hbar\omega_c)}.$$

A more detailed derivation and explanation of these equations can be found in Potts (1996).

3.2 Experimental details

Sample A2268 is a 10 layer modulation doped GaAs/(Al,Ga)As 2DEG with the following attributes.

$n_e = 4.5 \times 10^{15}$ /m^2 per layer before illumination

$n_e = 6.9 \times 10^{15}$ /m^2 per layer after illumination (red LED)

$\mu = 1.57 \times 10^6$ and 1.93×10^6 cm^2/Vs before and after illumination respectively.

Torque magnetometry experiments were carried out (as described in chapter 2) in the range $0 \rightarrow 17$ T. De Haas – van Alphen oscillations were observed within the temperature range 26 mK to 750 mK. Due to the small size of the dHvA signal all magnetometry experiments were carried out with the dilution refrigerator in single shot mode to minimise mechanical noise. This however leads to a slow temperature increase over many hours and sets the maximum length of time an experiment can take typically an increase of ~10 mK over a period of 8 hours, although this value can vary with the operating temperature of the dilution refrigerator due to variation in the cooling power. This variation in temperature not only manifests itself in a changing zero point in the

data (however this ‘background’ is removed prior to the fitting process) but also in the size of the dHvA ‘saw teeth’ which themselves are temperature dependent, which can lead to complications during the fitting process.

Sample A2268 exhibits both equilibrium oscillations in the magnetisation in the form of dHvA oscillations and non-equilibrium magnetisation peaks centred on integer filling factors produced by circulating induced currents. The two features are distinguishable by the fact that the non-equilibrium features reverse when the magnetic field sweep is reversed. The magnitude of the induced currents varies rapidly with filling factor and the induced currents quickly swamp the small dHvA oscillations. The induced currents are more susceptible to temperature increase than the equilibrium oscillations and they are barely noticeable at temperatures above 1 K. The induced currents can also be removed in most cases by illuminating the 2DES when cold; the mechanism for this though is not understood. Illumination also has the effect of increasing the number density of charge carriers in the sample and their mobility, these effects are not reversible while the sample is still cold. The measurements reported in this chapter focus mainly on the lower field higher filling factor oscillations where the induced currents are smaller and also some measurements after illumination of the sample with an LED in the mixing chamber.

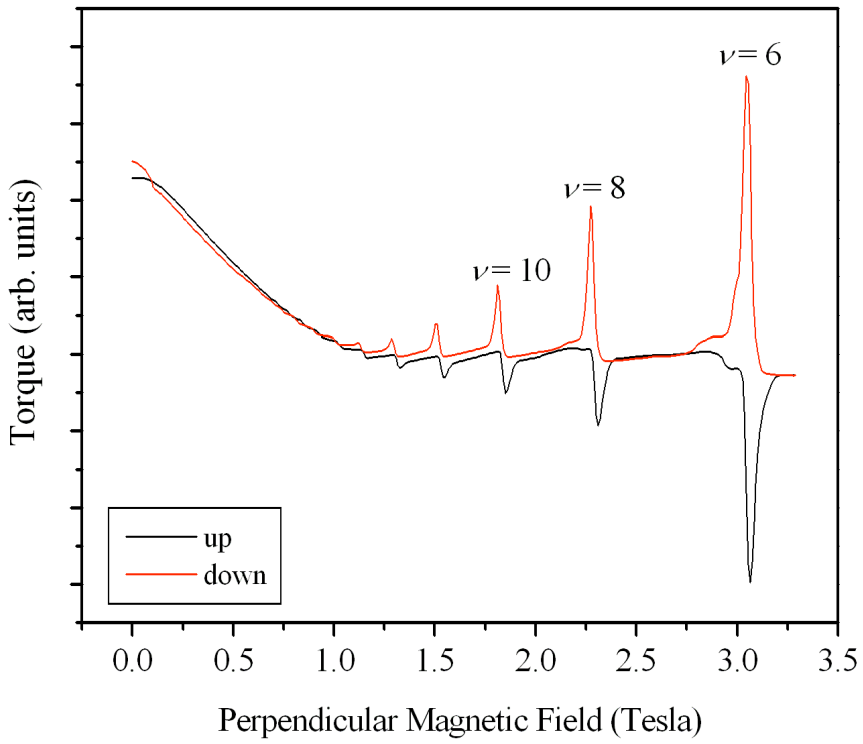

Fig. 3.2.i Raw data output by magnetometer for up and down magnet sweeps at ~30 mK showing de Haas – van Alphen oscillations and reversing induced currents at integer filling factors.

Fig. 3.2.i shows the raw data output from the magnetometer showing filling factors up to $\nu = 6$, notice how the dHvA oscillations continue to lower field than the non-equilibrium induced current features. There is a slight shift in the position of integer filling factor between up and down sweeps. This is due to the hysteresis effect of superconducting magnet system as discussed in chapter 2 and can be removed by shifting up and down sweeps so that the equivalent dHvA oscillations line up and are periodic in inverse magnetic field, however this is easiest to do after removal of the background.

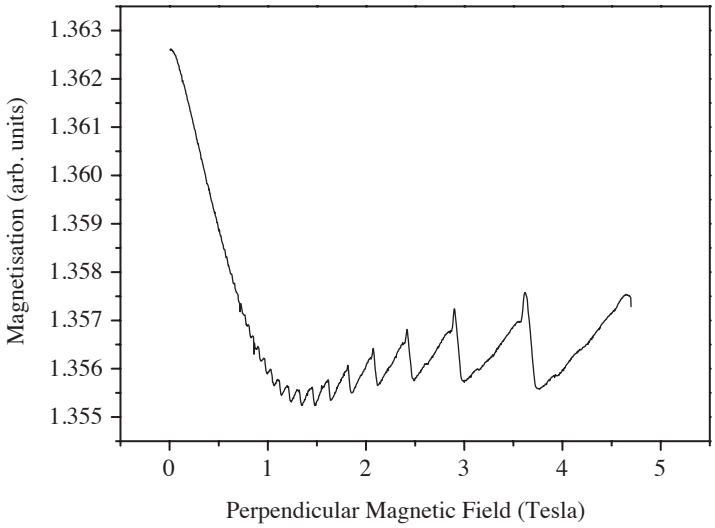

Fig. 3.2.ii Plot of raw data prior to background magnetisation subtraction. The induced currents are minimised compared to those in Fig 3.2.i by the higher temperature of 540 mK ± 10 mK.

Removal of the background involves choosing a range of magnetic field values where the induced currents are significantly small so as not to alter the dHvA oscillations period or magnitude. For this analysis only oscillations where the dHvA peak can be resolved independently from the induced current peak have been considered. This range changes with temperature, larger ranges being available at higher temperatures. A low order polynomial is then subtracted from the data to remove the majority of the

background signal. A spline fit curve is then fit to the peaks of the dHvA oscillations and another to the troughs. The average of these two spline fit curves is then deducted from the data to remove the residual background signal after subtraction of the polynomial. This is possible provided one assumes that the equilibrium dHvA saw teeth oscillate about zero magnetisation.

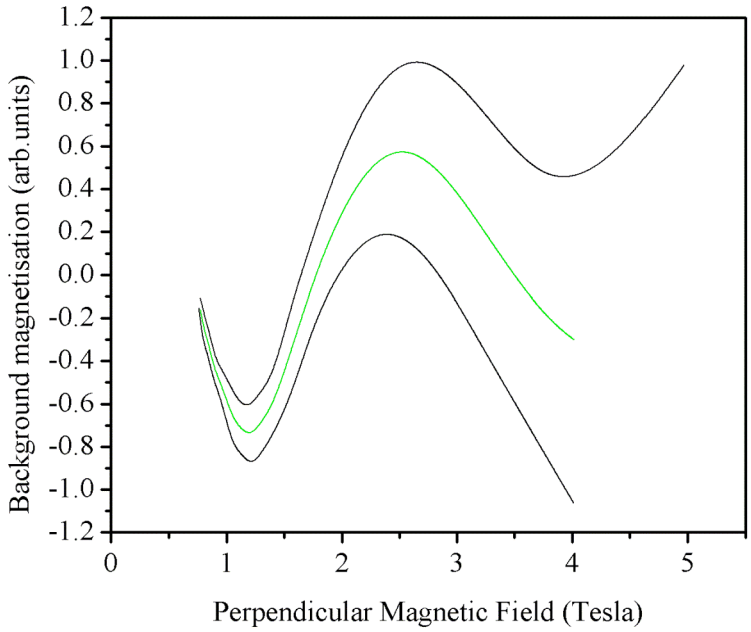

Fig. 3.2.iii Plot of the spline fits to the peaks and troughs of the dHvA (in black) and the average of the two (in green) to be subtracted from the data

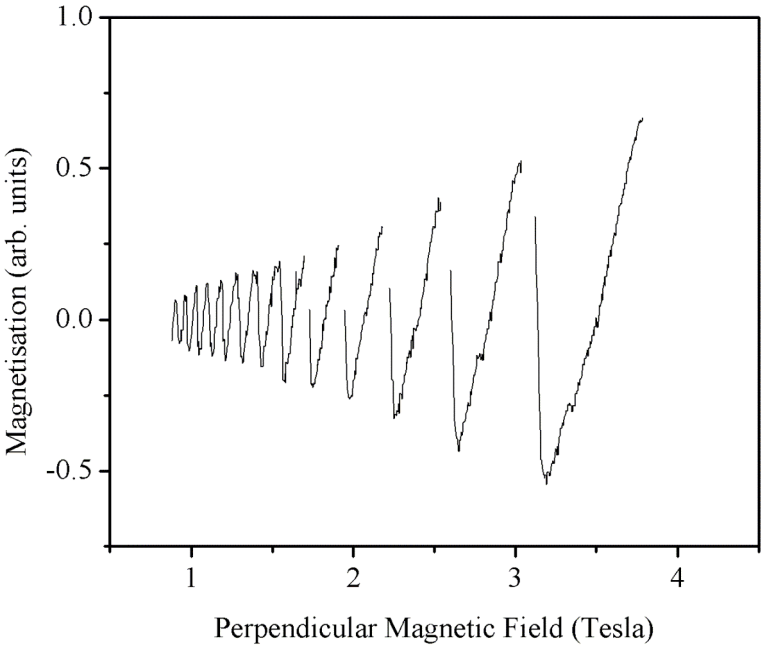

Fig. 3.2.iv Plot of the dHvA data after removal of the background signal. The induced currents have been deleted from the data set so as not to affect the analysis of the dHvA oscillations.

After removal of the background the data needed to be shifted in field to counteract the discrepancies between reported magnetic field and the actual field before any analysis could be performed. In order for the data to be analysed the dHvA oscillations are required to be periodic in inverse field otherwise calculation of the number density becomes difficult. As shown in Fig. 3.2.v the up and down sweeps have been shifted by the same amount and the oscillations line up at higher field values. However, the low field oscillations are misaligned, close examination of the same data on an inverse field scale shows that the down sweep data are indeed periodic in 1/B. For the purposes of the dHvA analysis down sweeps were used for this reason, up sweep data were recorded purely for comparison and to aid the magnetic field shifting of the down sweep oscillations to be periodic in inverse field.

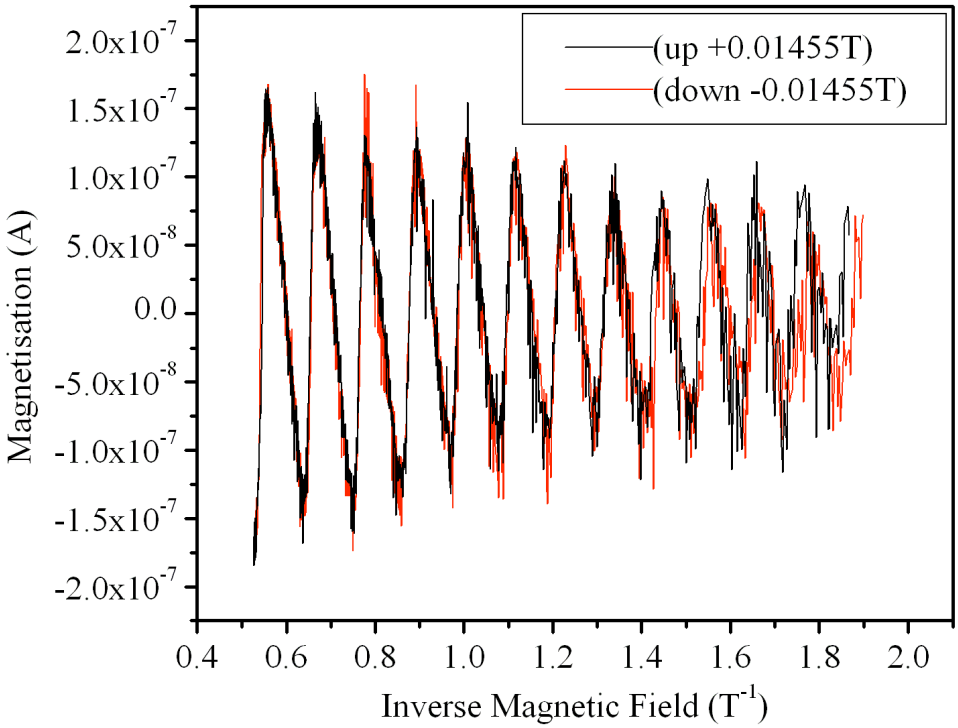

Fig. 3.2.v plot of comparative up and down sweep dHvA oscillations after shifting in field at 640mK ± 20 mK the data are shown plotted against inverse field for clarity. The discrepancy between the sweeps at low field is probably due to the magnet power supply issues discussed in chapter 2. The down sweep data are periodic in inverse field.

The program used to analyse the dHvA oscillations uses the analytical expressions derived in the previous section to generate a dHvA signal for comparison with the data. The program retrieves initial values for the number density n_s, width of the Landau level

Γ, background density of states and a scaling factor. The program then reads the dHvA data and for each value of magnetic field B in the data set calculates $n_s(\mu)$ using eqn. 3.1.xiii and eqn. 3.1.xiv for the Gaussian and Lorentzian broadening models respectively. The Newton Raphson method is used to find the value of $\mu(B, n_s, \Gamma$ and background DOS) which gives the correct value of n_s. These values are then used to calculate the magnetisation $M(\mu, \Gamma$, background DOS) using eqn. 3.1.viii and eqn. 3.1.ix for the Gaussian and Lorentzian models respectively. Next the scaling factor is applied and the mean difference between the modelled magnetisation $M(B)$ and the data is calculated. The downhill simplex method is used to find values of the fit parameters that minimise the errors between the modelled $M(B)$ and the data. An explanation of the downhill simple method can be found in most scientific computing textbooks. The parameter values output by each stage of the downhill simplex method are then passed back to the beginning of the cycle and n_s is calculated. The cycle is repeated until the error between the modelled magnetisation $M(B)$ and the data no longer decreases with each iteration. The final parameter values are output with a plot of the M vs. B curve and a figure of merit for the fit.

3.3 Results

Once the measured torque has been converted to magnetisation with the background removed along with any induced current peaks and the periodicity of the dHvA in inverse field has been checked, then the various models can be fitted to the oscillations. A Labview virtual instrument is used to vary the parameters and fit the models to the magnetisation oscillations as described in the previous section. The parameters fitted were; number density n_e, width of the Landau level Γ, the background density of states between Landau levels and a scaling factor. This was done for both the Gaussian and Lorentzian model of Landau level broadening, also for Gaussian broadening with a $B^{½}$ dependence of the width Γ. The Lorentzian broadening with a $B^{½}$ dependence of Γ was not investigated in detail as Potts (1996) showed that the model produces a poor fit to data, this was confirmed for this sample with fits to preliminary data. De Haas - van Alphen oscillations at 26 mK, 69 mK, 193 mK, 430 mK, 640 mK and 740 mK were analysed.

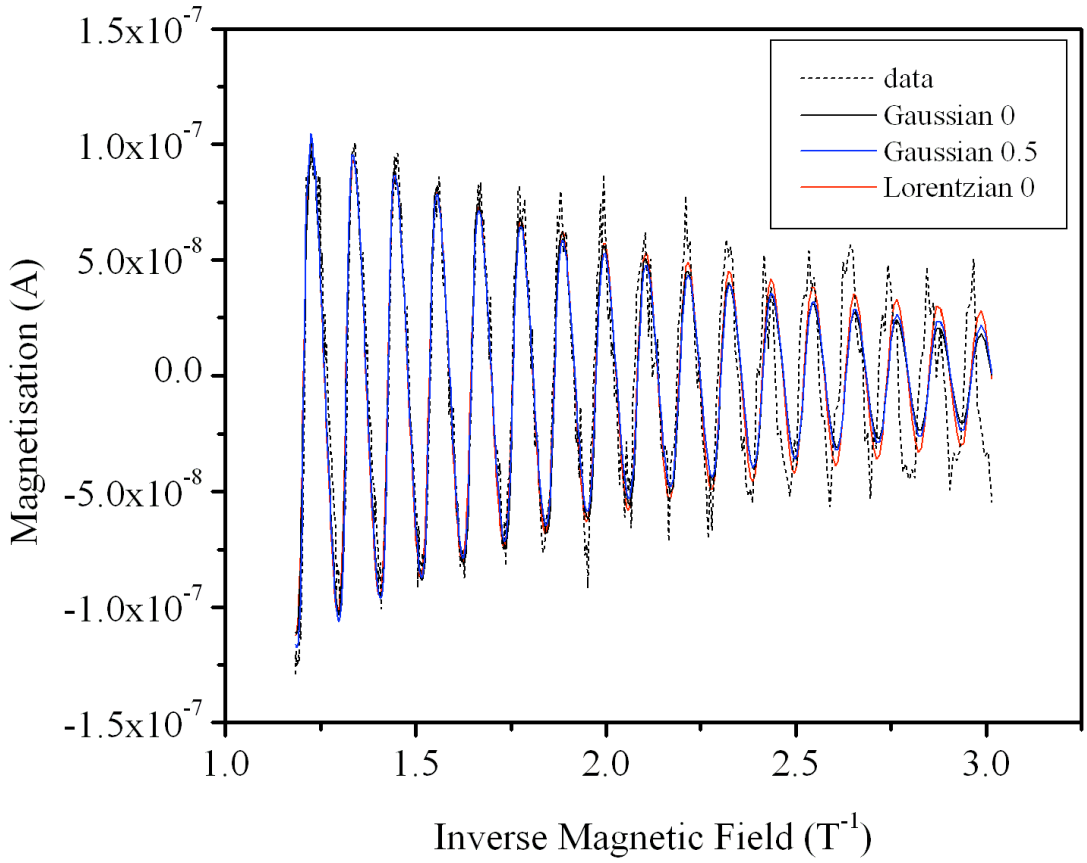

Fig. 3.3.i Plot of dHvA data at 69 mK ± 10 mK with calculated $M(B)$ for each model superimposed on top. The designations Gaussian 0 and Gaussian 0.5 refer to the Gaussian model for the DOS with B^0 and $B^{½}$ dependence of the width Γ respectively. Similarly Lorentzian 0 refers to the Lorentzian model with B^0 dependence of Γ. The fitting parameters can be found in Table 3.3.i, the background DOS was a variable for these fits.

Fig. 3.3.i shows dHvA oscillations (down sweep) at 69 mK with the $M(B)$ oscillations for the different models superimposed on top. The different models produce similar results at higher fields, but the Lorentzian model appears to fit the magnitude of the lower field oscillations best.

The presence of a background density of states in between the Landau levels can be attributed to an inhomogeneity of the carrier number density across the sample. Investigation of the presence of a background density of states between Landau levels for the different models shows that for Gaussian broadening there is a sizable background DOS but only a negligible one for the Lorentzian broadening. Fig. 3.3.ii and Fig. 3.3.iii show dHvA oscillations at 740 mK with the various modelled $M(B)$ for a

varying background DOS and zero background DOS respectively. Oscillations at 740 mK allow a better fit to the modelled DOS, while the magnitude of the dHvA is reduced compared to lower temperatures the induced current features which are more temperature sensitive have mostly disappeared. This allows modelling of dHvA oscillations at higher fields than at low temperatures and hence mechanical noise associated with the magnetometer has less of an effect on the fitting procedure, also the effect of remnant magnetic field on the data as discussed in chapter 2 is reduced. This is illustrated by the reduced errors for the high temperature data shown in Table 3.3.i.

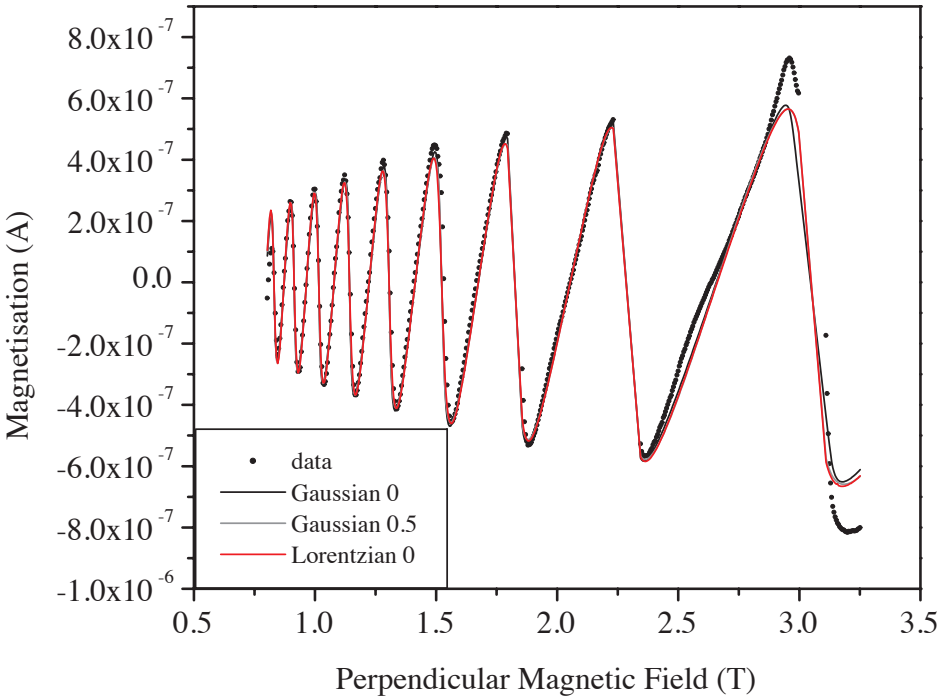

Fig. 3.3.ii plot of dHvA oscillations at 740 mK ± 10 mK. Also plotted are the calculated magnetisation $M(B)$ curves for different models of Landau level broadening where a background density of states was allowed. The values of the fitting parameters for each model can be found in Table 3.3.i.

The variation in the damping of the oscillations towards lower field is most likely due to the changing temperature. This effect has the effect of increasing the errors associated with a fit of the oscillating $M(B)$ The 'hump' on the dHvA oscillation at 3 T could be an indication of an inhomogeneity of the sample number density, however such a feature could also be attributed to magnetic impurities within the rotor or sample or a slow change in the balance point of the rotor.

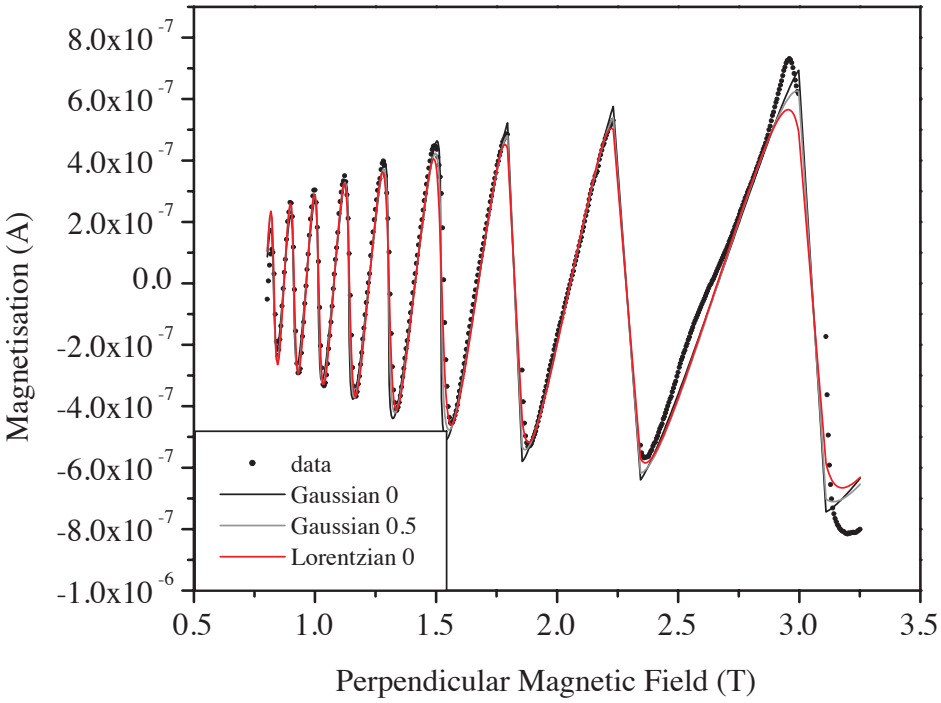

Fig. 3.3.iii plot of dHvA oscillations at 740 mK ± 10 mK. Also plotted are the calculated magnetisation $M(B)$ curves for different models of Landau level broadening. No background density of states was allowed in these fits. The values of the fitting parameters for each model can be found in Table 3.3.i

Figures 3.3.iv and 3.3.v show a close up view of two oscillation troughs shown in figures 3.3.ii and 3.3.iii respectively. With a varying background density of states the Gaussian model with a $B^{½}$ dependence of Γ produces a $M(B)$ curve very similar to the Lorentzian model with the B^0 dependent Γ Gaussian model providing the worst fit.

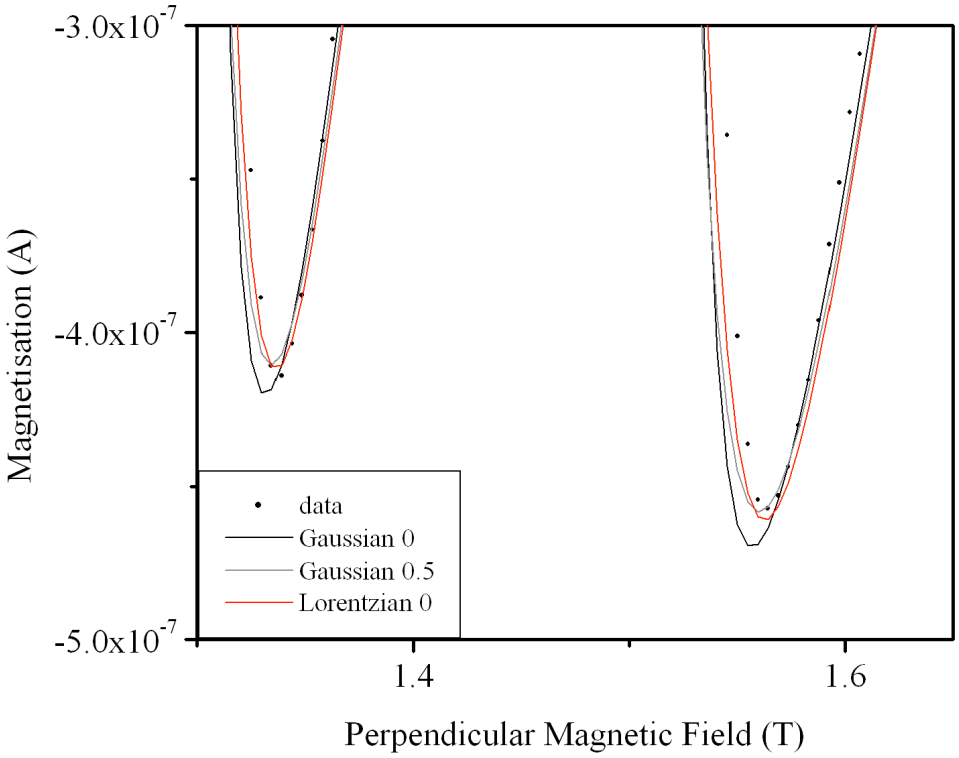

Fig. 3.3.iv close up view of two dHvA troughs from Fig. 3.3.ii with background DOS in model at 740mK.

With the background DOS set to zero the field independent Γ Gaussian model still provides by far the worst fit and the $B^{½}$ dependent Γ Gaussian model shows a significant deviation from the hardly affected Lorentzian model.

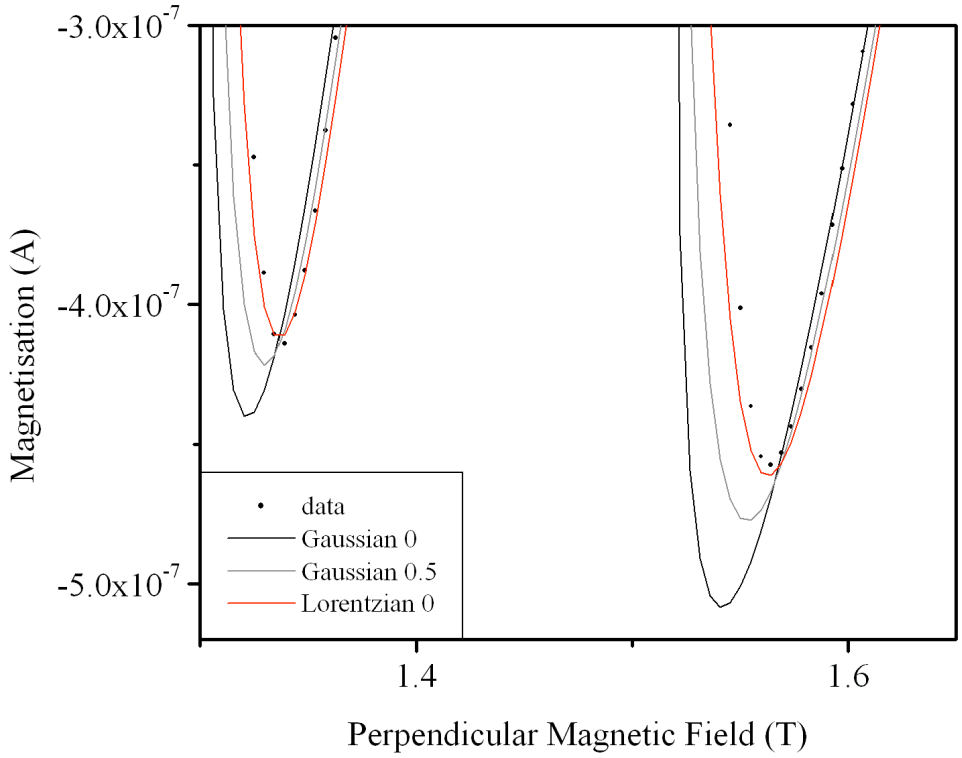

Fig. 3.3.v Close up view of two dHvA troughs from Fig. 3.3.iii with background DOS set to zero at 740mK

The Gaussian models shown in Fig. 3.3.ii have a background DOS of around 20% of the total DOS. This seems a rather high percentage and would indicate large deviations in the number density across the sample from the collective average. In a good quality sample with little inhomogeneity in n_e one would expect the background density of states to be close to zero. In which case the models shown in Fig. 3.3.iii are more accurate, implying that the Lorentzian model for the background density of states is the best model to use to describe the broadening of Landau levels.

For comparison with the higher temperature data shown Fig. 3.3.vi shows dHvA oscillations at 69 mK with the various models plotted on the same axes with zero background DOS. This data is the companion graph to the data shown in Fig. 3.3.i. Similar to the higher temperature data the Lorentzian model DOS follows the magnitude of the dHvA oscillations better than the other two models, especially at lower magnetic fields. The data while at lower temperature also shows oscillations at much lower magnetic field strengths due to induced currents being present and masking the dHvA oscillations at lower filling factors. As such there is increased noise and the

quality of the fit for the modelled DOS is reduced compared to the higher temperature data.

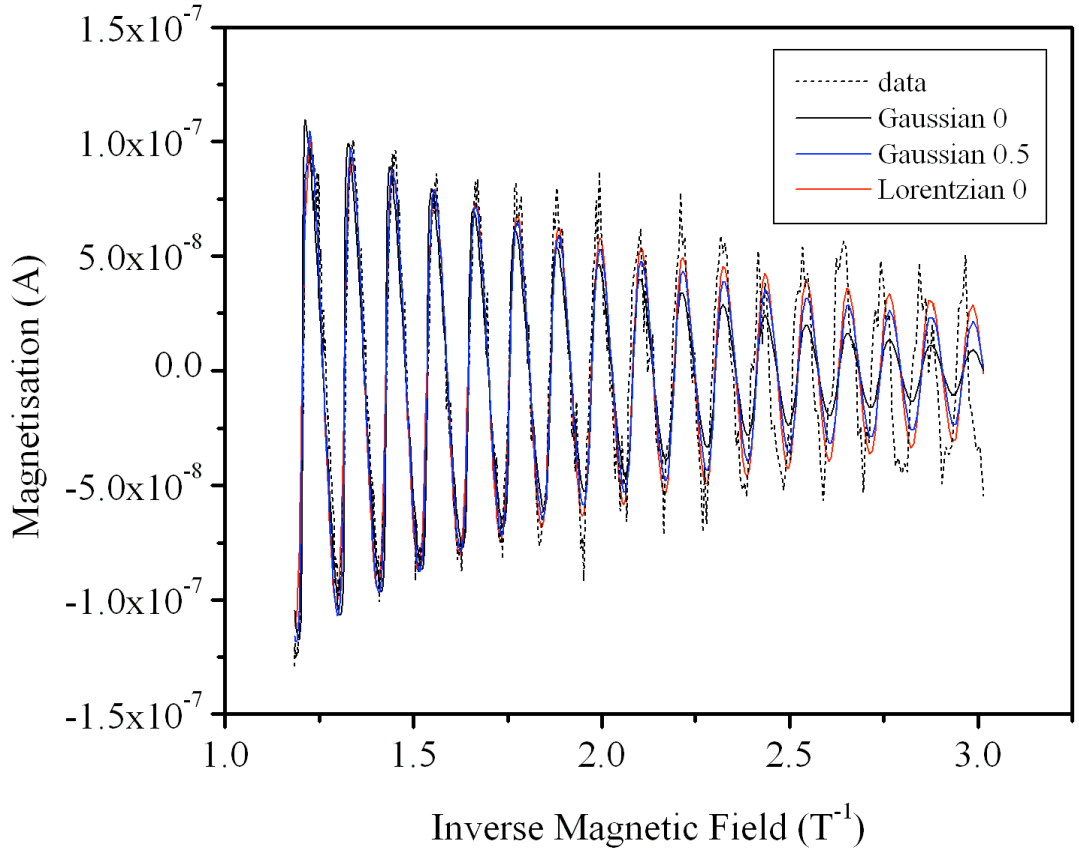

Fig. 3.3.vi Plot of dHvA data at 69 mK ± 10 mK with calculated $M(B)$ for each model superimposed on top. The fitting parameters can be found in Table 3.3.i, the background DOS was set to zero for these fits.

The data shown in Fig. 3.3.i and in Fig. 3.3.vi would at first glance indicate that the Lorentzian model for the DOS is more accurate as it visibly maps the dHvA oscillation peak magnitudes better at lower fields than its counterparts. However the fitting parameters shown in Table 3.3.i indicate that the Gaussian model with the $B^{½}$ dependence of the width Γ produces a better fit to the shape of the dHvA oscillations, both with and without the presence of a background DOS. While the discrepancy between the models is small and could be heavily influenced by noise on the data, this could indicate that there is a transition from a Gaussian DOS with a $B^{½}$ dependent Γ to a more Lorentzian line shape with a field independent Γ as the magnetic field is increased.

740 mK	n_e *10^{15}	Width Γ	Background DOS	Error *10^{-8}
Gaussian	4.40905207	0.333391881	0	2.886904
	4.41946029	0.263195413	0.240297141	2.338416
Gaussian $B^{1/2}$	4.414990167	0.37906	0	2.482787
	4.419278425	0.344497437	0.18777834	2.346826
Lorentzian	4.419748806	0.203144867	0	2.280037
	4.419421163	0.203582538	2.25239E-04	2.280604

69 mK	n_e *10^{15}	Width Γ	Background DOS	Error *10^{-8}
Gaussian	4.409462042	0.220758371	0	3.504938
	4.408926653	0.182816982	0.424939069	3.074309
Gaussian $B^{1/2}$	4.408270436	0.365364727	0	3.108106
	4.408513937	0.363058108	0.102936478	3.106505
Lorentzian	4.411543073	0.189152779	0	3.14799
	4.411557993	0.193247916	0.004139939	3.150609

Table 3.3.i Fitted parameter values for the various models for $M(B)$ oscillations at 740 mK as shown in Fig. 3.3.ii and Fig. 3.3.iii, also $M(B)$ oscillations at 69 mK as shown in Fig. 3.3.i and Fig. 3.3.vi for comparison. The background DOS is given as a proportion of the total DOS. The width Γ is given in meV, the number density is in carriers per m^2. The error is the deviation of the model from the data and gives an indication of the quality of a fit.

Illumination of the sample with a red LED changed the number density of the sample from $\sim 4.40 \times 10^{15}$ /m^2 before illumination to $\sim 6.95 \times 10^{15}$ /m^2. Illumination of the sample also has the curious effect of removing induced current peaks from the data. De Haas – van Alphen oscillations were observed at 40 mK, 114 mK, 306 mK, 391 mK, 540 mK and 700mK. In general Lorentzian model produced the best fits to the data followed by the Gaussian with the $B^{½}$ dependant Γ. The effect of the background DOS was the same pre-illumination data. Fig. 3.3.vi shows a plot of the dHvA oscillations post-illumination with the best fitting Lorentzian model $M(B)$ superimposed on top.

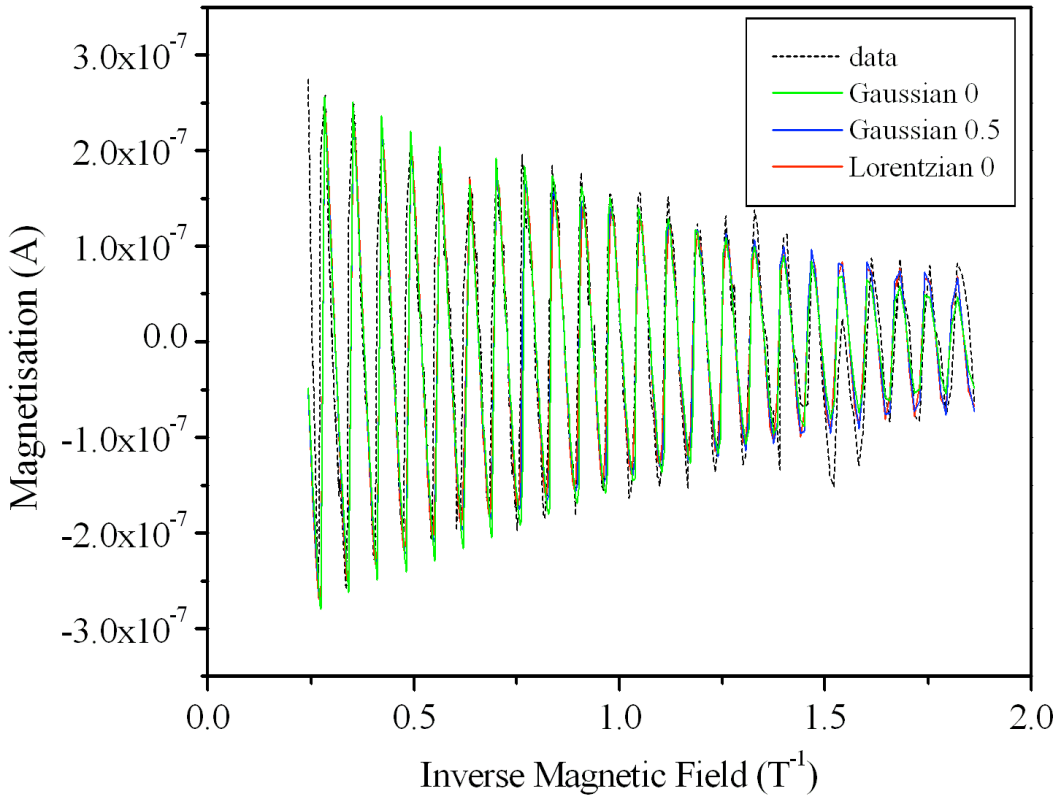

Fig. 3.3.vii Plot of experimental data taken after illumination with a red LED at 306 mK ± 0.5 mK, note the increased oscillation frequency compared to previous plots. $M(B)$ oscillations with a zero background DOS for each model is superimposed on top. The fitting parameters for the different models can be found in Table 3.3.ii.

As with the pre-illumination data the Lorentzian DOS modelled $M(B)$ on average provides the best fit to the dHvA oscillations. Because illumination of the sample removes the effects of induced currents larger field ranges with more oscillations were available for fitting. The 40 mK data set has the largest field range with oscillations extending to lower fields than at higher temperatures. The fitting parameters shown in Table 3.3.ii show that the Gaussian modelled DOS with a $B^{½}$ dependence of Γ provides the best fit to data indicating that again there maybe a transition between a Gaussian DOS line shape and a Lorentzian one. As before a Lorentzian DOS line shape requires a much smaller background DOS to model $M(B)$ oscillations.

40 mK	n_e *10^{15}	Width Γ	Background DOS	Error *10^{-8}
Gaussian	6.820132543	0.205522259	0	4.034515
	6.830907371	0.176811408	0.308614549	3.724989
Gaussian $B^{1/2}$	6.830198193	0.330538573	0	3.672055
	6.830352854	0.324198908	0.061431737	3.676305
Lorentzian	6.832796025	0.143704516	0	3.753036
	6.83279625	0.143704516	0.000652307	3.753459
114 mK	n_e *10^{15}	Width Γ	Background DOS	Error *10^{-8}
Gaussian	6.972050534	0.228108823	0	2.145419
	6.98357556	0.159548402	0.368375331	1.967589
Gaussian $B^{1/2}$	6.976680143	0.325570745	0	2.123786
	6.976680143	0.325570745	9.62E-06	2.123783
Lorentzian	6.980551451	0.140848452	0	2.078063
	6.981952804	0.112612352	0.136443954	2.056714
306 mK	n_e *10^{15}	Width Γ	Background DOS	Error *10^{-8}
Gaussian	6.967995434	0.255198731	0	2.279168
	6.978059759	0.175765105	0.297026407	2.084682
Gaussian $B^{1/2}$	6.971769038	0.327621618	0	2.192649
	6.971769038	0.327621618	7.82E-05	2.192636
Lorentzian	6.97620355	0.143427401	0	2.1012
	6.975809985	0.12561136	0.078303728	2.0893
391 mK	n_e *10^{15}	Width Γ	Background DOS	Error *10^{-8}
Gaussian	6.953618441	0.289371608	0	2.774135
	6.95530391	0.204335952	0.428660836	2.462234
Gaussian $B^{1/2}$	6.95575696	0.384234483	0	2.544537
	6.956133067	0.344204162	0.273221324	2.484278
Lorentzian	6.956683937	0.193645597	0	2.487656
	6.956683937	0.193645597	0.004041139	2.490356
540 mK	n_e *10^{15}	Width Γ	Background DOS	Error *10^{-8}
Gaussian	6.960185571	0.291267644	0	1.579116
	6.970259168	0.191711698	0.314415193	1.415452
Gaussian $B^{1/2}$	6.962422493	0.344706004	0	1.464397
	6.96737656	0.270450027	0.311229998	1.426392
Lorentzian	6.96363909	0.175334667	0	1.408497
	6.965381588	0.133342765	0.134440295	1.393826
700 mK	n_e *10^{15}	Width Γ	Background DOS	Error *10^{-8}
Gaussian	6.961609	0.283189	0	1.932958
	6.972550316	0.213541863	0.271264143	1.729868
Gaussian $B^{1/2}$	6.965378821	0.354642822	0	1.728621
	6.96804133	0.331800488	0.157223108	1.688229
Lorentzian	6.969197644	0.167724224	0	1.652271
	6.969406418	0.165243358	0.009938095	1.653027

Table 3.3.ii Fitted parameter values for the various models for $M(B)$ oscillations at different temperatures after illumination. The background DOS is given as a proportion

of the total DOS. The width Γ is given in meV, the number density is in carriers per m^2. The error is the deviation of the model from the data and gives an indication of the quality of a fit.

3.4 Summary

De Haas - van Alphen oscillations have been measured using sensitive torsion balance magnetometer in a 10× quantum well sample in the range 26 mK to 740 mK. Modelled $M(B)$ oscillations have been fit to the dHvA data to yield information about the shape of the broadening of the density of states and its origins. The best fit of the modelled $M(B)$ to the data was achieved using a Lorentzian model for the broadening of the DOS with a field independent width Γ, both before and after illumination of the sample with an LED to change the carrier number density. A Gaussian model for the DOS with a $B^{½}$ dependence of Γ produced a similar quality of fit. However, for the Gaussian model to achieve results similar to the Lorentzian model approximately 20% to 30% of the DOS had to be located between Landau levels in the form of a constant background DOS. This value seems unusually large compared to results from similar experiments [Potts (1996)], indicating that the Lorentzian model $M(B)$ is a more realistic model for the broadening of the Landau levels. Although the data suggest that there may be a transition from a Gaussian DOS with a $B^{½}$ dependence of Γ to a Lorentzian DOS line shape as the magnetic field is increased. The critical factor here would be the ratio of the magnetic length $l_B = (\hbar/eB)^{½}$ to the range of the disorder causing the scattering events. The Lorentzian model produced very similar results when the background DOS was set to zero to when it was a variable fitting parameter. This is probably due to the shape of the Lorentzian broadening compared to Gaussian broadening, with a Lorentzian model there remains a significant DOS between Landau levels located in the tails. This can produce a similar result to a large background DOS although the origins a different.

The width Γ of the Landau levels was found to be reasonably constant with increasing temperature as expected as the modelled DOS takes into account thermal effects. Landau level broadening is most likely caused by scattering from remote ionised donors present in the sample due to the modulation doping. However the indication that the DOS has a Gaussian line shape with a $B^{½}$ dependence of Γ at higher Landau levels indicates that there are also some short range scattering events that contribute to the

Landau level broadening. Illumination of the sample also had no affect on the values of Γ only on the number density n_e. The magnitude of the background DOS in the different models was invariant to increasing temperature confirming that any background DOS is due to electron scattering by disorder and inhomogeneities in the number density across the sample rather than phonon scattering.

4 Observation of the Decay of Long Lived induced currents in 2D electron systems

4.1 Introduction

As discussed in chapter 1, the quantum Hall effect [von. Klitzing (1980)] is characterised by almost dissipationless electrical conduction ($\rho_{xx} \approx 0$) and quantised Hall resistance ($\rho_{xy} = h/ie^2$, where i is an integer). The small value of ρ_{xx} makes measurements of the resistance using Hall bar techniques difficult since the resolution is defined by the sensitivity of the voltmeter used, and increasing the current through the sample results in breakdown of the QHE and destruction of the quasi-dissipationless state [Ebert (1983) and Matthews (2000)].

Previous experiments by Eisenstein [1985] have shown that large circulating currents are induced as a time varying magnetic field is swept through the QHE condition of integer Landau-level filling factor (ν). So far it still remains uncertain where such induced currents flow within the 2DES, however the currents are thought to flow along the inner border between the outermost compressible strip at the edge of the 2DES, and the incompressible region within [Chklovskii (1992)]. The currents are therefore isolated from any ohmic contacts at the edge of the 2DES, for which there is good experimental evidence [Ahlswede (2002)]. Consequently the induced currents are not detected in conventional transport measurements, despite being typically at least an order of magnitude larger than the injected currents involved in such experiments [Ahlswede (2002), Huels (2004)]. The lack of detection of induced currents using alloyed contacts can be attributed to the formation of a, depletion region along the border between the 2DES and the metallic ohmic contact at high magnetic fields decoupling the bulk region of the 2DES from the alloyed contact preventing the circulating currents from entering the alloyed contacts, thus preventing their detection. Induced circulating currents were first observed by Eisenstein [1985] using a torsion-balance magnetometer to detect the magnetic moment associated with the circulating current. Other methods for detecting these circulating currents include using single-electron transistors fabricated on top of the 2DES to detect the circulating electrons *via* the Coulomb-blockade potential [Ahlswede (2002), Klaffs (2004)]. Also it has recently been shown that laterally defined

nanostructures such as quantum point contacts and quantum dots are sensitive to the presence of the induced circulating current [Pioro-Ladriere (2006)].

It is possible however to build up a microscopic picture of the processes, which may be taking place within the 2DES. From the finite value of ρ_{xx}, a manifestation of electron scattering events can be caused by many different mechanisms, including impurities and disorder in the crystal lattice, electron – phonon scattering and electron – electron scattering events. The decay of these induced circulating currents observed in a static magnetic field gives an insight into both the breakdown of the QHE at large currents [Ebert (1983)], and the processes by which the QHE system can relax to thermodynamical equilibrium [Jones (1995, 1996)].

Torque magnetometry investigations [Jones (1995, 1996)] carried out at Exeter into the nature of the decay of these induced circulating currents by measuring the decay of the associated magnetic moment. The measurements indicated that the current would decay exponentially to zero over a period of about 4 hours. The data showed two distinct decay regimes. A fast exponential decay in the first few tens of seconds was attributed to the breakdown of the quantum Hall regime at high currents. This was followed by a much slower exponential decay, which was observed over a time period of ~800s. A single exponential fitted to the decay in the quasi-dissipationless quantum Hall regime indicated a single dominant relaxation mechanism. Their measurements yielded a value for ρ_{xx} on the order of $10^{-14}\Omega/\square$ for $\nu = 1$ and 2 at 40mK. Due to improvements in the experimental setup since these experiments (see chapter 2), the decays can now be observed for days rather than minutes. The aim of the experiments described in this chapter is to obtain a more accurate value of ρ_{xx} and the methods of relaxation that allow the system to return to equilibrium. The observations and results discussed in this chapter expand upon those previously published [Kershaw (2007)].

These more recent experiments, carried out on two GaAs/AlGaAs heterojunctions over a much longer time period, have indicated the presence of a power-law type decay of the induced circulating currents in the quasi-dissipationless quantum Hall regime, indicating the presence of multiple co-dominant relaxation paths, and consequently a resistivity that decreases monotonically with time.

4.2 Experimental Details

Torsion – balance magnetometry experiments (as explained in chapter 2) were carried out on two high-mobility modulation doped heterojunctions.

Sample V0049: $n_e = 1.7\times10^{15}$ m^{-2}, $\mu = 200$ m^2 (Vs)$^{-1}$
Sample T73: $n_e = 4.4\times10^{15}$ m^{-2}, $\mu = 50$ m^2 (Vs)$^{-1}$

Sample V0049 is a modulation doped single GaAs/AlGaAs heterojunction, where as Sample T73 is delta doped. The samples are uncontacted 10×6 mm rectangles, the mass of the sample on the magnetometer rotor was balanced using an undoped insulating piece of GaAs of equivalent size and mass. The experiments in this chapter are mainly concerned with sample T73.

Experiments were performed at magnetic fields up to 12 T and temperatures in the range 20 to 800 mK. The dilution refrigerator was run in single-shot mode during decay measurements to eliminate mechanical noise, which would otherwise have occurred as the sorption pumps were cycled. The decays were monitored for up to 40 hours, the length of the decay measurements is limited by the temperature and magnetic field stability of the system (see chapter 2). During single shot operation the sorption pumps are not regenerated and the temperature of the experiment is controlled by heater located at the top of the mixing chamber. A consequence of using this method is that during long experiments the sorption pumps can empty the still. Without any returning liquid from a regenerating sorption pump to refill the still the cooling power is decreased due to the reduced surface area and the temperature of the mixing chamber starts to increase. A similar effect can occur if the sorption pumps become saturated with gas, however this usually occurs long after the still has been emptied of liquid. As result of the temperature instability which is typically no more than 10 mK is noted at the end of each decay measurement.

4.2.1 Data preparation

Induced currents were observed at Landau level filling factors $\nu = 1$ to 4 for sample V0049 and $\nu = 2$ to 4, 6 and 8 for sample T73; Fig. 4.2.1.i shows typical raw data.

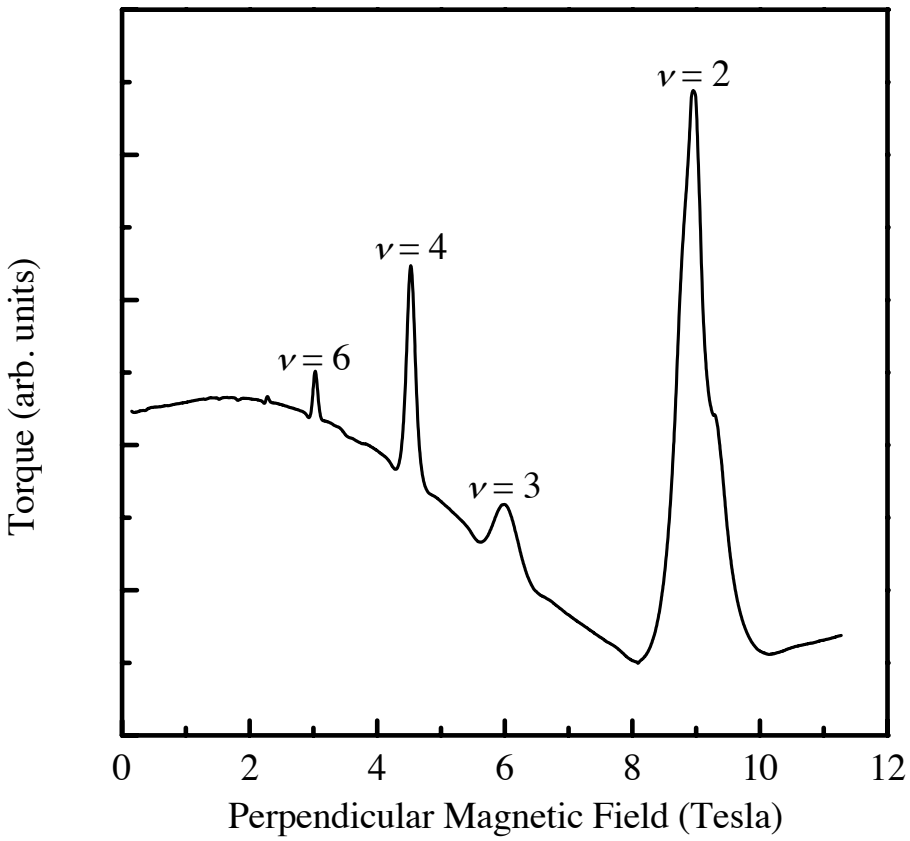

Fig. 4.2.i Magnetometer output for sample T73 at 20 mK, the magnetic field was swept from 0 to 12 T at a rate of 30 mT s^{-1}.

In order to determine a rate of decay of the induced current, the initial magnitude of the current needs to be known. For this reason it is necessary to be able to remove any background magnetisation signal that is not due to the induced current. The background signal arises from the presence of magnetic impurities in the magnetometer rotor and torsion fibre and possibly from the sample itself. Removal of this signal is necessary in order to calculate a decay rate since the zero value needs to be known. The non-equilibrium nature of the induced currents means that the direction of current flow and hence the polarity of the associated magnetic moment is dependent upon the direction of sweeping magnetic field. A value for the background signal at a given point on an eddy current peak can be obtained by sweeping the magnetic field through an integer value of ν and then back again. By displaying the data from both sweep directions on the same plot it is easy to see where the induced current peak begins since the induced current peak changes polarity with field sweep direction but the background signal remains constant (as shown in Fig. 4.2.ii). By masking off the entire induced current

peak a curve can be fitted to the background signal surrounding the induced current features. A low order polynomial usually provides an adequate fit to the background magnetisation signal allowing removal of the background.

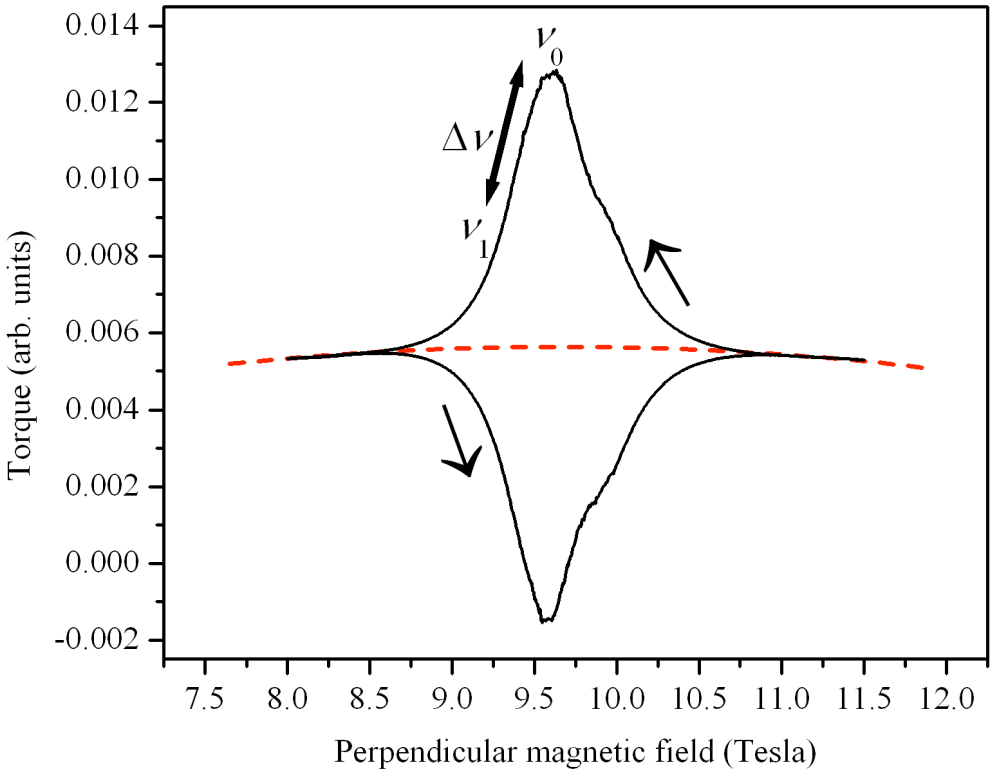

Fig. 4.2.ii Plot of measured torque vs. magnetic field around $\nu = 2$ for both increasing and decreasing magnetic field showing the change in polarity of the eddy current and example values for the parameters ν_1, $\Delta\nu$ and ν_0. Also shown is a 2nd order polynomial fit to the background signal. The arrows show the direction of the sweeping magnetic field.

Fig. 4.2.iii shows both polarities of eddy current with the polynomial fit to the background signal removed. The zero value in this graph now corresponds to zero magnetic moment and hence zero circulating induced current. The circulating currents were induced by sweeping the magnetic field from a filling factor $\nu_1 = \nu_0 + \Delta\nu$ to the filling factor ν_0 at which the decay was to be measured (as shown in Fig. 4.2.ii), at a rate dB/dt. Hereafter $\Delta\nu$ will be referred to as the "approach distance" and dB/dt as the "approach rate". As discussed later the magnitude of the induced current and its rate of decay are dependent on the approach rate and the distance of approach.

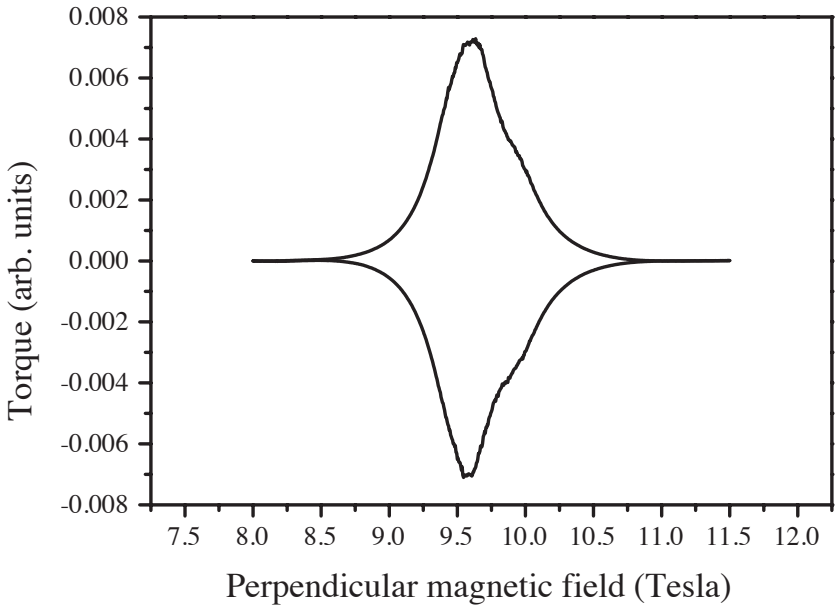

Fig. 4.2.iii Plot of measured torque vs. magnetic field around $\nu = 2$ for both increasing and decreasing magnetic field showing the change in polarity of the eddy current after subtraction of the polynomial background signal.

Prior to each eddy current decay measurement the magnetic field is swept from a value ν_0 + X to a value ν_0 – X and back again with X chosen so as to sweep through the entire eddy current peak. The field is then swept to the value ν_1 in preparation to begin the eddy decay measurement. This allows determination of the background signal at the start of the experiment as described previously. After the decay measurement is complete the field is swept back to a value ν_0 + X to check for any variation in the background signal due to drift in temperature or due to the electronic equipment. The polynomial fit to the background signal can be used to determine the value of the background at the point ν_0. This value is then subtracted from the decay data before any determination of the decay rate is made.

Having subtracted any background signal from the decay data, the data need to be converted to current versus time so that the decay can be evaluated. Chapter 2 explained how a calibration could be obtained for the sensitivity of the experiment. This calibration is used to convert the output of the lockin amplifier in volts to torque in Nm. The torque data that are displayed in the previous graphs can be converted to magnetic moment m using $\tau = mB\sin 20^\circ$ (20° being the angle of the normal to the 2D plane with

respect to the applied magnetic field). Magnetic moment can be converted to current using $m = IA$. Where A is the surface area of the 2DES.

4.3 Results

4.3.1 Different Decay Regimes

The data shown in Fig. 4.3.i show the decay of an induced current at $\nu = 2$ for sample V0049. As can be seen from the data there are two distinct decay regimes. The initial decay, which is exponential in nature, causes the current to fall to approximately 70% of its original value in the first 100 seconds. This is followed by a much slower decay, in which the current only decays a further 25% in the next 12 hours. The inset of Fig. 4.3.i shows a logarithmic plot of the same data; the slower decay regime appears to have a linear dependence when displayed on a logarithmic plot, implying a power-law dependence. On the logarithmic plot the initial exponential decay regime is signified by a deviation from the linear trend. The data shows that after 100 seconds the exponential decay has become sufficiently small so as to be masked by the power-law decay.

The initial exponential decay implies that for the first 100 seconds there is a single dominant decay mechanism, where as the presence of the power-law dependent decay for the following 12 hours indicates the presence of several decay mechanisms, or equivalently decay with a varying time constant.

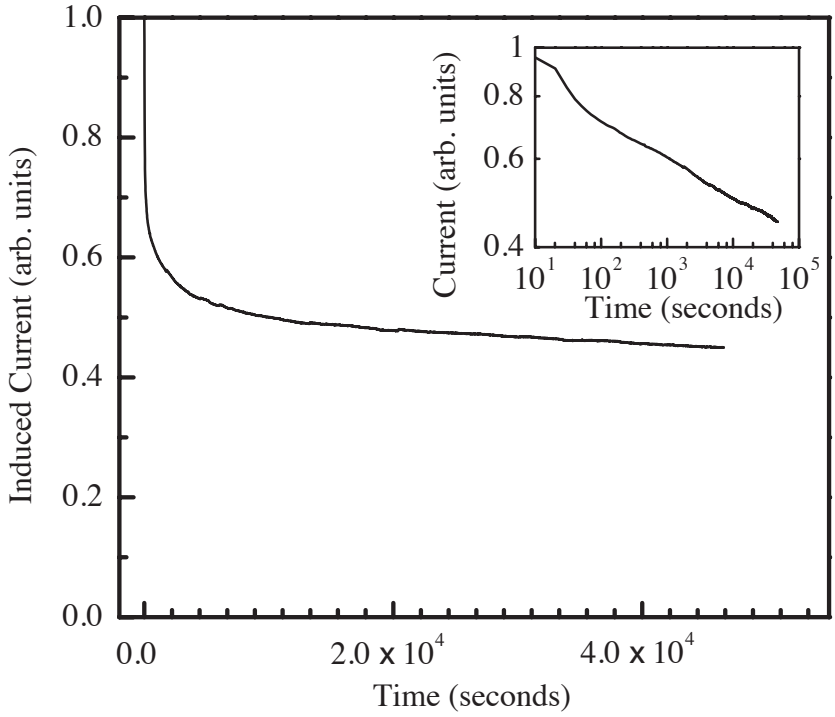

Fig. 4.3.i Decay of an induced current at $\nu = 2$ for sample V0049 (T = 88 ± 2 mK); inset, a logarithmic plot of the same data.

Having established that there are two distinct decay regimes, the difficulty lies in obtaining quantitative information about each regime without being influenced by the other. This can be done by separating the initial exponential decay from the subsequent power-law. To do this, we use the assumption that the exponential component of the decay will be negligible after ~500 seconds of decay. The raw data from $t \geq 500$ s onwards is then fitted to a power-law $I = at^n$. To obtain the initial fast decay we simply subtract the power-law fit to the decay obtained from the entire data set. The initial decay is then fitted to an exponential of the form $I = I_0 \exp(-\lambda_{\text{init}} t)$ where λ_{init} is the decay rate.

4.3.2 The power-law decay

As mentioned in the previous section the current decay after $t = 100$ s has a power-law nature. Fig. 4.3.ii below shows the decay of the induced current at $\nu = 2$ at 88 mK for sample V0049. A power-law of the form $I = at^n$ has been fit to the data $t \geq 500$ s is also shown in the figure, the exponent n of the power-law has a value of ~ –0.07. As shown

in the figure the current has only decayed to approximately half of its initial value over the first 12 hours of the decay and the rate is slowing.

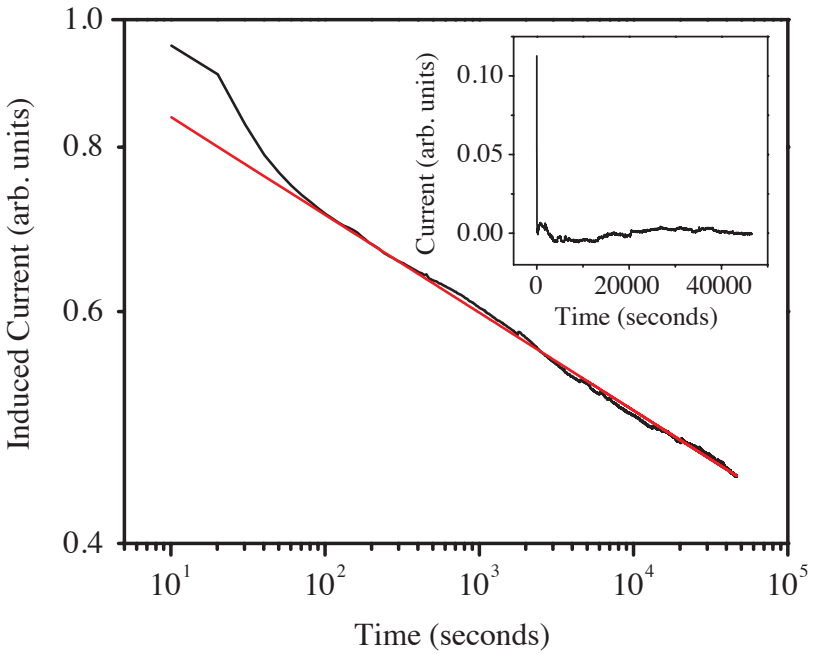

Fig. 4.3.ii Logarithmic plot of the data shown in Fig. 4.3.i and a power-law fit to the decay the power-law has an exponent $n = -0.0742 \pm 0.0002$; inset, a plot of the data with the power-law fit deducted from the data, showing the remaining initial decay.

It was observed that the rate of decay for induced currents varies depending upon the Landau level-filling factor ν. Induced currents at $\nu = 4$ were observed to decay much faster than their equivalents at $\nu = 2$ for a given ΔB, dB/dt and temperature (as shown in Fig. 4.3.iii). This implies that the separation $\hbar\omega_c$ between Landau levels affects the decay rate of the induced current, an indication that inter–Landau level scattering is taking place.

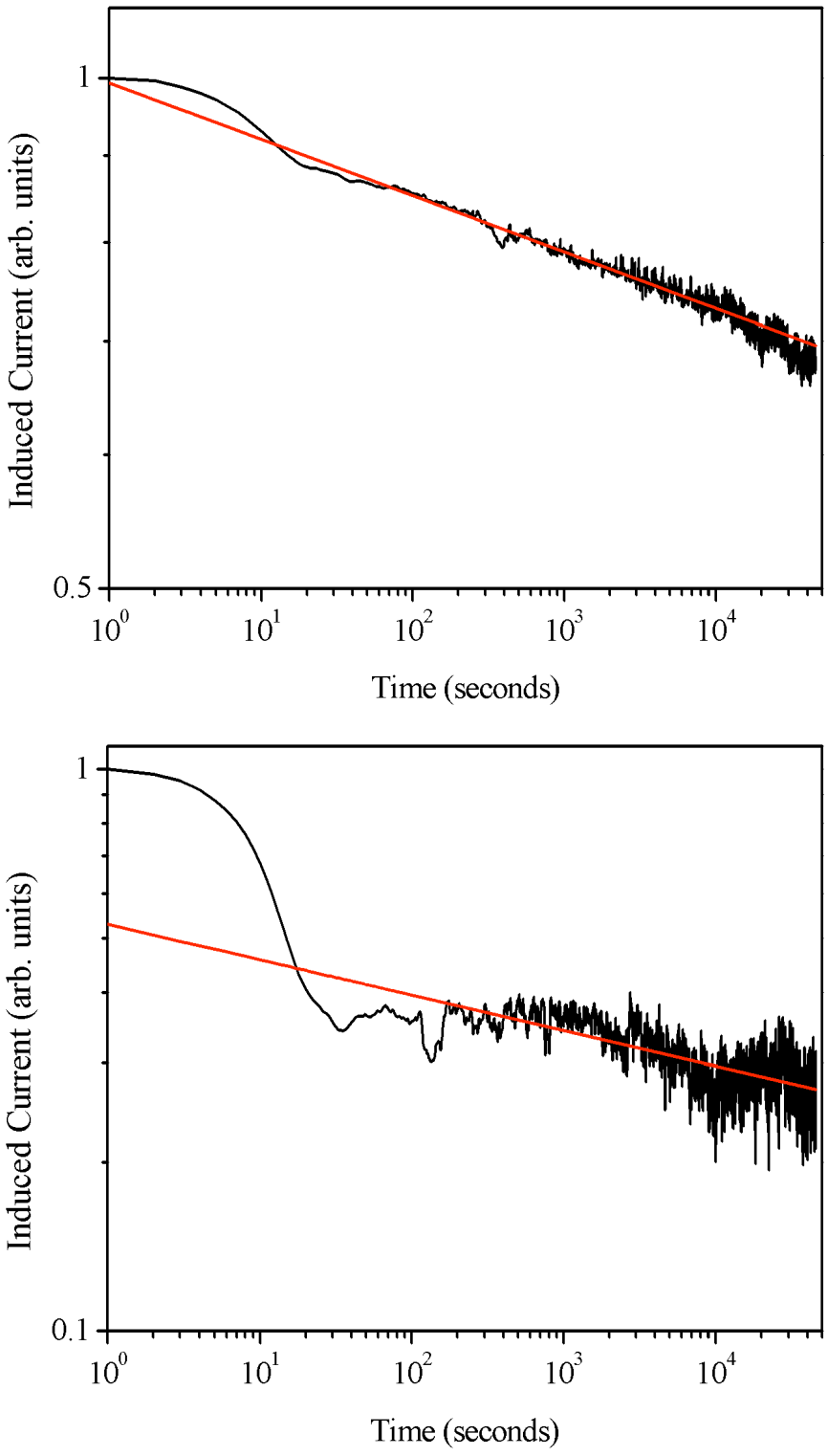

Fig. 4.3.iii Logarithmic plots of the decay of induced currents at filling factors $\nu = 2$ (top) and $\nu = 4$ (bottom) for sample T73 at 70 ± 10 mK ($\Delta B = 0.058$ T, $dB/dt \approx 0.8$ mT s^{-1}). The increased noise present on the $\nu = 4$ decay is a result of the smaller magnitude of the induced current and hence the signal to noise ratio is smaller. Power-law lines of best fit are also shown, for $\nu = 2$, $n = -0.02359 \pm 0.00007$ and for $\nu = 4$, $n = -0.07535 \pm 0.0007$.

4.3.3 The exponential decay

Fig. 4.3.iv shows the first 120 seconds of the data presented in the inset of Fig. 4.3.ii on a semi-logarithmic plot. It can be seen that after the power-law fit to the slow decay has been removed the remaining initial decay has an exponential nature with a time constant $1/\lambda_{init} = 32 \pm 4$ s. This relatively fast exponential decay is linked to the high-current breakdown of the QHE [Jones (1996)] and is only present when the circulating current is greater than the critical current required for QHE breakdown. The single exponential decay implies that there is only one relaxation mechanism associated with this decay.

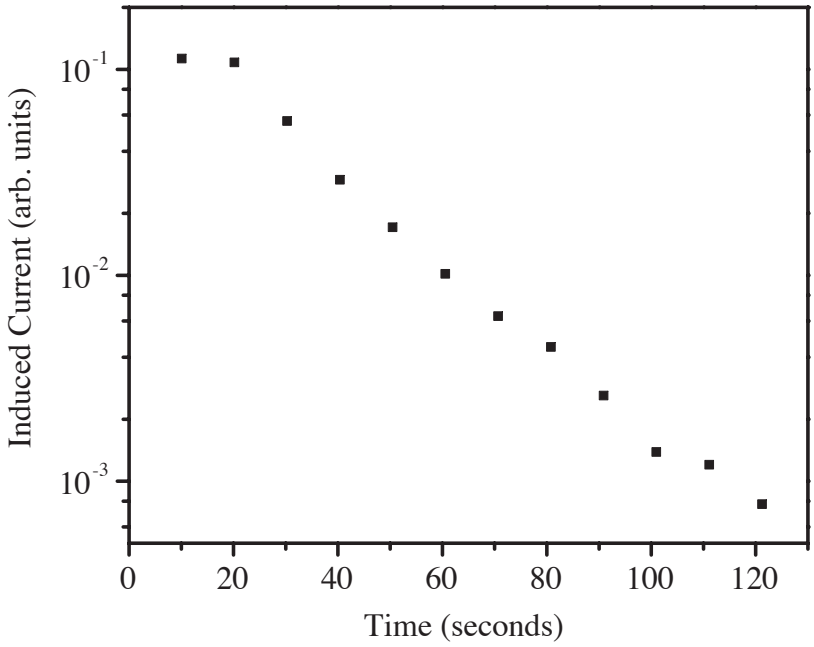

Fig. 4.3.iv Semi-log plot of the first 120 seconds of the data shown in the inset of Fig.4.3.iii showing the exponential nature of the initial decay.

The time constant and the magnitude of the single-exponential decay both depend on the approach rate dB/dt and the approach distance ΔB, since the high current breakdown of the QHE is dependent on the magnitude of the induced current. Before the approach begins, there will already be an induced current present, having been induced by the sweep to the starting point $B = B_0 + \Delta B$. In the experiment of Fig. 4.3.ii, this pre-existing induced current was of opposite polarity to the current induced by the approach to B_0. Consequently, a judicious choice of ΔB and dB/dt should enable one to completely eliminate the initial exponential decay. In contrast, the slow power-law

decay is not affected by the choices of ΔB and dB/dt. The magnitude of the induced current increases with dB/dt and ΔB up to the value at which high-current breakdown of the QHE occurs but cannot increase any further [Matthews (2000)]. As ΔB or dB/dt are increased further, the initial fast decay appears and becomes gradually more pronounced, while at the same time the exponential time constant $1/\lambda_{init}$ decreases. This is consistent with the system being driven progressively deeper into the QHE breakdown regime (Fig. 4.3.v). The saturation magnetisation is an upper limit to the magnitude of the induced magnetic moment and hence an upper limit to the magnitude of the induced current governed by the breakdown of the QHE.

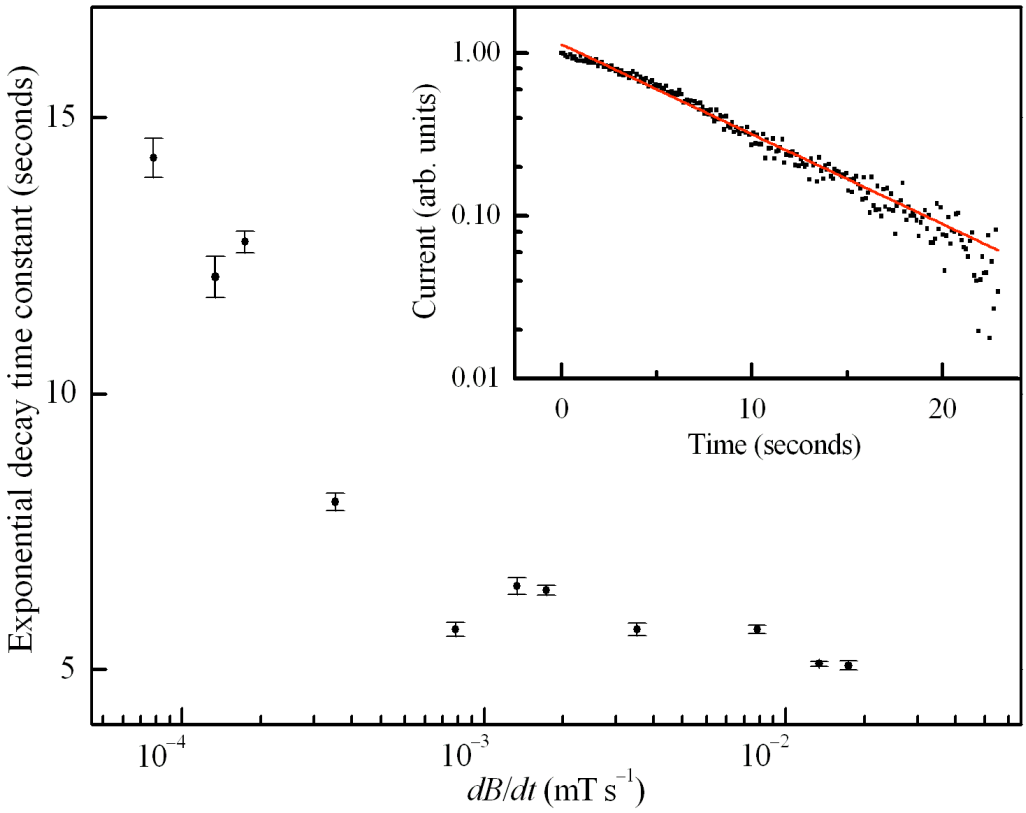

Fig. 4.3.v Exponential decay time constant versus approach rate dB/dt for sample T73 shown on a reverse semi-logarithmic plot for clarity ($\nu = 2$ at 150 ± 2 mK $\Delta B = 0.1$ T). The error bars represent the uncertainty associated with the exponential fit. Inset is a semi-logarithmic plot of a typical initial exponential decay with background signal and slow power-law decay removed for sample T73 ($\nu = 2$ at 300 mK $\Delta B = 0.058$ T, $dB/dt \approx 0.8$ mTs^{-1}). The decay has a time constant of $1/\lambda_{init} = 7.87 \pm 0.08$ s. The initial deviation from the exponential fit is a feature associated with the large inductance of the superconducting magnet.

4.3.4 Filling factor dependence

It is observed that as ν_0 moves away from integer values the magnitude of the initial induced current is reduced. This can easily be seen in Fig. 4.2.i since the measured torque is proportional to induced current. As one would expect decreasing the magnitude of the induced current has an effect on the initial exponential decay. As can be seen in Fig. 4.3.vi as ν_0 moves away from an integer value the magnitude of the initial exponential decay decreases and by $\nu = 2.15$ the initial exponential decay is no longer present.

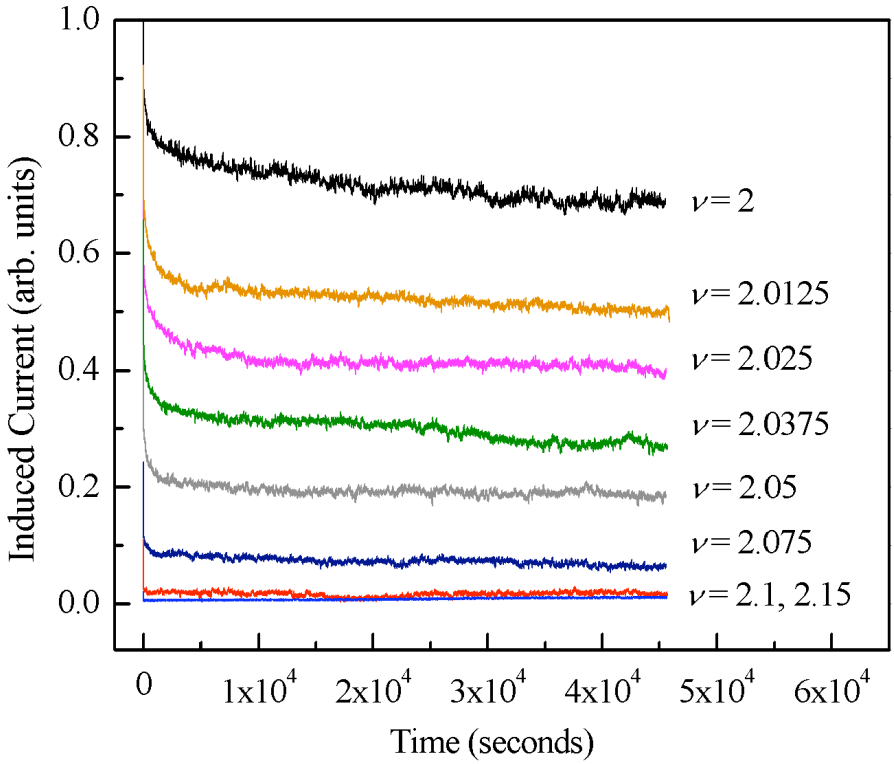

Fig. 4.3.vi Plot of induced current versus time for decays in the range $\nu_0 = 2$ to $\nu_0 = 2.15$ for sample T73 at 150 ± 8 mK, $\Delta B = 0.058$ T, $dB/dT \approx 0.8$ mTs^{-1}. The initial current decreases as ν_0 moves away from integer value. The decays are *not* offset.

The power-law exponent of the slow decay becomes more negative as ν moves away from its integer value, resulting in a more rapid decay (Fig. 4.3.vii). This contrasts with the initial exponential decay, which becomes slower away from integer ν due to the smaller induced current and the fact that the QHE is not driven so far into the high-current breakdown regime.

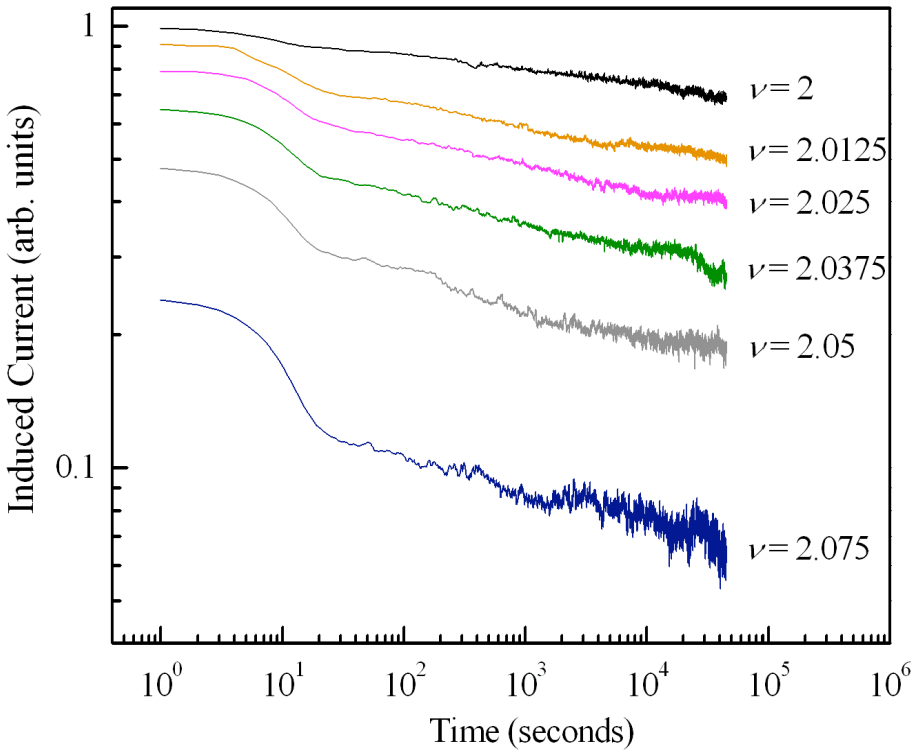

Fig. 4.3.vii Logarithmic plot of induced current versus time for decays in the range $\nu_0 = 2$ to $\nu_0 = 2.15$ for sample T73 at 150 ± 8 mK, $\Delta B = 0.058$ T, $dB/dT \approx 0.8$ mTs^{-1}. The decays are *not* offset. Decays at $\nu = 2.1$ and 2.15 have been omitted for clarity.

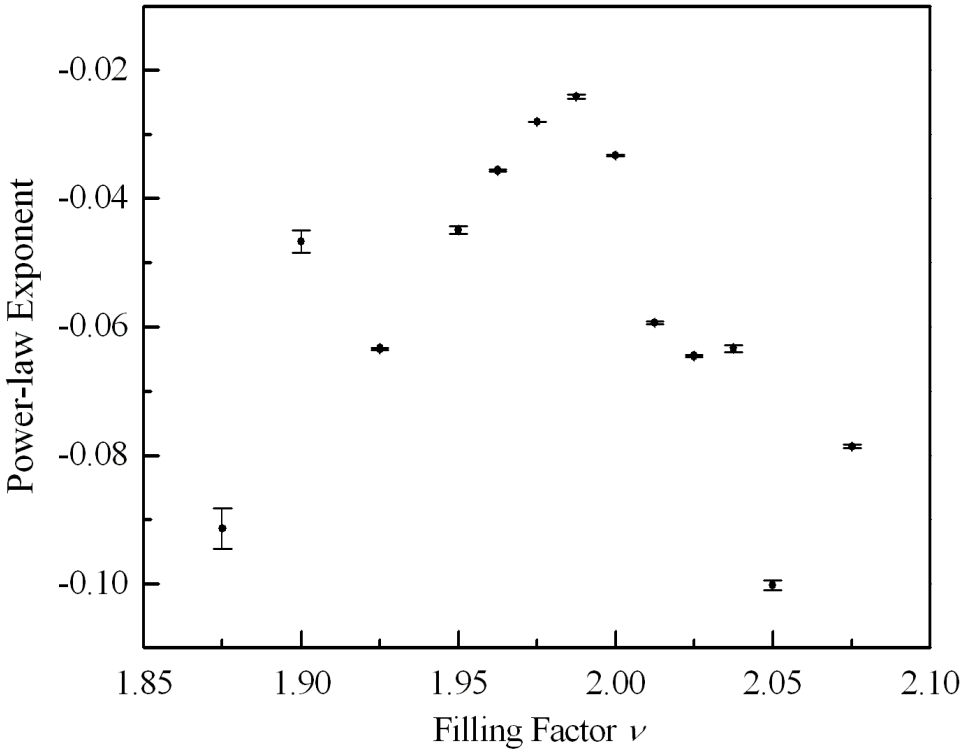

Fig. 4.3.viii Plot of slow decay power-law exponent n versus filling factor ν for sample T73 at 150 ± 8 mK, $\Delta B = 0.058$ T, $dB/dT \approx 0.8$ mTs^{-1}. The discrepancy with the peak not aligning with $\nu = 2$ is probably due to an error in the value of the number density.

Points outside the range $1.875 \geq \nu \leq 2.075$ have been excluded because as ν moves away from integer filling factor the induced current becomes smaller and closer to the noise level.

4.3.5 Temperature dependence

As one would expect the decay of the induced circulating currents is dependent on the temperature of the system. However the extent of the temperature dependence is surprising since at low temperatures < 1K there are few phonons present in the system. Instead the temperature dependence probably arises as a result of electrons in states above E_F leading to increased inter and intra–Landau level scattering. It was observed that both the magnitude of the induced current and the rate of decay are dependent on the temperature.

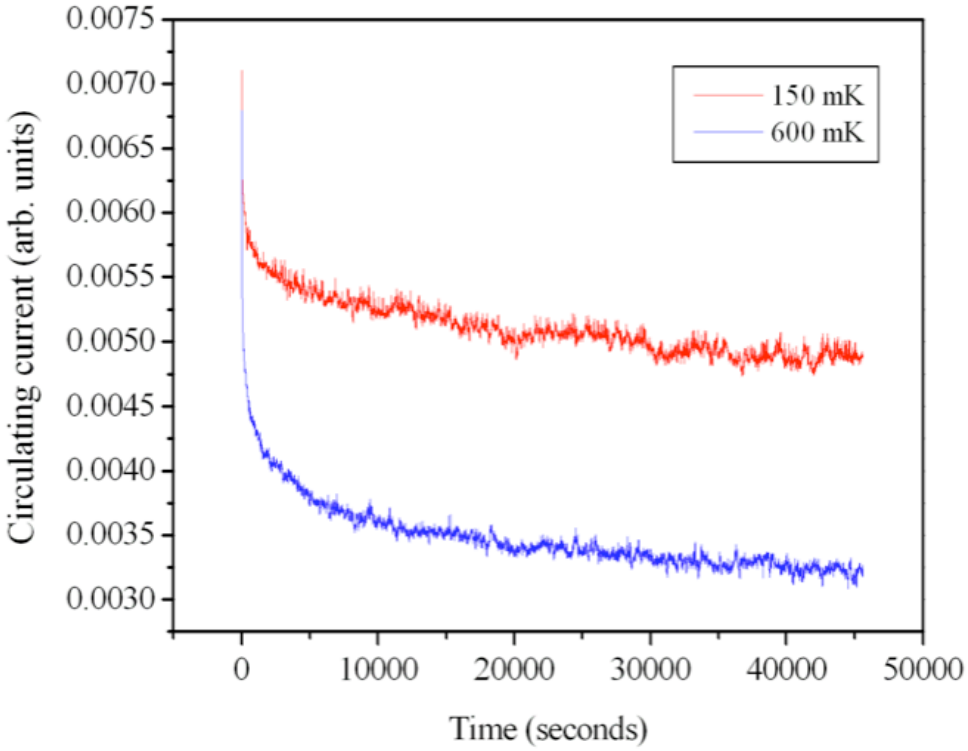

Fig. 4.3.ix Plot of current decay data for an induced current in sample T73 at $\nu = 2$ for the temperatures 150 ± 2 mK and 600 ± 2 mK on the same scale ($\Delta B = 0.058$ T, $dB/dt \approx 0.8$ mT s^{-1}).

Fig 4.3.ix above shows two traces of the current decay at 150 mK and 600 mK, note the difference in the magnitude of the initial current and the increased rate of the power law decay. The variation in magnitude of the initial induced current suggests that the initial

resistivity of the sample increases with temperature also. Further experiments showed that the initial current appears to have a linear dependence on the temperature.

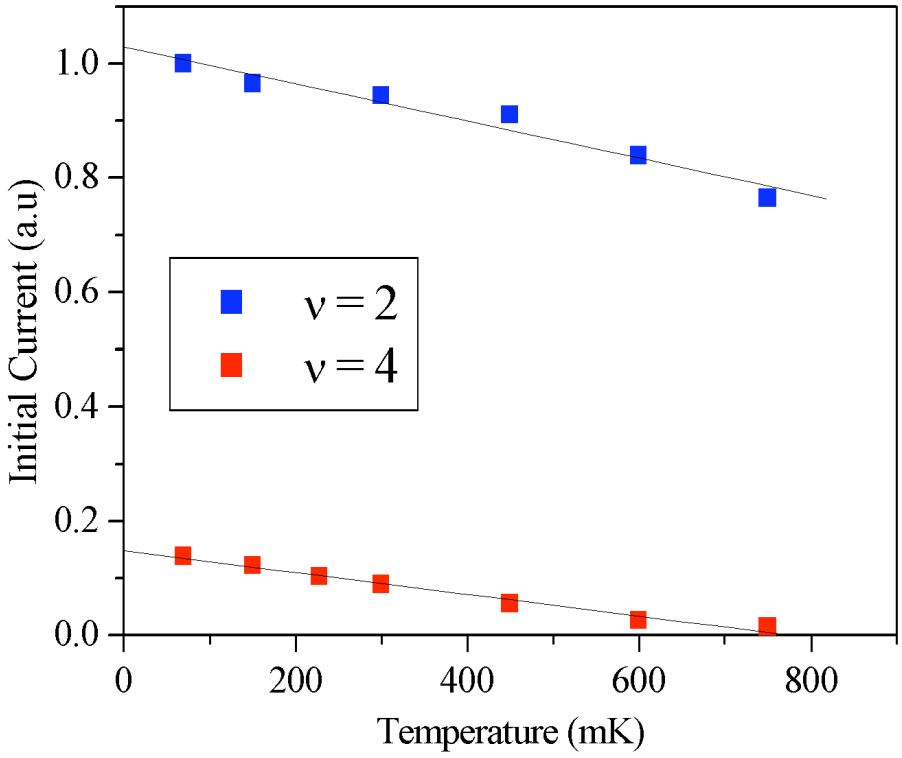

Fig. 4.3.x Plot of the magnitude of the initial current for $\nu = 2$ and $\nu = 4$ in the range 70 mK $\rightarrow$ 750 mK for sample T73 showing the approximately linear dependence (ΔB = 0.058 T, $dB/dt \approx 0.8$ mT s^{-1}).

Fig. 4.3.x shows the linear dependence of the magnitude initial current for induced currents at $\nu = 2$ and $\nu = 4$. Note how the initial current for $\nu = 4$ has fallen to almost zero by 750 mK illustrating the small temperature range these measurements can be performed over. Figures 4.3.xi and 4.3.xii show the decay of induced currents for filling factors $\nu = 2$ and $\nu = 4$. Deviations in the power-law trend of the decays such as the displayed in the 750mK decay of Fig. 4.3.xi is a result of the magnetic field instability discussed in chapter 2.

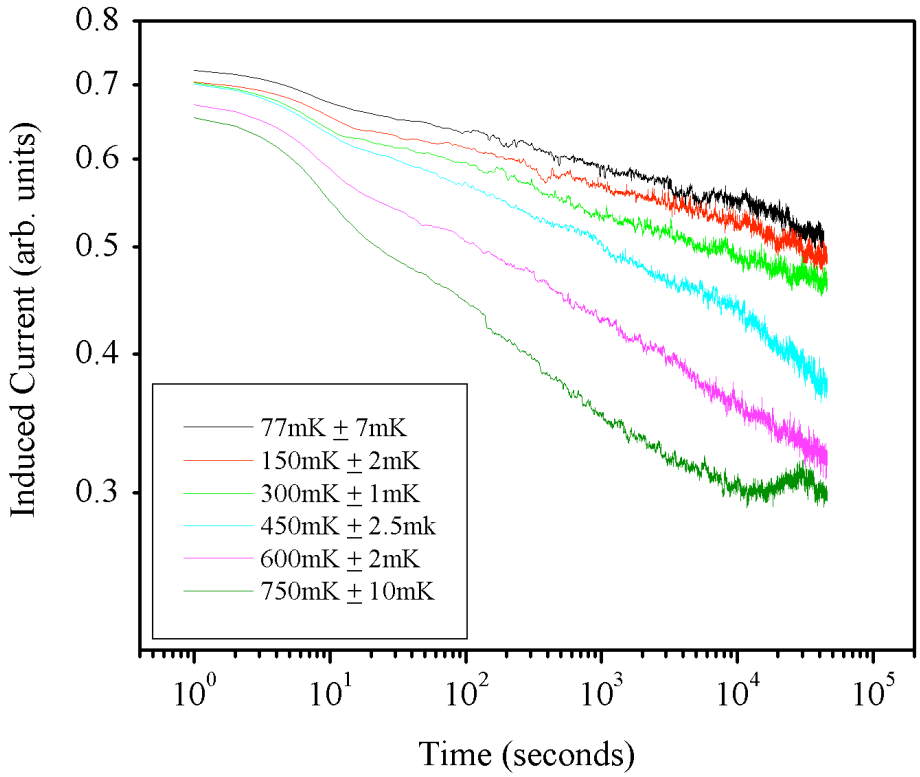

Fig. 4.3.xi Logarithmic plot of the induced current in sample T73 at $\nu = 2$ in the temperature range 70 mK → 750 mK (ΔB = 0.058 T, $dB/dt \approx 0.8$ mT s^{-1}). The deviation from the power-law in some decays is most likely due to the magnet stability issues discussed in chapter 2.

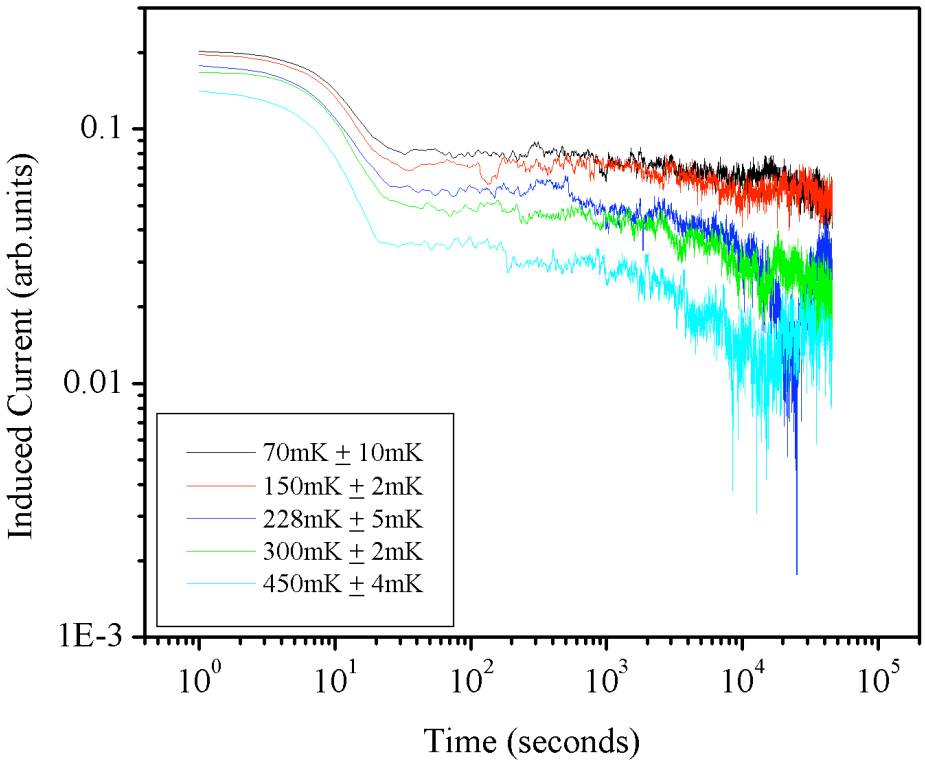

Fig. 4.3.xii Logarithmic plot of the induced current in sample T73 at $\nu = 4$ in the temperature range 70 mK → 450 mK ($\Delta B = 0.058$ T, $dB/dt \approx 0.8$ mT s^{-1}). Higher temperature decays have been omitted for clarity. The curvature on the higher temperature decays could be an indication that there are fewer decay mechanisms and hence the decay becomes more exponential. The apparent increase in induced current in some decays is due to the magnet stability issues discussed in chapter 2.

By fitting a power-law type curve to the decay data the exponent n of the decay can be obtained. The temperature dependence of the power-law decay exponent for sample T73 at $\nu = 2$ and $\nu = 4$ in the range 70 mK to 750 mK are shown in Fig. 4.3.xiii. The data display a linear dependence, with the exponent becoming more negative with temperature signifying a faster decay. The decay of currents at $\nu = 4$ has a temperature dependence ~3 times faster than at $\nu = 2$.

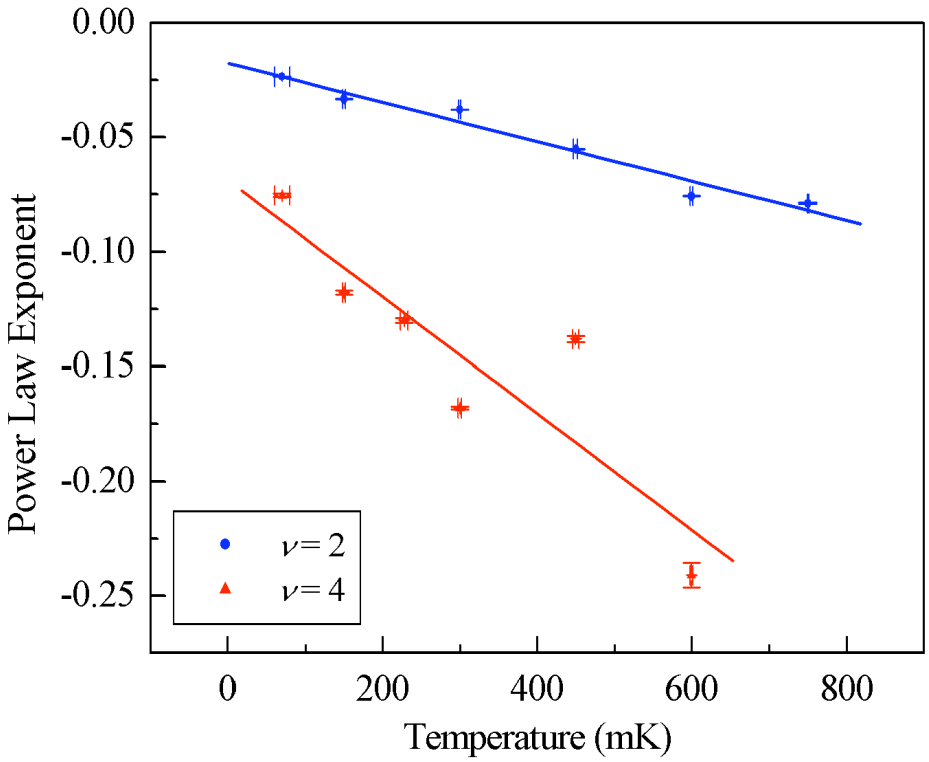

Fig. 4.3.xiii Temperature dependence of the slow decay power-law exponent for sample T73 at $\nu = 2$ and $\nu = 4$ ($\Delta B = 0.058$ T, $dB/dt \approx 0.8$ mT s^{-1}). Error bars for the deviation of the temperature and uncertainty in the power-law fit are also shown.

4.4 Discussion

4.4.1 Calculating the resistivity

As was shown in the previous sections of this chapter the magnitude of the induced current and the rate of decay is dependent upon the Landau level-filling factor ν and temperature. Both of these factors affect the scattering rate of the electrons as they circulate within the sample, and thus the rate of decay.

In a sweeping magnetic field charge displacement caused by the circulating induced current results in a Hall voltage between the edges and the centre of the 2DES. For a non-ideal sample ρ_{xx} and σ_{xx} are non-zero allowing the charge circulating at the edge to return to the centre of the 2DES. An estimate of ρ_{xx} can be derived from the classical Drude scattering expression [Jones (1995)]:

eqn. 4.4.i $$\rho_{xx} = \rho_{xy} / \omega_c \tau .$$

Jones (1995) showed that the majority of the energy stored in the sample is stored capacitively in the Hall electric field between the circulating current at the edge of the sample and the centre of the 2DES. A scattering event as a result of the non-zero values of ρ_{xx} and σ_{xx} will cause an electron to move radially and so discharge the capacitor, resulting in a reduction in the tangential induced current.

The power-law decay can be pictured in two ways. The current may be thought of as flowing in a single loop close to the edge of the sample. In this picture the power-law form of decay in the quasi-dissipationless QHE regime, indicates the presence of multiple relaxation paths (i.e. multiple independent scattering events each with its own characteristic time scale), which contribute to ρ_{xx}. Relaxation will occur near to impurities or sample edges where the Hall field becomes concentrated and exceeds its critical value. As the decay progresses, and both the current and the Hall electric field decrease, the faster relaxation routes become progressively blocked, leaving only the slower ones remaining. In the second equivalent picture, one could envisage a disordered sample as containing many current loops of different shapes and sizes confined to wells within the disorder potential. In such a system each current loop has a characteristic time constant defined by the capacitance of the loop (determined by the size of the loop) and the local resistivity. The variation in decay rate between current loops would then explain the overall power-law decay rate observed. Faster decaying current loops will disappear first until a single current loop remains.

In both of these pictures, one would expect the power-law dependence to give way to a single exponential decay after a very long decay time. However there is no indication of this behaviour in our data after 45000 seconds of decay. In a previous study into the 'noisy' breakdown of the QHE [Elliott (2006)], statistical analysis of the breakdown events displayed a power-law dependence, suggesting multiple paths for breakdown to occur. It is interesting that we can now infer the same about the decay of circulating currents in the quasi-dissipationless QHE regime.

The power-law form of the relaxation can also be interpreted as a time varying ρ_{xx}. We can describe the power-law decay, $I = at^n$, as an exponential decay with a time-varying decay rate, $I = I_0\exp(-\lambda(t)t)$. In this case,

eqn. 4.4.ii $$\lambda(t) = -\frac{n}{t}\left(\ln(t)\right).$$

In this description, the decay rate $\lambda(t)$ is proportional to ρ_{xx}. This implies that ρ_{xx} decreases with time according to:

eqn. 4.4.iii $$\rho_{xx} = -\frac{hm^*}{\upsilon e^3 B}\left(\frac{n}{t}\ln(t)\right).$$

For the decay in sample T73, ($\nu = 2$, 150 mK, the top trace of Fig. 4.3.vi), this equation yields a value of $\rho_{xx} = 8.36\times10^{-13}$ Ω/□ at $t = 100$ s falling to $\rho_{xx} = 4.32\times10^{-15}$ Ω/□ after 45000 s. These values are consistent with those stated by Jones (1995), in which a single exponential was fitted to data taken over a period of 800 seconds. The values presented here are lower due to the increased time scales over which the measurements were performed. The striking new feature of our current studies is that the decays are found to be sub-exponential, resulting in a ρ_{xx} that decreases with time (approximately as $1/t$). This new behaviour has become apparent because we have been able to follow the decays for ~60 times longer than in previous experiments.

4.4.2 Scattering Mechanisms

The filling factor dependence shown in Fig. 4.3.viii indicates that the system is becoming more dissipative as the filling factor deviates from integer values of ν. This demonstrates that ρ_{xx} and σ_{xx} are not perfectly quantised and do not remain constant across the whole of the Hall plateau.

Heinonen (1984) showed that there was a dramatic onset of dissipation in the QHE regime as the speed of the carriers approached the speed of sound in the semiconductor. They showed that at the onset of dissipation the Hall voltage V_H was such that the energy eV_H is larger than the cyclotron energy $\hbar\omega_c$. Thus given a mechanism for electrons to make the transition between Landau levels, electrons would be able to move to states of lower energy. For this to be possible there has to be a source of momentum for the electron to make the transition in k-space. A suitable source of momentum change could come from scattering by impurities or phonons.

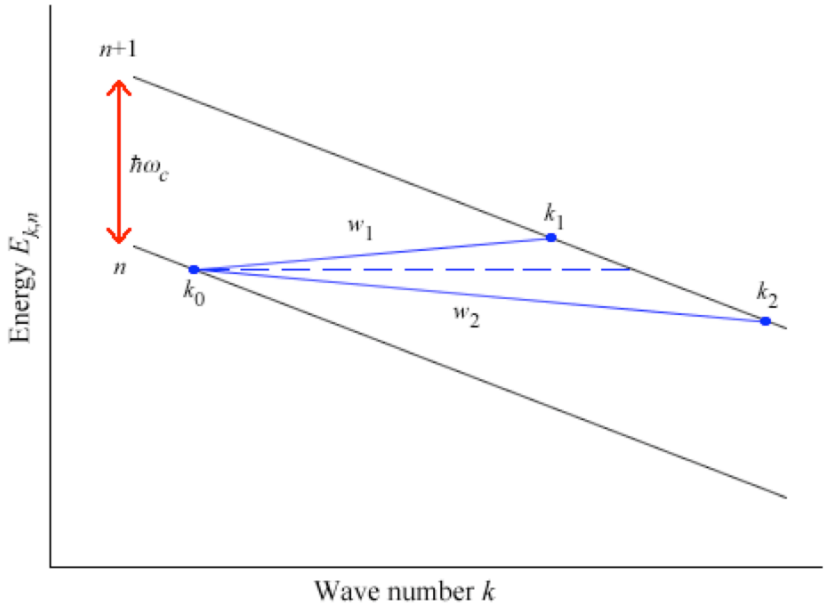

Fig. 4.4.i Diagram showing two Landau levels n and n+1 of an electron system in crossed electric and magnetic fields. An electron can make the transition from k_0 to k_1 (k_2) by adsorption (emission) of a phonon with transition rate w_1 (w_2).

It was shown that at the critical current required for breakdown, the drift velocity $v_d \equiv Ec/B$ (where E is the Hall field) of the carriers is close to the speed of sound v_s, which in GaAs is ~2470ms^{-1}. Usually associated with particle physics 'Cerenkov' radiation is the spontaneous emission of a photon as the speed of a charged particle exceeds the speed of light in a medium, it has been suggested by Streda (1984) that an analogous process of spontaneous phonon emission occurs when an electron exceeds the speed of sound in that medium. The data suggest that this form of 'Cerenkov' radiation is an important source of phonons in the system and hence a source of momentum scattering. For phonon assisted inter–Landau level scattering to occur there has to be available states in the n+1 Landau level, hence this process can only occur when the Fermi energy E_F lies between the Landau levels n and n+1, the slope of the Landau levels is given by $\hbar v_d = \hbar Ec/B$ [Heinonen (1984)]. 'Cerenkov' radiation however may not be the only source of phonons in the system. Since the samples under study are GaAs, which is a piezoelectric material, phonons can be produced as a result of the Hall voltage across the sample. This piezoelectric phonon emission and the absorption of the phonon by a subsequent electron facilitate the transitions shown above in Fig 4.4.i.

Fig. 4.3.vi shows that the exponential decay is present even at $\nu = 2.15$, which lies in the tail of the induced current. At $\nu = 2.15$ the current decays exponentially to zero in a few tens of seconds and there is very little power-law decay. This can be attributed to intra-Landau level scattering [Streda (1984)] becoming the dominant relaxation mechanism away from integer ν [Heinonen (1984)]. For intra–Landau level transitions to be possible there has to be empty states in the n^{th} Landau level. Intra–Landau level scattering can only occur after inter–Landau level scattering has emptied electron states in the n^{th} Landau level or the filling factor is no longer an integer, which is the case here. If the filling factor is non-integer then phonons produced by 'Cerenkov' radiation or piezoelectric emission are free to scatter electrons into an empty state within the same Landau level. These scattering events cause dissipation of the circulating current and a reduction of the Hall voltage across the sample. The processes by which the QHE system returns to its dissipationless state are still unclear at this time.

Thermally activated phonons are generally ignored at temperatures below 1K, hence the temperature dependence of the power-law decay shown in Fig. 4.3.xiii must be due to other processes. The Fermi function $f(E,\mu) = (1+\exp((E - E_F)/k_BT)^{-1}$ (where μ is the chemical potential) gives the probability of a given electron energy state is available at a certain temperature. As the temperature is increased it becomes more likely that electrons will occupy states above the Fermi energy. For a magnetic field corresponding to an integer filling factor ν, E_F lies halfway between Landau levels. Therefore as the temperature is increased an electron can be scattered from a state below E_F towards the centre of the sample into another Landau level. This process of thermally activated inter–Landau level scattering leaves vacant electron states within a Landau level below E_F allowing intra–Landau level scattering to take place from the extended states close to integer ν into the localised states in the 'tails' of the Landau level close to E_F. We have also observed that the current at the start of the power-law decay I_{t_0} (shown in Fig. 4.3.x), which is equivalent to the critical current required for QHE breakdown [Matthews (2004)] has a linear temperature dependence as previously reported [Pioro–Ladriere (2006)]. This implies a linear dependence of the initial resistivity of the sample on temperature.

Finally we note that a similar power-law form of decay is observed in the relaxation of magnetic moments in Ising spin glasses [Chaubet (1998)]. In the spin-glass phase a simple power-law decay is observed with a temperature-dependent exponent, while

above the spin-glass transition a decay of the form $q(t) = ct^{-x}\exp\left(-\omega t^{-\beta}\right)$ with temperature-dependent exponents $x(T)$ and $\beta(T)$ is observed. If such different phases exist in our experiment, improvements would have to be made to the temperature, mechanical and magnetic field stability to distinguish between these different dependences. The comparison is intriguing nonetheless.

4.5 Summary

With the series of experiments associated with this chapter, we have shown that the decay of induced currents in the quantum Hall regime within a 2DES comprises of an initial exponential decay followed by a much slower power-law decay. The exponential decay can be attributed to the breakdown of the QHE at high currents. Once the current has fallen the quasi-dissipationless QHE state is restored and the current decay then follows a power-law form of decay. The power-law decay suggests the presence of multiple relaxation paths, each with its own characteristic time. The power-law form of decay also implies a ρ_{xx} which is approximately proportional to t^{-1} with calculated values decreasing by two orders of magnitude over the course of 12 hours. This has the important implication that significant residual induced currents will be present for much longer than has previously been thought.

5 Investigation in to the 2D properties of bulk graphite and the presence of Dirac fermions

5.1 Introduction

As shown in chapters 1 and 3 the dHvA effect can be used to characterise properties of an electron system, such as the thermodynamic density of states, carrier number density, effective mass and information about the Landau levels can all be obtained via contactless magnetometry experiments without much perturbation to the system. As also discussed in chapter 1 graphite is a semi-metal made up of Bernal-stacked individual graphitic layers or graphenes. Since the fabrication of individual graphene layers [Novoselov (2004)] the experimental interest in graphene has increased tremendously. Graphene was researched theoretically several decades ago [Slonczewski (1958)] as a theoretical 'building block' to model graphite and later carbon nanotubes and fullerenes. However recent experiments on graphene [Novoselov (2005)] have shown that graphene exhibits an anomalous quantum Hall effect with plateaus at half-integer filling factor and massless, 'relativistic' Dirac fermions. It is these interesting and useful properties that we hope to show exist within bulk graphite, which being easier to fabricate on a large scale would be more useful to industry.

For graphite to exhibit the same properties as graphene each individual graphitic layer would have to be independent of the others with no interaction between them. This is obviously not the case as the graphitic layers in bulk graphite are held together by van der waals forces. However, because the interlayer distance is much larger than the in plane carbon-carbon bond length, the electronic interaction between the planes is much smaller than the in-plane effects. This is manifested in the ratio of the basal to *c*-axis resistivities, which reaches values greater than 10^4 at room temperature in clean samples [Kopelevich (2007)], in contrast to lower quality samples such as Kish graphite where the ratio may only be a factor of 100 or less. Interlayer hopping as a result of disorder in the crystal structure or the presence of impurities is the cause for this increased interaction between the layers and the reduced ratio of resistivities. These large factors in the ratio of resistivities in high quality samples are the reasons for the 2D-like properties of the QHE and the dHvA effect observed in graphite. As shown in chapter 1 plateau-like steps in the Hall resistance R_{xy} have been observed in high quality

HOPG samples [Luk'yanchuk (2006)] but are absent for lower quality samples. This gives the indication that high quality HOPG samples are more 2D-like than their lower quality counterparts such as Kish graphite.

The work of Luk'yanchuk and Kopelevich [2004, 2006] has illustrated the 2D-like properties of HOPG graphite samples and has claimed to have observed the presence of Dirac holes with Berry phase π through use of phase analysis of the dHvA oscillations and band-pass filtering of QHE transport data. However due to the resolution of the SQUID magnetometer used for these experiments and the relatively high temperatures (~2 Kelvin) only a few high-field oscillations were analysed. In this chapter I report on the results of magnetometry and transport experiments on a high quality HOPG sample carried out using a high sensitivity torsion-balance magnetometer (as detailed in chapter 2) at different temperatures with the aim of confirming or refuting the claims of Dirac fermions in graphite and to study the 2D-like nature of graphite in further detail with the aid of more sensitive measurements at lower temperatures.

5.2 Experimental Details

The sample used for both sets of experiments was a piece of ZYB grade HOPG graphite measuring 10 mm × 5.5 mm × 0.5 mm with a mass of 35 mg. For the purpose of the magnetometry experiments the rotor was balanced with an undoped insulating piece of GaAs semiconductor of equivalent mass. Measurements were carried out at temperatures in the range 30 mK to ~4 K in the mixing chamber of a low-vibration dilution refrigerator as described in chapter 2. The angle dependence of the dHvA oscillations is also briefly investigated with oscillations observed at angles of 20° and 2° between the *c*-axis (perpendicular to the basal planes) and the magnetic field.

Standard low frequency ac transport measurements of the QHE were carried out on the same sample after all magnetometry experiments were completed. The transport experiments were carried out at an angle of 20° to the magnetic field for comparison with the dHvA data.

Due to the magnet stability issues discussed in chapter 2 the experimental data displayed in this chapter were taken with the magnet sweeping from high to low fields. This allows a simple subtraction of a constant remnant field to correct the $1/B$

periodicity of the quantum oscillations. Subtraction of a remnant field of 26 mT was found to restore the periodicity of the dHvA oscillations. While the remnant field is small and has little effect on the analysis of high-field oscillations, reliable analysis of low-field oscillations is not possible without this correction as the dHvA peak separation approaches the value of the remnant field.

5.3 Initial Data

Initial magnetometry experiments carried out on the sample with the magnetic field applied at an angle of 20˚ to the *c*-axis showed many dHvA oscillations on a large background magnetisation signal. The size of the background magnetisation caused a deflection of the rotor at high fields sufficient to cause the capacitor plates to touch. This meant for further experiments the sensitivity of the experiment had to be reduced so that both high and low magnetic field oscillations could be observed.

At low fields the background magnetisation signal was approximately linear. Fig. 5.3.i shows the low field oscillations after subtraction of a linear background signal. The data show high frequency oscillations corresponding to either majority holes situated at the *K* point in the Brillouin zone (Fig. 1.7.iii) or majority electrons located near the *H* point according to the SWMC model. The low frequency oscillations superimposed on the majority carrier oscillations could be due to the presence of minority carriers situated at the *H* point in the Brillouin zone (Fig. 1.7.iii and Fig. 1.7.v). The presence of majority and minority carrier oscillations in high quality HOPG samples is an indication of a 3D Brillouin zone rather than a 2D one. At the lowest temperatures available to us the majority hole dHvA oscillations are still present at magnetic fields below 100 mT.

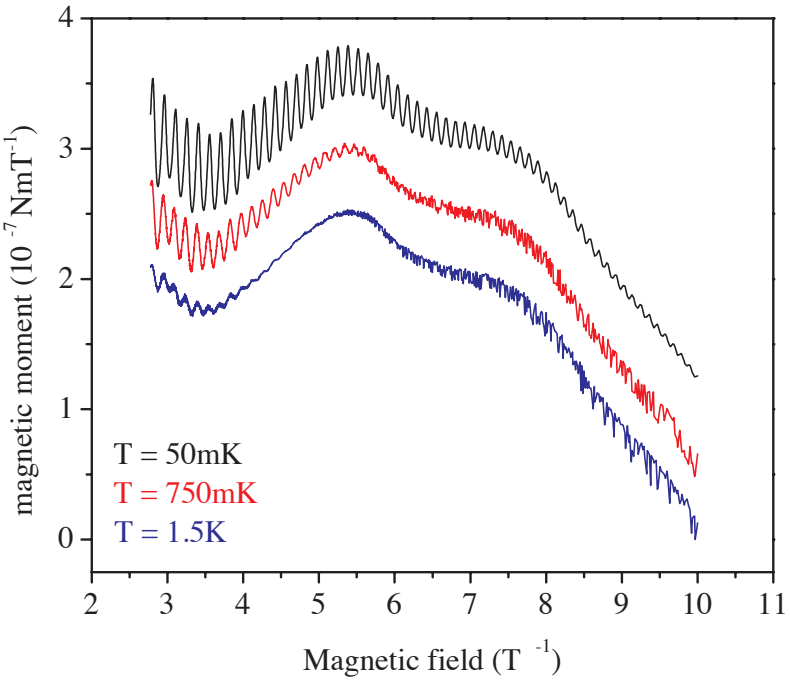

Fig. 5.3.i Plot of preliminary data after subtraction of a linear background showing low field oscillations at 50 mK, 750 mK and 1.5 K. The magnetic field was applied at an angle of 20° to the *c*-axis, the oscillations have been offset for clarity. The increased noise is due either to the heater switching on and off or due to the reduced stabilising effect of a smaller magnetic moment.

5.4 Main results

Further magnetometry experiments on the same graphite sample, using a thicker torsion fibre to compensate for the large background magnetisation signal of the graphite allowed the observation of dHvA oscillations up to 5 T. Fig. 5.4.i shows dHvA oscillations in graphite at 30 mK. The enlarged section of Fig. 5.4.i shows that oscillations are still visible down to magnetic fields of ~100 mT despite the decreased sensitivity of the experiment.

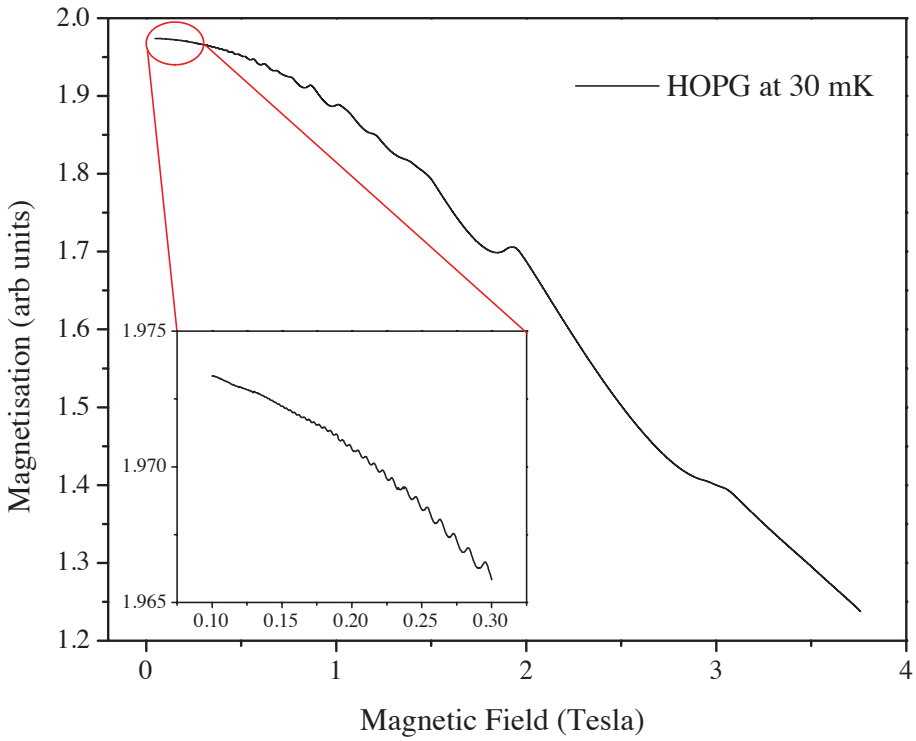

Fig. 5.4.i Plot of magnetisation against magnetic field component parallel to the *c*-axis for dHvA oscillations at 30 mK ± 0.5 mK showing high and low field oscillations (inset). The oscillations continue to ~100 mT. The magnetic field was applied at an angle of 20˚ to the *c*-axis.

Luk'yanchuk [2004] observed two distinct majority carrier frequencies in the dHvA oscillations. This is consistent with the work of Williamson [1965] who also observed two sets of majority carriers and also minority carriers in pyrolytic and single crystal graphite. Using the SWMC model developed by Slonczewski and Weiss [1958] and refined by McClure [1957], Williamson was able to identify the two majority carriers. The SWMC model yields a Fermi surface similar to the one shown in Fig. 1.7.iv with hole oscillations arising from the extremal orbit at the *K* point and electron oscillations from the extremal orbits close to the *H* point. As shown in Fig. 1.7.iv, for a magnetic field applied in the *z*-direction (along the *c*-axis) the extremal hole cyclotron orbit is larger than the equivalent electron orbit. This larger orbit as discussed in chapter 1 implies a larger period between consecutive cyclotron orbits and therefore a higher dHvA frequency.

By interpolating the data in inverse magnetic field and performing a fast Fourier transform (FFT) the oscillation frequencies can easily be found. A FFT performed on the data shown in Fig. 5.4.i over the range 0.25 T to 3.75 T produces two majority carrier oscillation frequencies at 4.30 T^{-1} and 5.95 T^{-1} shown in Fig. 5.4.ii (peaks e1 and h1 respectively). In a 2D picture these frequencies can be thought of as being equivalent to a fundamental field at which all carriers are in the last Landau level. For electrons with a period of 4.30 T^{-1} all carriers will lie within the last Landau level at fields above 4.30 T.

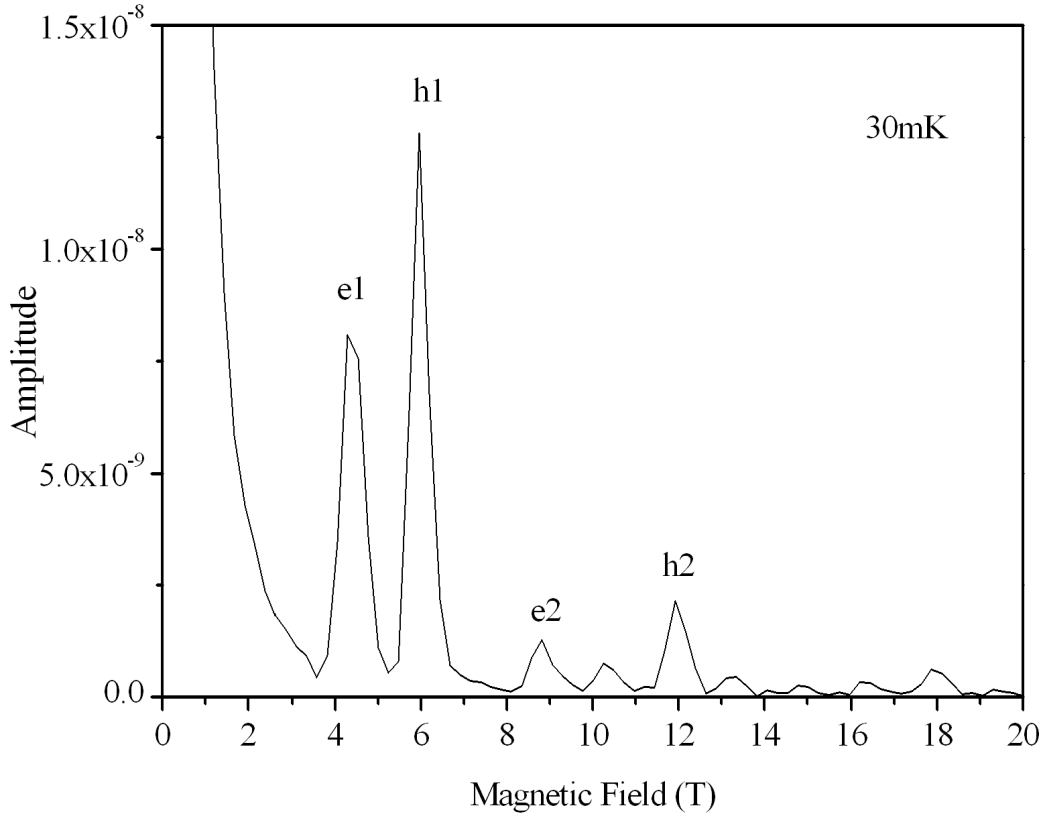

Fig. 5.4.ii Plot of the fast Fourier transform (FFT) of dHvA oscillations (shown in Fig. 5.4.i) over the region 0.25 T to 3.75 T at 30 mK ± 0.5 mK showing the different periodicities of the two carriers. First and second harmonic peaks are shown for both electrons and holes. Peak e1 is at 4.30 T and peak h1 is at 5.95 T. The peaks are assigned according to values for the electron and hole frequencies presented by Williamson [1965] using the SWMC model.

Hence we can allot the peaks in the FFT to the different carriers, the electrons with a fundamental field of 4.30 T and the holes with a fundamental field of 5.95 T. The FFT clearly shows the first and second harmonics of the oscillations with possible third harmonic peaks at ~13.2 T and ~18 T.

Upon close inspection of the low field oscillations it was noted that only one carrier frequency is present, compared to the high field oscillations where 'beating' between the two majority frequencies is clearly visible. By separately analysing the data over different ranges of magnetic field it is possible to gain an insight into the behaviour of the different carriers. Fig. 5.4.iii shows dHvA oscillations plotted against inverse magnetic field. The data has been divided into four sections each covering a different range of magnetic field, so that the contribution of each carrier to the observed oscillations at different magnetic fields can be determined.

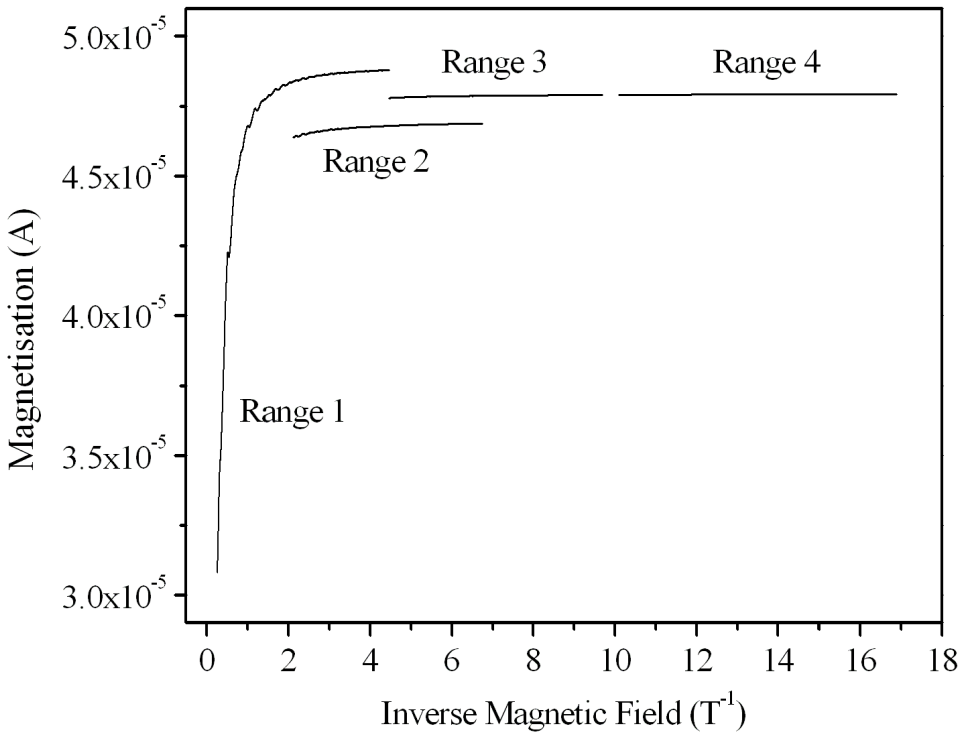

Fig. 5.4.iii Plot of dHvA oscillations against 1/*B*. The data has been divided into 4 sections to allow independent analysis of high and low field oscillations. Ranges 1 and 2 have been offset for clarity. The temperature is 30 mK ± 0.5 mK.

By interpolating each range of magnetic field shown in Fig. 5.4.iii in 1/*B* so that the points are evenly spaced in inverse field and performing a FFT on each range. The Fourier amplitude relating to each of the carriers in the different ranges can be obtained. The results of the FFT for each range are shown in Fig. 5.4.iv. As can be clearly seen the electron oscillations rapidly reduce with decreasing magnetic field, while the hole oscillations persist to fields below 100 mT.

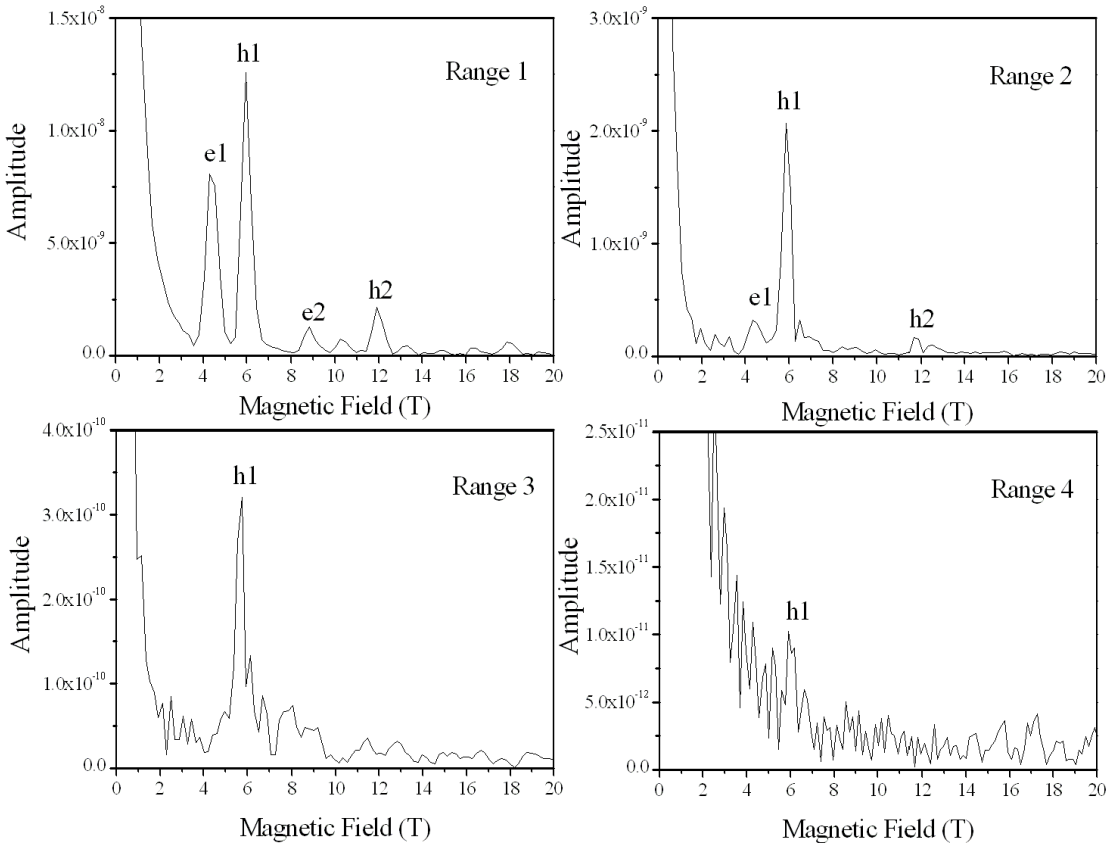

Fig. 5.4.iv FFT plots of dHvA oscillation frequencies for different range of magnetic field. The ranges correspond to those shown in Fig. 1.4.iii. The electron and hole frequencies are indicated along with the second harmonic if present. Note how the dHvA oscillations due to majority holes persist to lower magnetic fields but the electron oscillations quickly die out. The temperature was 30 mK ± 0.5 mK and the magnetic field was applied at 20˚ to the sample *c*-axis.

The electron oscillation's greater dependence on magnetic field could be attributed to the Landau levels being closer together (larger effective mass m^*) and hence $\hbar\omega_c$ becomes comparable to Landau level broadening Γ faster than for the hole oscillations as the magnetic field is decreased. This can easily be verified by examining the temperature dependence of the different carrier oscillations.

Fig. 5.4.v shows dHvA oscillations in the range 0.2 T to 5 T at 50 mK and 1.5 K. The inset shows the FFT of the two sets of data. The data show that the hole oscillations have a greater temperature dependence than the electron oscillations. This is in contradiction to the findings of the field dependence and the assumption that the

electron Landau levels are closer together in energy. This is supported by the work of McClure [1957] and Williamson [1965] who both claim an electron effective mass that is smaller than the hole effective mass. Therefore the electron Landau levels are further apart and the field dependence of the electron oscillations must be due to some other factor than the energy separation of the Landau levels. Alternatively the contradictory findings of the temperature and field dependence could be attributed to increased scattering of electrons or from increased scattering at certain positions within the Brillouin zone. Also the presence of Dirac fermions could explain these results, since the energy separation between Landau levels E_n and E_{n+1} at a given field is not equal for all values of n as it is for normal fermions. It is possible that the Dirac Landau level separation could be greater than the normal Landau level separation $\hbar\omega_c$ at high field but be closer together at low fields, thus explaining the temperature and field dependence of the two sets of carriers.

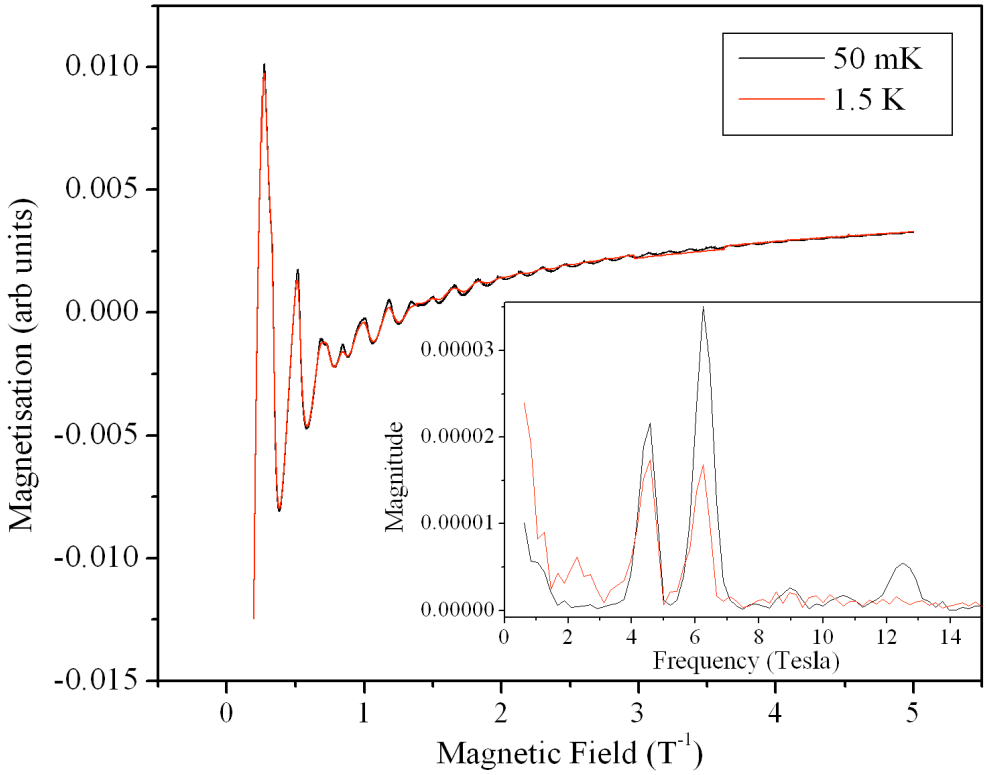

Fig. 5.4.v Plot of dHvA oscillations at 50 mK ± 1 mK and 1515 mK ± 15 mK after subtraction of a polynomial background versus inverse magnetic field perpendicular to the basal plane. The FFT of the two sets of oscillations is inset, note the different temperature dependence of the two sets of majority carriers. The magnetic field was applied at an angle of 2° to the sample *c*-axis.

5.5 Angle dependence

Observation of the dHvA oscillations with the magnetic field applied at different angles to the *c*-axis (perpendicular to the graphite planes) can give information about the shape of the Fermi surface. Williamson [1965] investigated the angle dependence of the dHvA oscillations in pyrolytic and single crystal graphite. It was found that the magnitude of the dHvA oscillations changed as the angle between the *c*-axis and the magnetic field was increased. Also the frequency of the oscillations changed as the cross sectional area of the extremal orbits changed.

The angle dependence of the dHvA oscillations in our HOPG sample has been briefly investigated. De Haas van Alphen oscillations with the magnetic field applied at angles of 2˚ and 20˚ to the *c*-axis have been observed and are shown in Fig. 5.5.i. While only two angles have been investigated there is no apparent difference in the frequency of the oscillations indicating that the electron and hole systems in HOPG samples are more 2D-like than those found in pyrolytic or single crystal graphite. More measurements with the magnetic field applied at larger angles to the sample *c*-axis are needed to build a better picture of the shape of the Fermi surface.

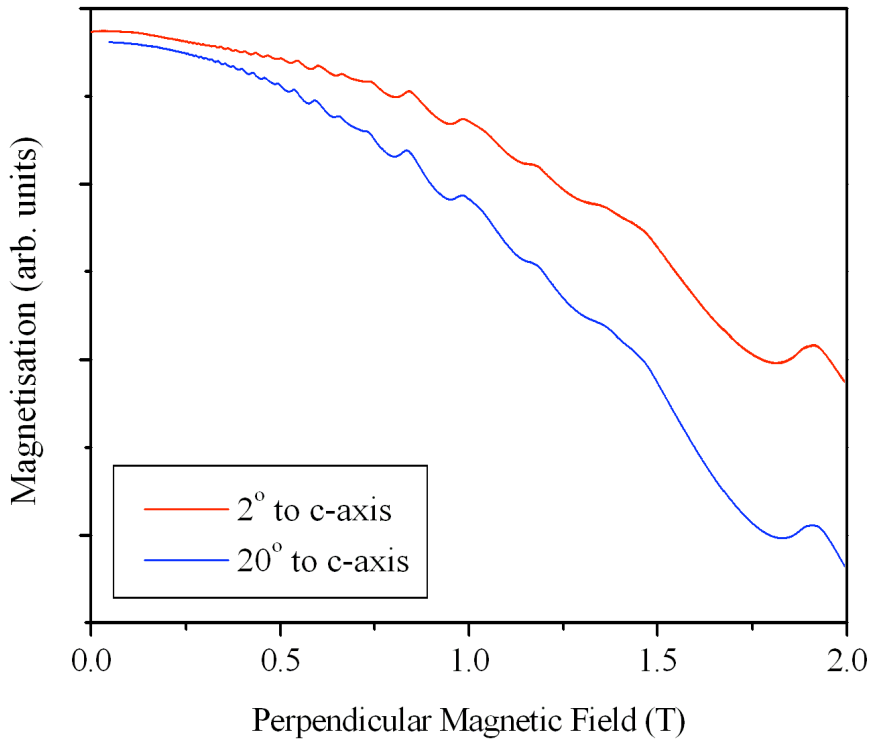

Fig. 5.5.i Plot of comparative dHvA oscillations with the sample *c*-axis at an angle of 2˚ and 20˚ to the applied magnetic field. The plot is of magnetisation against magnetic field perpendicular to the basal plane, the temperatures are 102 mK ± 2 mK and 30 mK ± 0.5 mK for the 2˚ and 20˚ data respectively. The traces are offset for clarity.

5.6 Transport data

As shown in chapter 1 (Fig. 1.7.vi) the QHE has been observed in HOPG samples [Luk'yanchuk (2006)]. Traces of R_{xx} and R_{xy} were obtained for the HOPG sample with the magnetic field applied parallel to the *c*-axis at a temperature of 2 K. The data showed plateaux in the transverse resistance (R_{xy}) and an anomalous longitudinal resistance (R_{xx}) that did not fall to zero at the position of the plateaux in R_{xy}. Using FFT analysis Luk'yanchuk [2006] showed that the QHE oscillations comprised two distinct carrier contributions, holes located at the *H* point and electrons located at the *K* point. The positions of the different carriers in the Brillouin zone was determined by angle-resolved photoemission spectroscopy (ARPES) [Zhou (2006)]. Note that the location of the carriers within the Brillouin zone reported by the ARPES measurements is in disagreement with those predicted by the SWMC model [McClure (1957)]. The analysis of Luk'yanchuk [2006] showed that the QHE 'staircase' for R_{xy} demonstrated the normal QHE for the electrons with a fundamental field of 4.68 T, for which, integer-filling factor lies in the centre of a plateau. The holes with fundamental field 6.41 T however, demonstrated the half integer QHE with the steps in resistance occurring at integer filling factor. The presence of the half integer QHE was compared with the presence of the Dirac QHE in graphene.

In order to make a direct comparison with the results obtained by Luk'yanchuk [2006], standard ac Hall measurements were carried out on the same HOPG sample used for the contactless magnetometry experiments. Fig. 5.6.i shows resistance traces of R_{xx} and R_{xy} for our HOPG sample at 30 mK. The field was applied at an angle of 20˚ to the *c*-axis to maintain consistency with the magnetometry experiments. The results are similar to those obtained by Luk'yanchuk [2006]. The longitudinal resistance R_{xx} is larger than the transverse resistance R_{xy} and does not fall to zero at the positions of the plateaux in R_{xy}. The anomalous behaviour of R_{xx} can be attributed to the presence of a large background resistance in addition to the oscillations.

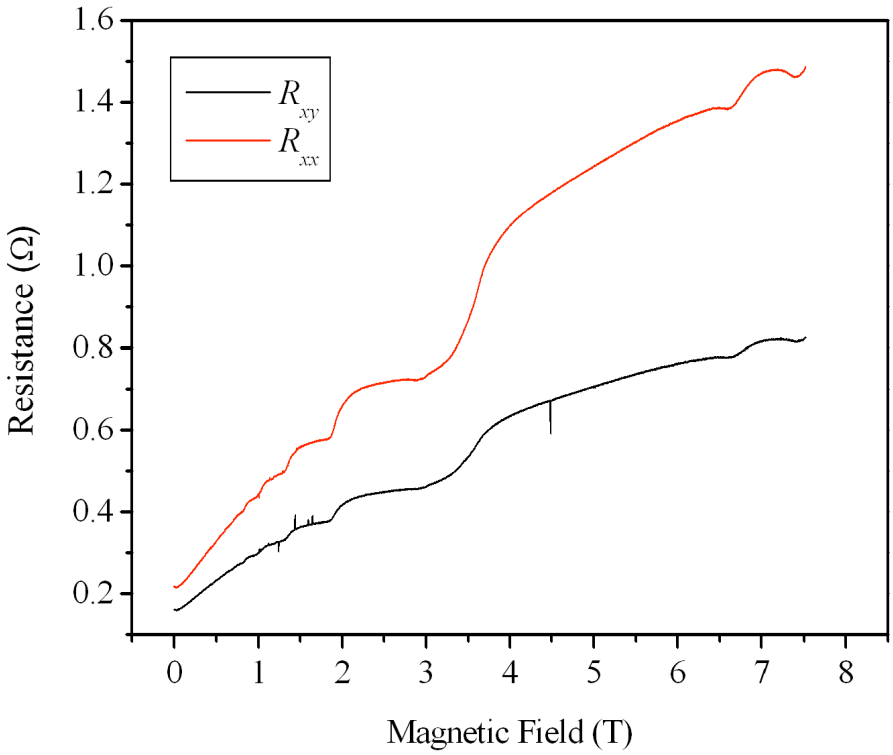

Fig. 5.6.i QHE plot of R_{xx} and R_{xy} versus applied magnetic perpendicular to the basal plane. The excitation current was 10 μA and the temperature was 30 mK ± 5 mK.

In order to determine if Dirac fermions are present in our HOPG sample, the R_{xy} data were converted to conductance using the formula

eqn. 5.6.i

$$\sigma_{xx} = \frac{\rho_{xx}}{\rho_{xy}^2 + \rho_{xx}^2}$$

By observing the periodicity of the steps in inverse magnetic field it is possible to attribute them to one of the majority carriers. By plotting the conductance against normalised filling factor $n = B/B_0$ where B_0 is the fundamental field, it is possible to discern the nature of the QHE 'staircase'. Fig. 5.6.ii shows the QHE 'staircase' obtained from the R_{xy} data shown in Fig. 5.6.i. The conductance (G_{xy}) staircase is consistent with a disorder broadened half integer QHE corresponding to the majority electron frequency. Interestingly the height of the steps is not a constant multiple of e^2/h as one would expect.

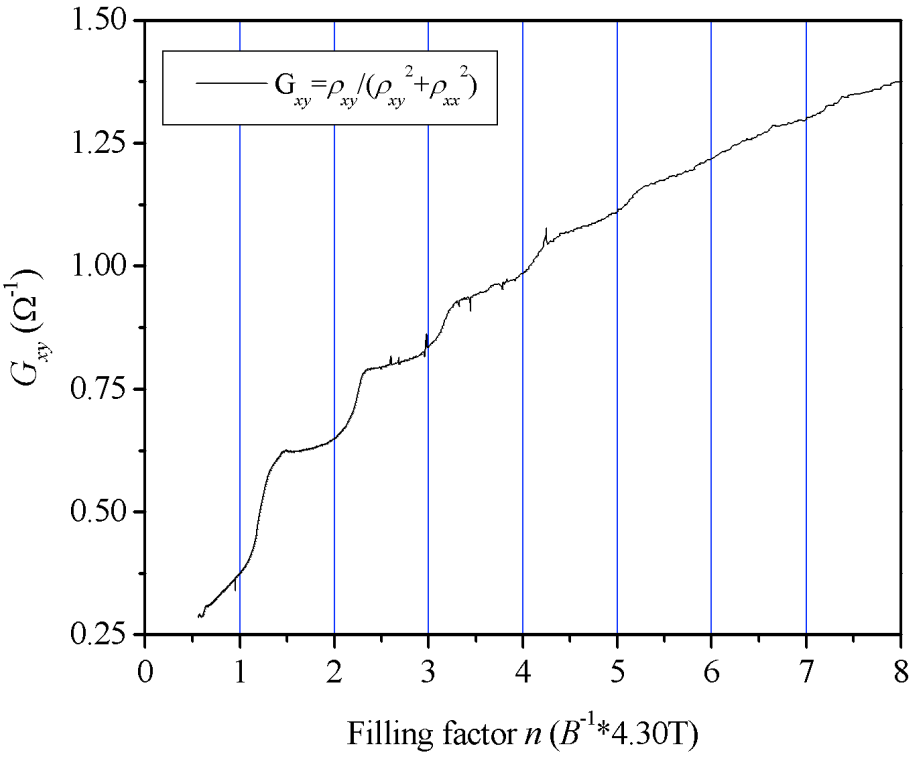

Fig. 5.6.ii Plot of conductance G_{xy} against normalised filling factor $n = B_0 / B$ where B_0 is the fundamental frequency of the electron oscillations 4.30 T. The periodicity of the Hall oscillations corresponds to the electron frequency. The position of integer filling factor is consistent with the Dirac QHE 'staircase' and the half integer QHE. Note however that the steps in conductance are not of equal size corresponding to a multiple of e^2/h.

The relatively few plateaus present in the QHE data are consistent with the electron oscillations in the dHvA data. The lack of any obvious hole oscillations especially at lower fields is surprising. The hole contributions can be obtained be Fourier filtering of the data. The QHE data was found to vary very little with temperature up to 3.8 K. This is consistent with the temperature dependence shown by the dHvA oscillations. This dependence could be due to the large energy gap associated with Dirac fermions described by eqn. 1.7.ix compared to normal fermions described by eqn. 1.4.xx, suggesting that electrons in graphite are Dirac fermions.

5.7 Landau level phase analysis

Analysis of the Landau level quantisation relies on the fact that the spectra for normal and Dirac fermions are different. In normal carriers the Landau levels are equidistant at

a given field and are described by $E_n = (n + ½)\hbar\omega_c$ as derived in chapter 1. Dirac fermions however are governed by $E_n = v_F(2eB\hbar n)^{½}$ also derived in chapter 1 and the Landau level separation at a given field varies as $n^{½}$ and the lowest Landau level is situated at $E_0 = 0$. For the normal carriers the Landau levels have the associated phase factor $\gamma = ½$ arising from the Bohr-Sommerfeld quantisation relation (eqn. 1.4.ii) used in chapter 1 to describe the quantisation of cyclotron orbits. This phase factor is related to the Berry phase $\Phi_B = k\pi$ acquired by a fermion moving around an orbit of area $S(E_F)$ [Mikitik (1999)]. For even k (normal fermions) $\gamma = ½$, and $\gamma = 0$ for odd values of k (Dirac fermions). Notice that the phase factor γ is absent in the expression for quantised energy levels of Dirac fermions above. There is also a further phase factor $|\delta| < ⅛$ which is governed by the curvature of the Fermi surface [Luk'yanchuk (2006)] for 2D systems $\delta = 0$. Since graphite has a 3D Fermi surface (Fig. 1.7.iv) the extra factor δ has to be included in the analysis. Hence we can write [Luk'yanchuk (2006)] that the longitudinal resistance R_{xx} varies as

eqn. 5.7.i
$$\Delta R_{xx} = A(B)\cos\left[2\pi\left(\frac{B}{B_0} - \gamma + \delta\right)\right],$$

where $A(B)$ is the non-oscillating amplitude and B_0 is the fundamental field. Luk'yanchuk (2006) obtained the phase factors γ and δ by plotting inverse magnetic field against conductivity (G_{xy}) oscillation maxima (minima) as a function of their Landau level n ($n - ½$). Linear extrapolation of the data to $B^{-1} = 0$ shows a phase difference ($-\gamma + \delta$) of $\sim\pi$ between the two carriers. This phase difference between the two carriers is due to different values of ($-\gamma + \delta$) and is termed Berry phase, this indicates that one of the carriers is a Dirac fermion and the other a normal fermion. Luk'yanchuk (2006) concluded that the hole oscillations have Berry phase π and hence are Dirac fermions, while the electron oscillations have Berry phase 0 and are normal fermions.

By interpolating the R_{xx} data shown in Fig. 5.6.i in $1/B$ to create a dataset of points evenly spaced in inverse field, the different contributions of the two carriers can be separated by FFT filtering. A band-pass filter centred on the electron oscillation frequency was used to separate the electron oscillations from the hole oscillations and the background signal. A high pass filter was used to isolate the hole oscillations. It is

possible to recombine the filtered data sets to return to the original data, indicating that the filtering process does not unduly alter the data, simply remove unwanted frequencies.

By plotting the $1/B$ value of the minima (maxima) of the filtered R_{xx} oscillations against their Landau level number n (n –½) the phase difference between the two sets of carriers was determined. As Fig. 5.7.i shows linear interpolation of the data to $B^{-1} = 0$ there is a phase difference of $\sim\pi$ between the two carriers. This corresponds to different values of γ in eqn. 5.7.i, for normal fermions $\gamma = ½$ and for Dirac fermions $\gamma = 0$. However in our data it is the holes that are the normal fermions while the electrons appear to be Dirac fermions with Berry phase π. The deviation of the x-axis intercept away from half integer values of n can be accounted for by the extra phase factor δ. Since $|\delta| < 1/8$ and is governed by the curvature of the Fermi surface, δ may take a different value for electrons and holes since each carrier originates from a separate pocket within the Fermi surface (Fig. 1.7.iv).

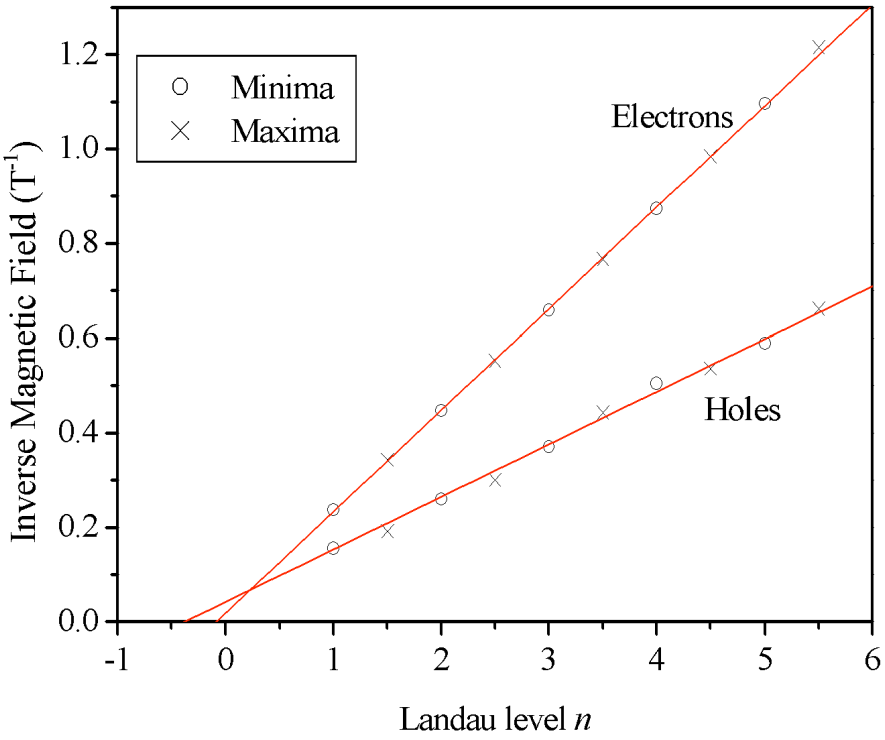

Fig. 5.7.i Plot of maxima and minima in R_{xx} for electron and hole oscillations against B^{-1}. The maxima in R_{xx} are assumed to occur at half way between Landau levels. Linear extrapolation of the data to $B^{-1} = 0$ shows the phase difference $(-\gamma + \delta)$ between normal and Dirac fermions.

For completeness similar analysis was performed on dHvA oscillations. Since integer-filling factors typically occur at the zero-crossing point on the high field side of a dHvA oscillation, it was decided to differentiate the magnetisation signal with respect to the magnetic field. This is because it is easier to locate oscillation maxima and minima rather than zero-crossing points. After differentiation the dM/dB data was interpolated in $1/B$ and a FFT filter was used to separate the different carrier contributions the same as for the R_{xx} data. A plot of the inverse magnetic field against maxima (minima) in dM/dB as a function of Landau level n ($n - ½$) shown in Fig. 5.7.ii shows that there is a Berry phase of π difference between the electrons and holes. Again it is the holes that are the normal carriers and the electrons that are the Dirac fermions.

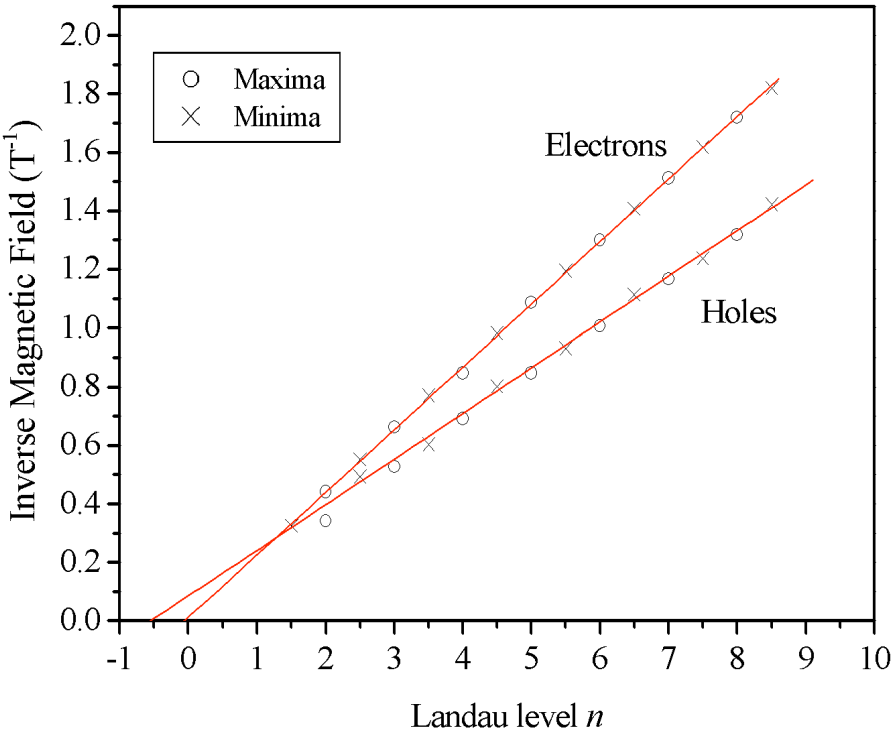

Fig. 5.7.ii Plot of maxima and minima in dM/dB for electron and hole oscillations against B^{-1}. The maxima in dM/dB are assumed to occur at half way between Landau levels. Linear extrapolation of the data to $B^{-1} = 0$ shows the phase difference $(-\gamma + \delta)$ between normal and Dirac fermions.

This analysis of R_{xx} and dHvA oscillations is consistent with the observation of the half integer QHE 'staircase' of conductance G_{xy} shown in Fig. 5.6.ii. These results are in contradiction to other observations of Dirac fermions in graphite [Luk'yanchuk (2004,

2006), Zhou (2006) and Kopelevich (2007)] where holes located close to the *H* point were observed to behave as Dirac fermions and electrons located close to the *K* point were observed to behave like normal fermions. The SWMC model [McClure (1957)] shows that holes are located at the *K* point and electrons near the *H* point, it also shows that the hole pocket located at the *K* point is larger than the electron pocket and hence the hole oscillation frequency is higher. This raises some questions about the validity of some statements in the papers by Luk'yanchuk, Zhou and Kopelevich, since the holes that are claimed to be Dirac fermions do indeed have a higher oscillation frequency as expected but they originate from the wrong point in the Brillouin zone according to accepted theory. The data presented in this section supports the assertion that Dirac fermions are present in graphite and that they originate from near the *H* point, however, the oscillation frequency suggests that they are electrons and not holes according to the theory of Slonczewski, Weiss and McClure. Instead the model proposed by Woollam [1971] and Saito [1998] appears to be correct.

5.8 dHvA oscillation phase analysis

Phase analysis of dHvA oscillations can also be used to determine if a carrier is normal or Dirac-like. Luk'yanchuk [2004] showed that the susceptibility χ oscillates as

eqn. 5.8.i $$\Delta\chi l \sim \mu\cos\left(2\pi\left[\frac{Bl}{B_o} - \gamma + \delta\right]\right)$$

Where l is the oscillation harmonic and μ is equal to +1 for electrons and to –1 for holes. Again the phase difference is dominated by the phase factor γ and to a lesser extent by δ. The phase of the oscillations can be extracted from Fourier analysis of oscillations in dM/dB. Comparison of the phase returned extracted from an FFT of the oscillations at a resonance peak allows identification of Dirac and normal fermions without filtering the data.

Fig. 5.8.i shows a screen capture of a Labview Virtual Instrument used to differentiate dHvA data and perform a FFT and return the phase at the resonance peaks. These phases can then be compared with what would be expected for different types of carrier using eqn. 5.8.i.

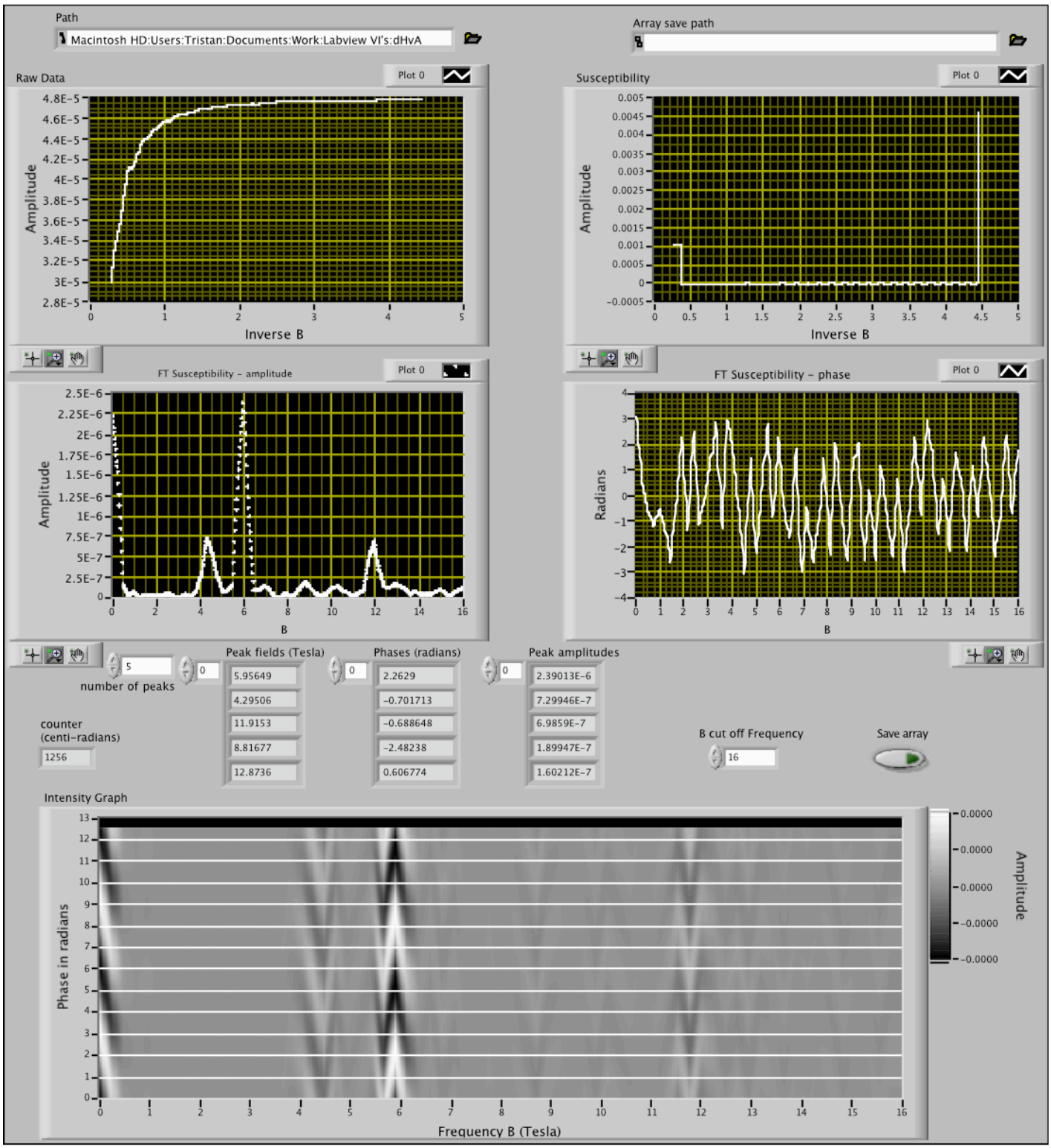

Fig. 5.8.i Screen capture of Labview VI, the different windows show from top left, dHvA data, *dM*/*dB*, FFT amplitude, FFT phase and Intensity plot showing how the phase varies around the resonance peaks. Also shown are the field positions of the different resonance peaks and their respective phase.

As shown in Fig. 5.8.i the oscillations with a resonance peak at ~5.95 T have a phase of 2.26 radians and the oscillations with a resonance peak at ~4.29 T have a phase of

–0.70. According to eqn. 5.8.i this is consistent with the higher frequency oscillations being normal fermions and the lower frequency oscillations being Dirac fermions with $\delta = -1/8$ in both cases. The intensity plot shown in Fig. 5.8.i shows how the phase varies around the fundamental field as the field is swept through the resonance peak, this is consistent with figure 4 in Luk'yanchuk [2004].

This method produces the same results as the previous method discussed in section 5.7 but without the need for the filtering of the data. Thus illustrating that filtering of the oscillations does affect the phase analysis. While this method is perhaps superior due to the lack of filtering required, the analysis is more complicated and harder to interpret and does not provide much extra information.

5.9 Discussion

Earlier in this chapter a temperature dependence of the dHvA oscillations of the different carriers was shown in Fig. 5.4.v. The temperature dependence showed that the hole oscillations were more temperature dependent than those of the electrons, suggesting that the hole Landau levels are closer together in energy than their electron counterparts. This was contradicted by the field dependence of the two carriers where the hole oscillations persist to far lower magnetic fields than the electron oscillations. A more detailed analysis of the temperature dependence shown in Fig. 5.9.i shows how the amplitude of the FFT peaks varies with temperature. The size of the FFT peak is related to the RMS amplitude of the dHvA oscillations. The first harmonics of the electron and hole peaks do not appear to change very much up to 485 mK, however the second and third harmonic peaks show a decrease in amplitude. At the highest temperatures the hole FFT amplitude is much smaller than the electron FFT amplitude. This is in contrast to at low temperatures where the electron peak is smaller than the hole peak. These results are consistent with the FFT data presented by Luk'yanchuk [2004] for dHvA oscillations in an HOPG sample at 2 K, where the electron FFT peak amplitude was ~50% greater than the hole FFT peak amplitude.

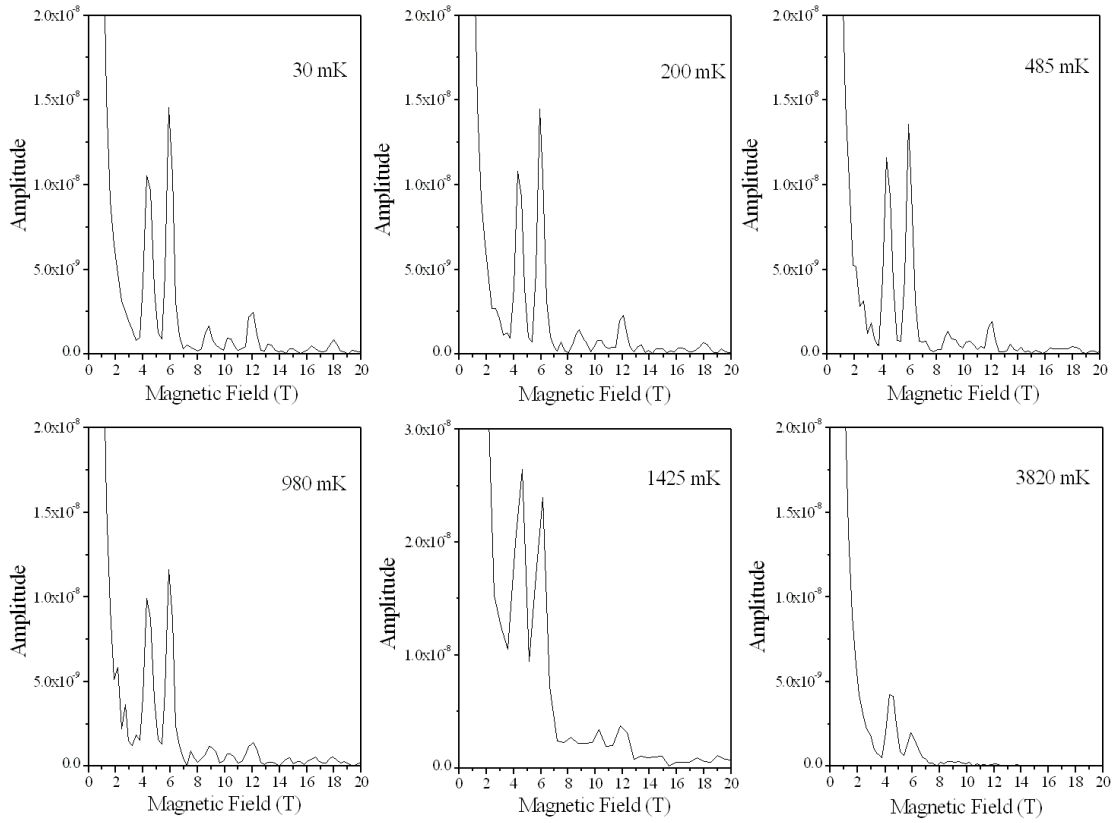

Fig. 5.9.i FFT plots of dHvA oscillations in the range 0.25 T to 3.75 T for different temperatures (0.5 T to 3.75 T for 1425 mK). The temperatures shown are from top left 30 mK ± 0.5 mK, 200 mK ± 4 mK, 485 mK ± 15 mK, 980 mK ± 40 mK, 1425 mK ± 100 mK and 3820 mK ± 5 mK. Note the increased temperature dependence of the holes over electrons. The magnetic field was applied at an angle of 20˚ to the *c*-axis.

By plotting a Landau level fan diagram of energy versus magnetic field for the normal holes and Dirac electrons (Fig. 5.9ii), it is possible to better visualise the different energy separations. It is clear that the hole Landau levels are much closer together in energy than the Dirac ones, which explains the greater temperature dependence. From the data presented in Fig. 5.4.iii and Fig. 5.4.iv the electron oscillations have died away at fields below ~0.5 T. Comparison of the energy separation of the Landau levels at 0.5 T and again at 0.2 T for the normal holes and the Dirac electrons shows that all the occupied electron Landau levels at these fields have a greater energy separation than the occupied hole Landau levels. This means that the field dependence of the Dirac electrons cannot be explained by the energy separation of the Landau levels.

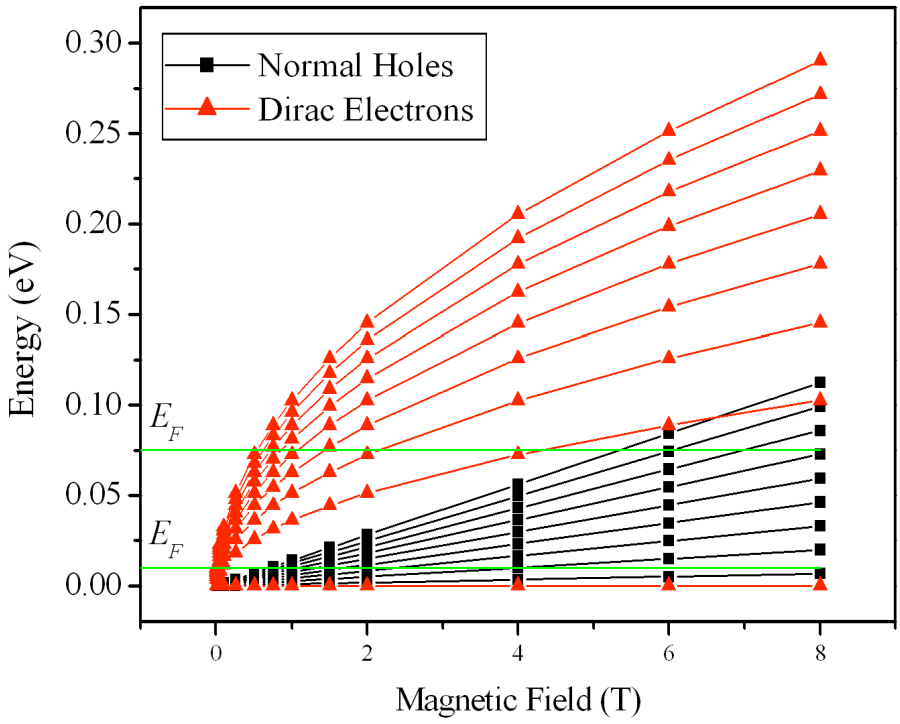

Fig. 5.9.ii Fan diagram showing Landau levels $0 \leq n \leq 8$ for normal and Dirac fermions. The energy levels were calculated using eqn. 1.4.xx for normal fermions and eqn. 1.7.ix for the Dirac fermions. The zero field Fermi energy E_F is also shown for normal (bottom) and Dirac (top) fermions using eqn. 1.2.xvi and eqn. 1.7.iv respectively. The effective mass m^* for the normal holes used in these calculations was $0.07m_e$ [McClure (1957)] and a value of 1×10^6 ms^{-1} was used for the Fermi velocity v_F of the Dirac electrons.

The discrepancy between our results and those of Luk'yanchuk can be partly explained by modification of the theory. Woollam [1971] modified some of the parameters in the SWMC model to change the sign of the charge carriers in the graphite Fermi surface, in order to explain experimental results. This modification to the SWMC model allows majority electrons to be located at the *K* point and majority holes to be located at the *H* point, the shape of the Fermi surface is unaffected. This modification of the band structure allows Fig. 1.7.iv to be redrawn as shown in Fig. 5.9.iii.

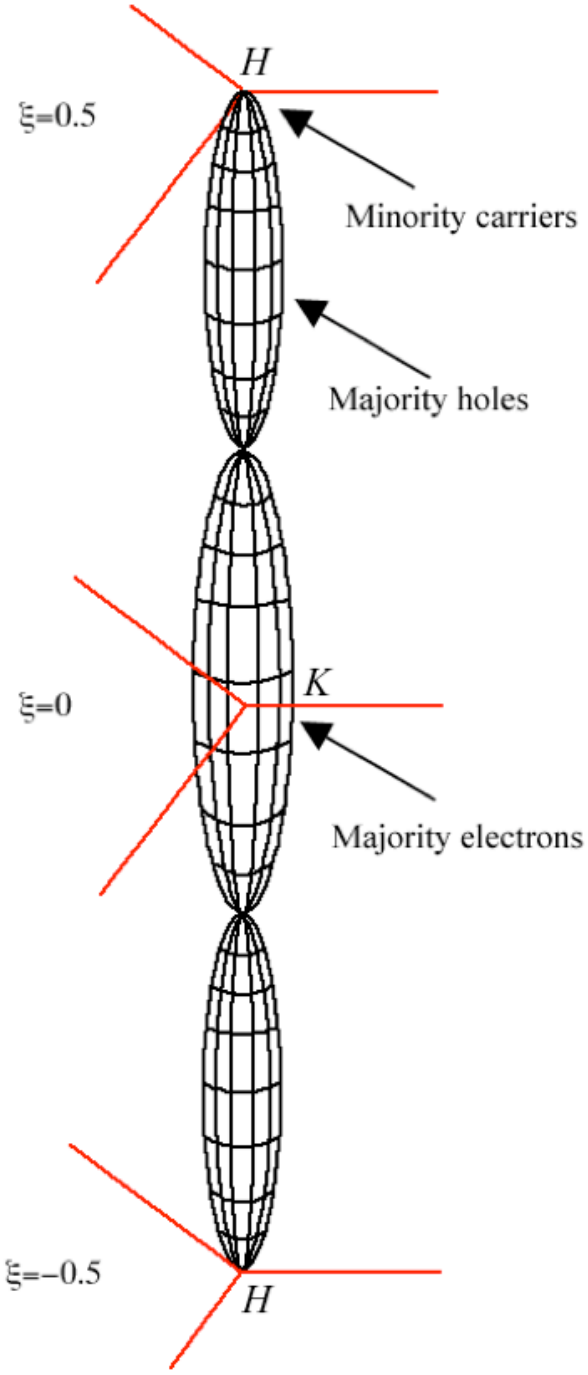

Fig. 5.9.iii Illustration of the Fermi surface of graphite along the Brillouin zone edge *HKH*. According to modified SWMC theory [Woollam (1971)] electrons are located at the *K* point and holes are located close to the *H* point.

To determine the polarity of the fermions in our sample, we can compared the phase of the quantum oscillations of susceptibility $\Delta\chi(B^{-1})$ and resistance $\Delta R(B^{-1})$ as used by Luk'yanchuk. The sign of the $\Delta R(B^{-1})$ oscillations is reversed to recover the behaviour of the oscillating part of the conductivity $\Delta\sigma(B^{-1})$ [Luk'yanchuk (2004)], by overlaying $\Delta\chi(B^{-1})$ the phase difference can be obtained. As shown in eqn. 5.8.i the susceptibility is

dependant on the factor μ, which takes the values +1 for electrons and –1 for holes. This implies that the susceptibility and conductivity oscillations will be in phase for the electrons but out of phase for the holes. Using band pass filtering to separate the individual carrier contributions of the susceptibility and conductivity oscillations, we find that the higher frequency (FFT peak at 5.95T) majority carrier oscillations in conductivity and susceptibility are in phase and hence are electrons. The lower frequency oscillations (FFT peak at 4.30T) are out of phase and hence are holes. The higher frequency of the electron oscillations compared to the hole oscillations suggests that the electrons are located at the *K* point where the cross-sectional area of the Fermi surface is greater, and the holes are located at the extremal orbit close to the *H* point. This picture is consistent with that presented by Woollam [1971] with the polarity of the carriers reversed compared to the original SWMC model devised by Slonczewski, Weiss and Mc Clure. Luk'yanchuk, however claims that the higher frequency oscillations are majority holes located close to the *H* point, the higher frequency would imply that the carriers are located at the *K* point, so there is still some uncertainty associated with the results of Luk'yanchuk.

In order to explain the field dependence of the electrons, there must be greater scattering of the fermions near the *H* point compared to the fermions close the *K* point. At this time it is unclear what could cause increased scattering of the Dirac holes close to the *H* point or decrease scattering of the normal electrons at the *K* point. It is possible that trigonal warping of the Fermi surface could affect the scattering of the fermions. Williamson [1965] and Soule [1964] showed that trigonal warping of the Fermi surface due to the three-fold symmetry of the graphite is greatest near the *K* point as shown in Fig. 5.9.iv, this could lead to reduced elastic scattering of the electrons.

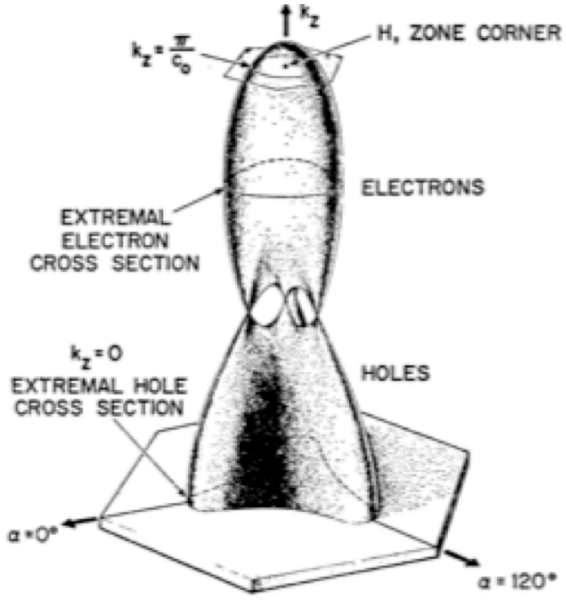

Fig. 5.9.iv Illustration of the Fermi surface of graphite showing trigonal warping of the Fermi surface near the *K* point and the extremal electron and hole orbits. Figure taken from Williamson [1965] (this picture shows the results of a calculation using the SWMC model so the majority electrons and holes need to be reversed to match the results of Woollam [1971] and those presented in this thesis).

5.10 Summary

In this chapter we have presented results that show that graphite exhibits a 2D-like QHE. However the presence of minority carriers indicate the presence of a 3D Fermi surface. We also confirm the work of Luk'yanchuk [2004, 2006], Zhou [2006] and Kopelevich [2007] by showing evidence of the presence of Dirac fermions in graphite. Observation of the half integer QHE in graphite indicates the presence of Dirac fermions consistent with those observed in graphene by Novoselov [2005]. The oscillation frequency associated with the half-integer QHE in graphite corresponds to the lower frequency oscillations, which we have attributed to holes located close to the *H* point in agreement with Woollam [1971]. Separate analysis of the phase of the Landau level quantisation spectra for both conventional transport data and magnetometry data indicate a difference in the phase factor between of the two sets of carriers. The data suggest that the holes are Dirac fermions with Berry phase π corresponding to a phase factor $\gamma = 0$, whereas the electrons are normal carriers with phase factor $\gamma = ½$. At this point it is still unclear whether the electrons or holes are 2D or 3D-like, further experiments to measure the angle dependence of the dHvA

oscillation frequency and amplitude would need to be done to establish the nature of the different carriers.

6 Conclusions and Future Work

The experimental work presented in this thesis studies both the equilibrium magnetisation and the magnetic moment of induced currents in the quantum Hall regime as well as measurements of the QHE in graphite.

Chapter 3 studies de Haas – van Alphen oscillations in a sample A2268 a 10× quantum well sample. Modelled magnetisation $M(B)$ oscillations were fit to the experimental data to determine the shape of the disorder broadened density of states. A Lorentzian model for the broadening of the density of states with a field independent width Γ produced the best fit. The Gaussian model with a $B^{1/2}$ dependence of Γ achieved similar results in the presence of a large background density of states between the Landau levels. The temperature dependence of the dHvA oscillations indicated that the width Γ of the broadened Landau levels was due to scattering from remote ionised donors. The data suggest that there is a transition from a Gaussian DOS with a $B^{1/2}$ dependence of Γ to a Lorentzian DOS line shape as the magnetic field is increased. This implies that at higher Landau levels there are short-range events that contribute to the width of the Landau levels. Further experiments measuring the magnetisation at higher Landau levels (lower magnetic fields) would have to be carried out to confirm the presence of a transition from Gaussian Landau level broadening to Lorentzian and to understand the mechanics of the transition. This would probably involve measurements of a multiple quantum well sample at low temperatures. Improvements to the sensitivity and stability of the magnetometer would also be necessary in order to resolve dHvA oscillations at low magnetic fields.

Chapter 4 focuses on magnetometry experiments on two modulation-doped heterojunctions V0049 and T73. Magnetometry measurements of the magnetic moment were used to observe the decay of the induced current in the quasi-dissipationless quantum Hall regime. Two distinct decay regimes were observed, an initial exponential decay followed by a much slower power-law decay. The initial exponential decay was attributed to the high current breakdown of the quantum Hall effect. Once the current has fallen below a critical value the quasi-dissipationless QHE regime is restored and the current follows a power-law form of decay. The presence of a power-law form of decay suggests multiple relaxation paths and a ρ_{xx} which is approximately proportional

to t^{-1}. The longitudinal resistivity ρ_{xx} was calculated to decrease by two orders of magnitude over the first 12 hours of the decay. These measurements imply that a significant induced current is present in the sample for much longer than was previously thought. Further experiments are needed to observe if the power-law decay evolves into a single exponential decay at long time scales as predicted. However this would involve improving the temperature and mechanical stability of the dilution refrigerator. Improvements to the magnetic field stability or a least a better understanding of the relationship between reported magnetic field and actual magnetic field is also required. These improvements should also allow the observation of the decay 'phase transition' as reported in Ising spin glasses if it is present in two dimensional electron systems. It would also be interesting to extend the experiments to observe the decay of the induced currents in the fractional quantum Hall regime to see if composite fermions have similar decay mechanisms to single fermions in the integer quantum Hall regime.

Chapter 5 aims to observe Dirac fermions in graphite with a linear dispersion relation in a ZYB grade HOPG sample. The results detailed in chapter 5 focus on various magnetometry experiments to observe dHvA oscillations of the two majority carriers in graphite as well as standard transport measurements of the quantum Hall effect. The results presented in chapter 5 confirm the work of Luk'yanchuk, Kopelevich and Zhou by showing that Dirac fermions are present in bulk graphite. The Dirac fermions were shown to be present using phase analysis of dHvA and SdH oscillations. In order for the phase analysis to work the oscillation contributions of the different carriers need to be separated using Fourier analysis. The presence of the half integer quantum Hall 'staircase' is a further indication that Dirac fermions with Berry phase π are present in the graphite sample. Comparison of the oscillation frequency and phase with the modified SWMC theory of Woollam indicates that the Dirac fermions are holes located near the *H* point in the Brillouin zone, the other carriers are normal electrons located at the *K* point. At this point it is still unclear whether the electrons or holes are 2D or 3D-like, further experiments to measure the angle dependence of the dHvA oscillation frequency and amplitude would need to be done to establish the nature of the different carriers. Also further experiments coupled with some theoretical calculations are needed to discover the reason for the increased scattering of the Dirac holes near the *H* point. For completeness a study of different grades of graphite to see if Dirac fermions are present in all types of graphite or just the highest quality samples. Similar experiments on ZYA and ZYH grades of HOPG graphite as well as Kish, single crystal pyrolytic

graphite or natural graphite would help explain why Dirac fermions have not been discovered in graphite before despite the numerous experiments performed over the last few decades. Comparison of our results on ZYB grade with results from ZYA grade graphite could explain some of the discrepancies between the results presented in this thesis and the findings of Luk'yanchuk and Kopelevich, such as the higher oscillation frequency of the holes compared to the electrons.

References

1. Abergel D S L, Russell A, Fal'ko V I, 2007 Appl. Phys. Lett. **91** 063125

2. Ahlswede E, Weis J, von Klitzing K, Eberl K, 2002 Physica E **12**, 165

3. Ando T, Uemura Y, 1974 J. Phys. Japan **36** 959

4. Ashoori R C, Silsbee R H, 1992 Solid State Commun **81** 821

5. Bernevig B A, Hughes T L, Raghu S, Arovas D P, 2007 Phys. Rev. Lett. **99** 146804

6. Cage M E, Dziuba R F, Field B F, 1985 IEEE Trans. Instrum. Meas. IM-**34**, 301

7. Chaubet C, Geniet F 1998 Phys. Rev. B **58** 13015

8. Chklovskii D B, Shklovskii B I and Glazman L I 1992 Phys. Rev. B **46** 4026

9. de Haas W J, van Alphen P M, 1933 Proc. Neth. R Acad. Sci. **33** 1106

10. Ebert G, von Klitzing K, Ploog K and Weimann G 1983 J. Phys. C: Solid State Phys. **16** 5441

11. Eisenstein J P, Boebinger G S, Pfeiffer L N, West K W, He S, 1992 Phys. Rev. Lett. **68** 1383

12. Eisenstein J P, Störmer H L, Narayanamurti V, Cho A Y, Gossard A C, Tu C W, 1985 Phys. Rev. Lett. **55** 875

13. Eisenstein J P, Stormer H L, Narayanamurti V and Gossard A C 1985 Superlatt. Microstruct. **1** 11

14. Elliott M, Lu Y, Phillips K, Herrenden-Harker W G, Usher A, Matthews A J, Gething J D, Zhu M, Henini M and Ritchie D A, 2006 Europhys. Lett. **75** 287

15. Gerhardts R R, Gudmundsson V, 1986 Phys. Rev. B **34** 2999

16. Gonzalez J, Guinea F, Vozmediano M A H, 1996 Phys. Rev. Lett. **77** 3589

17. Gornik E, Lassnig R, Strasser G, Störmer H L, Gossard A C, Wiegmann W, 1985 Phys. Rev. Lett **54** 1820

18. Heinonen O, Taylor P L and Girvin S M, 1984 Phys. Rev. B **30** 3016

19. Huels J, Weis J, Smet J, von Klitzing K and Wasilewski Z R 2004 Phys. Rev. B **69** 085319

20. Jones C L, Usher A, Elliott M, Herrenden-Harker W G, Potts A, Shepherd R, Cheng T S and Foxon C T, 1995 Solid State Commun. **95** 409

21. Jones C L, Usher A, Elliott M, Herrenden-Harker W G, Potts A, Shepherd R, Cheng T S and Foxon C T 1996 Solid State Commun. **97** 763

22. Kempa H, Esquinazi P, Kopelevich Y, 2003 Solid State Commun **125** 1

23. Kershaw T J, Usher A, Sachrajda A S, Gupta J, Wasilewski Z R, Elliott M, Ritchie D A, Simmons M Y, 2007 New J. Phys. **9** 71

24. Klaffs T, Krupenin V A, Weis J and Ahlers F J 2004 Physica E **22** 737

25. Kopelevich Y, Esquinazi P, 2007 Cond–Mat. arXiv:0712.4020v2

26. Laughlin R B, 1981 Phys. Rev. B **23** 5632

27. Li G, Andrei E Y, 2007 Nat. Phys. **3** 623

28. Lifshitz I M, Kosevich A M, 1956 Soviet Phys. JETP **2** 636

29. Lifshitz E M, Pitaevskii L P, Berestetskii V B, *Quantum Electrodynamics* (Butterworth-Heinmann, Oxford, 1982)

30. Luk'yanchuk I A, Kopelevich Y, 2004 Phys. Rev. Lett. **93** 166402

31. Luk'yanchuk I A, Kopelevich Y, 2006 Phys. Rev. Lett. **97** 256801

32. Matthews A J, Kavokin K V, Usher A, Portnoi M E, Zhu M, Gething J D, Elliott M, Herrenden-Harker W G, Phillips K, Ritchie D A, Simmons M Y, Sorensen C B, Hansen O P, Mironov O A, Myronov M, Leadley D R, Henini M, 2004 Phys. Rev. B **70** 075317 (a)

33. Mathews A J, Usher A, Williams C D H, 2004 Rev. Sci. Instrum. **75** 2672 (b)

34. Matthews A J, Watts J P, Zhu M, Usher A, Elliott M, Herrenden-Harker W G, Morris P R, Simmons M Y, Ritchie D A, 2000 Physica E **6** 140

35. McCann E, Fal'ko V I, 2006 Phys. Rev. B **96** 086805

36. McClure J W, 1957 Phys. Rev. **108** 612

37. Mikitik G P, Sharlai Yu. V, 1999 Phys. Rev. Lett. **82** 2147

38. Novoselov K S, Geim A K, Morozov S V, Jiang D, Zhang Y, Dubonos S V, Grigorieva I V, Firsov A A, 2004 Science **306** 666

39. Novoselov K S, Geim A K, Morozov S V, Jiang D, Katsnelson M I, Grigorieva I V, Dubonos S V, Firsov A A, 2005 Nature **438** 197

40. Onsager L, 1952 Phil. Mag. **43** 1006

41. Oxford Instruments Kelvinox system manuals.

42. Peierls Z, 1933 Z Phys. **81** 186

43. Pioro-Ladriere M, Usher A, Sachrajda A S, Lapointe J, Gupta J, Wasilewski Z, Studeniken S, Elliott M, 2006 Phys. Rev. B **73** 075309

44. Potts A, Shepherd R, Herrenden-Harker W G, Elliott M, Jones C L, Usher A, Jones G A C, Ritchie D A, Linfield E H, Grimshaw M, 1996 J. Phys.: Condens. Matter **8** 5189

45. RS components, rswww.com

46. Saito R, Dreselhaus G, Dresselhaus M S, *Physical properties of carbon nanotubes* (World Scientific Publishing Company, 1998)

47. Shoenberg D, 1984 J. Low Temp. Phys. **56** 417

48. Slonczewski J C and Weiss P R, 1958 Phys. Rev. **109** 272

49. Streda P, von Klitzing K, 1984 J. Phys. C: Solid State Phys. **17** L483

50. Tsui D C, 1999 Rev. Mod. Phys. **71** 891

51. Tsui D C, Störmer H L, Gossard A C, 1982 Phys. Rev. Lett. **48** 1559

52. Viculis L M, Mack J J, Mayer O M, Hahn H T, Kaner R B, 2005 J. Mater. Chem. **15** 974

53. von Klitzing K, Dorda G and Pepper M, 1980 Phys. Rev. Lett. **45** 464

54. von Klitzing K, 1986 Rev. Mod. Phys. **58** 519

55. Wegner F, 1983 Z. Phys. B. **51** 279

56. Williamson S J, Foner S and Dresselhaus M S, 1965 Phys. Rev. **140** A1429

57. Woollam J A, 1971 Phys. Rev. B **3** 1148

58. Zhou S Y, Gweon G H, Graf J, Fedorov A V, Spataru C D, Diehl R D, Kopelevich Y, Lee D H, Louie S G, Lanzara A, 2006 Nat. Phys. **2** 595

List of Equations

eqn. 1.4.v $$\hbar\mathbf{k} = q(\mathbf{r}\times\mathbf{B})$$ 21

eqn. 1.4.vi $$\oint \hbar\mathbf{k}\cdot d\mathbf{r} = q\oint \mathbf{r}\times\mathbf{B}\cdot d\mathbf{r} = -q\mathbf{B}\cdot\oint \mathbf{r}\times d\mathbf{r} = -2q\boldsymbol{\Phi},$$ 21

eqn. 1.4.vii $$q\oint \mathbf{A}\cdot d\mathbf{r} = q\int \text{curl}\,\mathbf{A}\cdot d\boldsymbol{\sigma} = q\int \mathbf{B}\cdot d\boldsymbol{\sigma} = q\boldsymbol{\Phi},$$ 21

eqn. 1.4.viii $$\oint \mathbf{p}\cdot d\mathbf{r} = -q\boldsymbol{\Phi} = (n+\gamma)2\pi\hbar.$$ 22

eqn. 1.4.ix $$\boldsymbol{\Phi}_n = (n+\gamma)\frac{h}{e}.$$ 22

eqn. 1.4.x $$A_n = \left(\frac{\hbar}{eB}\right)^2 S_n.$$ 22

eqn. 1.4.xi $$\boldsymbol{\Phi}_n = \left(\frac{\hbar}{e}\right)^2 \frac{1}{B} S_n = (n+\gamma)\frac{h}{e}.$$ 22

eqn. 1.4.xii $$S_n = (n+\gamma)\frac{2\pi eB}{\hbar}.$$ 22

eqn. 1.4.xiii $$S\left(\frac{1}{B_n} - \frac{1}{B_{n+1}}\right) = \frac{2\pi e}{\hbar}.$$ 22

eqn. 1.4.xiv $$\Delta S = S_{n+1} - S_n = \frac{2\pi e}{\hbar}B$$ 23

eqn. 1.4.xv $$D = \frac{2\pi eB}{\hbar}\left(\frac{L}{2\pi}\right)^2 = \frac{eBL^2}{h}$$ 23

eqn. 1.4.xvi $$T = \oint \frac{\hbar dk}{ev_\perp B} = \frac{\hbar^2}{eB}\frac{\oint \delta k_\perp dk}{\delta E}$$ 24

eqn. 1.4.xvii $$\omega_c = \frac{2\pi}{T} = \frac{2\pi eB}{\hbar^2}\frac{dE}{dS}.$$ 24

eqn. 1.4.xviii $$m_c = \frac{\hbar^2}{2\pi}\frac{dS}{dE}$$ 24

eqn. 1.4.xix $$\frac{1}{m^*} = \frac{1}{\hbar^2}\left(\frac{d^2E}{dk^2}\right).$$ 24

eqn. 1.4.xx $$E_n = (n+\tfrac{1}{2})\hbar\omega_c + \frac{\hbar^2 k_z^2}{2m}$$ 25

eqn. 1.4.xxi $$\frac{\hbar^2}{2m}(k_x^2 + k_y^2) = (n+\tfrac{1}{2})\hbar\omega_c.$$ 25

eqn. 1.4.xxii $$E_n = (n+\tfrac{1}{2})\hbar\omega_c.$$ 25

eqn. 1.4.xxiii $$\nu = \frac{N\Phi_o}{\Phi}.$$ 25

eqn. 1.4.xxiv $$\nu = \frac{n_e h}{eB}.$$ 25

eqn. 1.5.i $$F = U - TS,$$ 25

eqn. 1.5.ii $$dU = dQ + dW,$$ 26

eqn. 1.5.iii $$dQ = TdS.$$ 26

eqn. 1.5.iv $$dW = -\mathbf{M}\bullet d\mathbf{B},$$ 26

eqn. 1.5.v $$dF = -SdT - \mathbf{M}\bullet d\mathbf{B}.$$ 26

eqn. 1.5.vi $$M = -\left(\frac{\partial F}{\partial B}\right)_T.$$ 26

eqn. 1.5.vii $$F(B) = \sum_{n=0}^{n=\lambda-1} D\left(n+\frac{1}{2}\right)\hbar\omega_c + \left(\lambda+\frac{1}{2}\right)\hbar\omega_c\left(N - D\lambda\right),$$ 27

eqn. 1.6.i $$\kappa = -\frac{1}{V}\left(\frac{\partial V}{\partial P}\right)_S .$$ 31

eqn. 1.6.ii $$\kappa \propto \frac{1}{\frac{\partial^2 E}{\partial V^2}}.$$ 31

eqn. 1.6.iii $$V \propto \frac{1}{\nu}$$ 31

eqn. 1.6.iv $$E_n = (n + \tfrac{1}{2})\hbar\omega_c + U_D$$ 32

eqn. 1.6.v $$\mathbf{j} = \sigma\mathbf{E},$$ 35

eqn. 1.6.vi $$\sigma_{xx} = \frac{\rho_{xx}}{\rho_{xx}^2 + \rho_{xy}^2}.$$ 36

eqn. 1.6.vii $$\rho_{xy} = -\frac{B}{n_e e},$$ 36

eqn. 1.6.viii $$\rho_{xy} = \frac{h}{ie^2}.$$ 36

eqn. 1.6.ix $$I = \frac{\partial U}{\partial \Phi}$$ 37

eqn. 1.6.x $$A \rightarrow A + \delta A = A + \frac{\delta\Phi}{L},$$ 37

eqn. 1.6.xi $$\Delta U = neV_H .$$ 38

eqn. 1.6.xii $$I = \frac{\partial U}{\partial \Phi} = \frac{\Delta U}{\Delta \Phi}$$ 38

eqn. 1.6.xiii $$I = \frac{neV}{\Delta\Phi} = \frac{ne^2 V}{h}.$$ 38

eqn. 1.6.xiv $$\rho_{xy} = \frac{h}{ne^2}$$ 38

eqn. 1.7.i $$E_k = \hbar v\mathbf{k} = \hbar v\sqrt{k_x^2 + k_y^2 + k_z^2}$$ 47

eqn. 1.7.ii $$E_F = \hbar v_F \left(\frac{3\pi^2 N}{V}\right)^{\frac{1}{3}}.$$ 48

eqn. 1.7.iii $$E_F = \hbar v_F \left(\frac{2\pi N}{L^2}\right)^{\frac{1}{2}}.$$ 48

eqn. 1.7.iv $$D(E) \equiv \frac{dN}{dE} = \frac{L^2}{\pi}\frac{E}{(\hbar v_F)^2}.$$ 48

eqn. 1.7.v $$\hat{H} = v_F \begin{pmatrix} 0 & p_x - ip_y \\ p_x + ip_y & 0 \end{pmatrix}\begin{pmatrix} A \\ B \end{pmatrix} = E\begin{pmatrix} A \\ B \end{pmatrix}$$ 48

eqn. 1.7.vi $$\begin{pmatrix} -E & v_F\left(-i\hbar\frac{\partial}{\partial x} - eB_y - \hbar\frac{\partial}{\partial y}\right) \\ v_F\left(-i\hbar\frac{\partial}{\partial x} - eB_y + \hbar\frac{\partial}{\partial y}\right) & -E \end{pmatrix}\begin{pmatrix} \chi_A(y) \\ \chi_B(y) \end{pmatrix} e^{ik_x x} = 0.$$ 49

eqn. 1.7.vii $$-\frac{d^2\psi}{dx^2} + x^2\left(\frac{m^2\omega^2}{\hbar^2}\right)\psi = \frac{2mE}{\hbar^2}\psi,$$ 49

eqn. 1.7.viii $$E_s = \pm\sqrt{2eB\hbar v_F^2(s+1)} = \pm\frac{\hbar v_F}{l_B}\sqrt{2(s+1)},$$ 49